TECHNICAL CONCEPTS FOR A

LONG-WAVELENGTH TARGET STATION

FOR THE

SPALLATION NEUTRON SOURCE

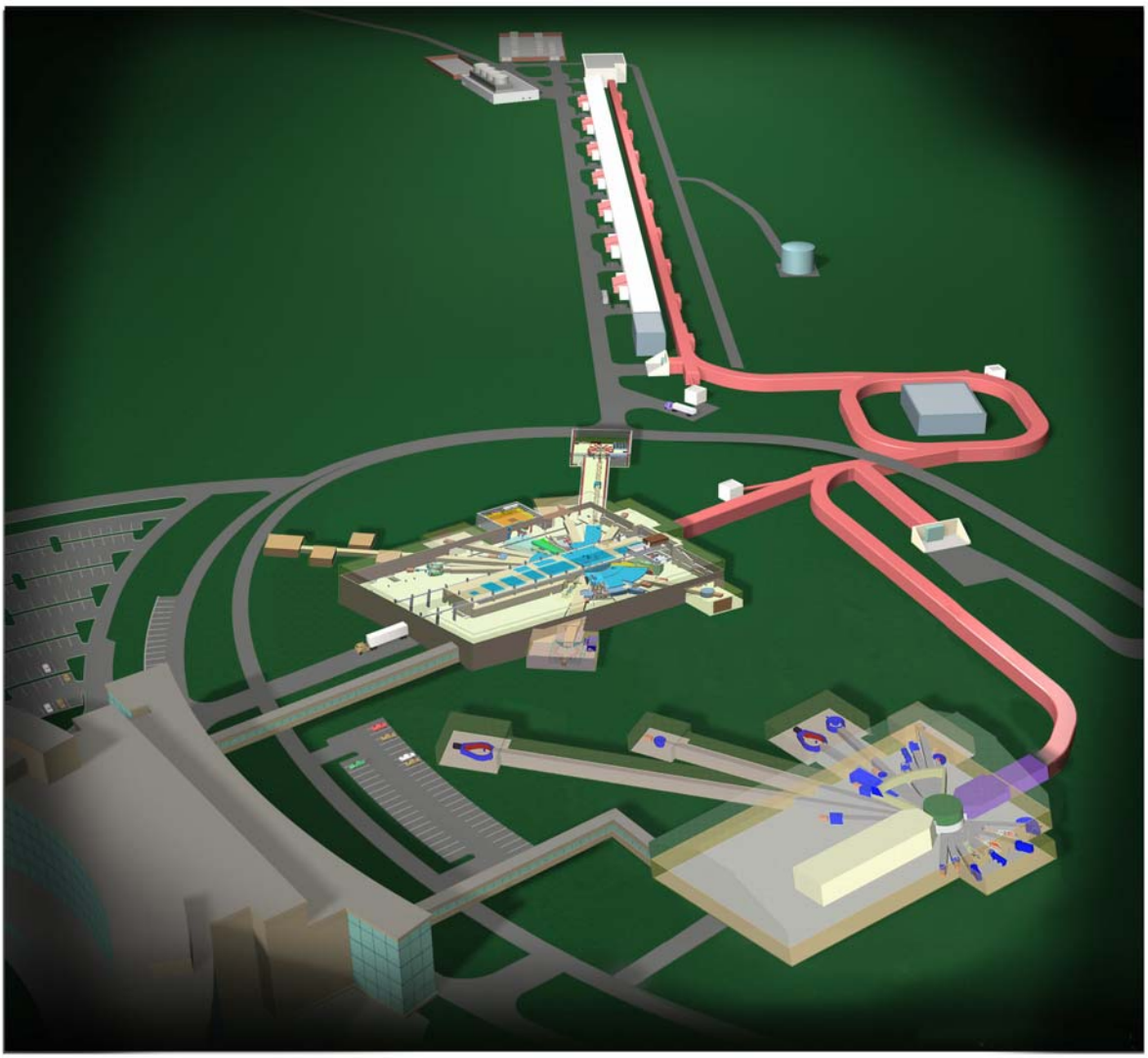

NOVEMBER 2002

ANL-02/16
ORNL/SNS-TM-2001/163

Acknowledgements

All of us who were involved in preparing this report express our thanks and admiration for their work to Carolyn Peters, who prepared the manuscript, and to Mary Fitzpatrick and Rhonda Carpenter, our very capable editors. We accept responsibility for whatever errors remain.

Available electronically at http://www.doe.gov/bridge

Available for a processing fee to U.S. Department of Energy and its contractors, in paper, from:

U.S. Department of Energy
Office of Scientific and Technical Information
P.O. Box 62
Oak Ridge, TN 37831-0062
phone: (865) 576-8401
fax: (865) 576-5728
email: reports@adonis.osti.gov

TECHNICAL CONCEPTS FOR A

LONG-WAVELENGTH TARGET STATION

FOR THE

SPALLATION NEUTRON SOURCE

NOVEMBER 2002

ANL-02/16
ORNL/SNS-TM-2001/163

TABLE OF CONTENTS

TABLE OF CONTENTS (cont)

TABLE OF CONTENTS (cont)

TABLE OF CONTENTS (cont)

TABLE OF CONTENTS (cont)

LIST OF FIGURES

LIST OF FIGURES (cont)

LIST OF FIGURES (cont)

LIST OF TABLES

LIST OF TABLES (cont)

ACRONYMS AND ABBREVIATIONS

ACoM	Advanced Cold Modulator Collaboration
AGS	Alternating Gradient Synchrotron
ASTE	AGS (Alternating Gradient Synchrotron) Spallation Target Experiment
BNL	Brookhaven National Laboratory
BRIMS	broad-range intense multipurpose SANS
CAF, Inc.	Cryogenic Applications F, Inc.
CAS	crystal analyzer spectrometer
CMR	colossal magnetoresistance
CPU	central processing unit
DOE	U.S. Department of Energy

ACRONYMS AND ABBREVIATIONS (cont)

ESS	European Spallation Source
FWHM	full-width half-maximum
GI-SANS	grazing incidence SANS
GMR	giant magnetoresistance
H/D	hydrogen(proton)/deuterium
HER	hydrogen equipment room
HET	ISIS chopper spectrometer
HEW	ISIS chopper spectrometer
HMI	Hahn Meitner Institute
HPTS	High-Power Target Station
HRCS	high resolution chopper spectrometer
HVAC	heating, ventilation, and air conditioning
ILL	Institut Laue-Langvin
INS	inelastic neutron scattering
IPNS	Intense Pulsed Neutron Source
IWG	Interagency Working Group
JAERI	Japan Atomic Energy Research Institute
JINR	Joint Institute for Nuclear Research
JRR-3M	Japan Research Reactor No. 3 Modified
KEK	High Energy Accelerator Research Organization, Tsukuba, Japan
KENS	pulsed spallation neutron scattering facility, Tsukuba, Japan
LAHET	Los Alamos High Energy Particle Transport Code
LANL	Los Alamos National Laboratory
L-CH_4	liquid methane
L-H_2	liquid hydrogen
LOCA	loss-of-coolant accident
LOQ	low Q
LQD	low-Q diffractometer
LWTS	Long-Wavelength Target Station
MAPS	ISIS choppper spectrometer
MCNP	Monte Carlo N-Particle Transport Code
MCNP-X	Monte Carlo Radiation Transport Code
MD	molecular dynamics
MiDaS	magnetism and diffuse scattering spectrometer
MLNSC	Manuel Lujan, Jr. Neutron Scattering Center
NBS	neutron Brillouin scattering
NISP	Neutron Instrument Simulation Program
NIST	National Institute of Standards and Technology
NMR	nuclear magnetic resonance
NSE	neutron spin echo spectrometer
NSF	National Science Foundation
ORNL	Oak Ridge National Laboratory
p/b-cm	protons/$Å^3$
PC-2	DOE building structure type
PSI	Paul Scherrer Institute

ACRONYMS AND ABBREVIATIONS (cont)

PXD	protein crystal diffractometer
PZT	Pb-Zr-Ti-O (lead-zirconium-titanium-oxide)
QCD	quantum chromodynamics
QCP	quantum critical point
QENS	quasielastic neutron spectrometer at IPNS
R&D	research and development
RTBT1	Ring Target Beam Transport proton beamline to HPTS
RTBT2	Ring Target Beam Transport proton beamline to LWTS
SANS	small-angle neutron scattering
SBIR	Small Business Innovative Research
SCD	single-crystal diffractometer
S-CH_4	solid methane
SINQ	spallation neutron source at the Paul Scherrer Institut, Switzerland
SNS	Spallation Neutron Source
SPEAR	surface profile analysis reflectometer
TOF	time of flight
UCN	ultra cold neutron
UHRPD	ultra-high resolution powder diffractometer
UIUC	University of Illinois, Urbana Champaign
WNR	Weapons Neutron Research (at the Lujan Center)

UNITS OF MEASURE

μeV	microelectron volt(s)
μs	microsecond(s)
Å	angstrom(s)
atm	atmosphere(s)
cm	centimeter(s)
cm^3	cubic centimeter(s)
eV	electron volt(s)
GeV	gigaelectron volt(s)
Hz	Hertz
K	Kelvin
kJ	kiloJoule
kW	kilowatt(s)
m	meter(s)
mÅ	milliangstrom(s)
meV	millielectron volt(s)
mm	millimeter(s)
mph	mile(s) per hour
MW	megawatt(s)
s	second(s)
W	watt(s)

1. INTRODUCTION

1.1 Purpose

The Spallation Neutron Source (SNS), a major new user facility for materials research funded by the U.S. Department of Energy (DOE), is under construction at Oak Ridge National Laboratory (ORNL), see the Spallation Neutron Source web site at: www.sns.gov/aboutsns/source/htm. The SNS will operate at a proton beam power of 1.4 MW delivered in short pulses at 60 Hz; this power level is an order of magnitude higher than that of the current most intense pulsed spallation neutron facility in the world, ISIS at the Rutherford-Appleton Laboratory in the United Kingdom: 160 kW at 50 Hz. When completed in 2006, the SNS will supply the research community with neutron beams of unprecedented intensity and a powerful, diverse instrument suite with exceptional capabilities. Together, these will enable a new generation of experimental studies of interest to chemists, condensed matter physicists, biologists, materials scientists, and engineers, in an ever-increasing range of applications.

The Long-Wavelength Target Station (LWTS) complements the High-Power Target Station (HPTS) facility, which is already under construction, and will leverage the significant investment in the remainder of the complex, providing important new scientific opportunities. The fully equipped SNS will offer capabilities for neutron scattering studies of the structure and dynamics of materials with sensitivity, resolution, dynamic range, and speed that are unparalleled in the world.

1.2 Background

From the outset, the arrangement of the SNS has included the capacity for two target stations: a high-power target station, HPTS, and a long-wavelength target station, LWTS (see Fig. 1.1). The funded construction project includes only the HPTS. In November 1999, a consortium was formed to submit a proposal to the National Science Foundation (NSF) requesting funding to develop a conceptual design for the LWTS. The purpose of the conceptual design was to extend the capabilities of the SNS to address the large field of new applications for long-wavelength neutrons. The basis of the proposal took shape during six months of preliminary target system conceptual design and meetings on instrumentation and the science case for the station.

The 1999 proposal resulted in funding by the NSF of a one-year study that included technical design activity, development of the scientific case for the LWTS, and development of a suite of neutron-scattering instruments. Thom Mason, project director of SNS, served as principal investigator of the consortium with Lee Magid, professor of chemistry at the University of Tennessee, Knoxville, as coordinator of the science case; Jim Richardson, group leader, Neutron Scattering, Intense Pulsed Neutron Source (IPNS) as coordinator of instrumentation; and Jack Carpenter, technical director of IPNS, as coordinator of target systems development. The experienced Argonne National Laboratory (ANL) IPNS target systems design team completed the conceptual design activity, while the IPNS instrument scientists conceived and evaluated scattering instruments. Groups of university scientists representing a number of disciplines assembled the scientific cases for the LWTS. To ensure a broad input into the specification of instruments and the overall design of the LWTS, a series of small workshops on specific areas

(soft matter, disordered materials, magnetism, crystallography, fundamental neutron physics) was held in early 2000, followed by the Users Meeting and Instrumentation Workshop on May 22–24, 2000, in Washington, D.C. These activities converged in an instrumentation and science review held in November 2000 at ANL.

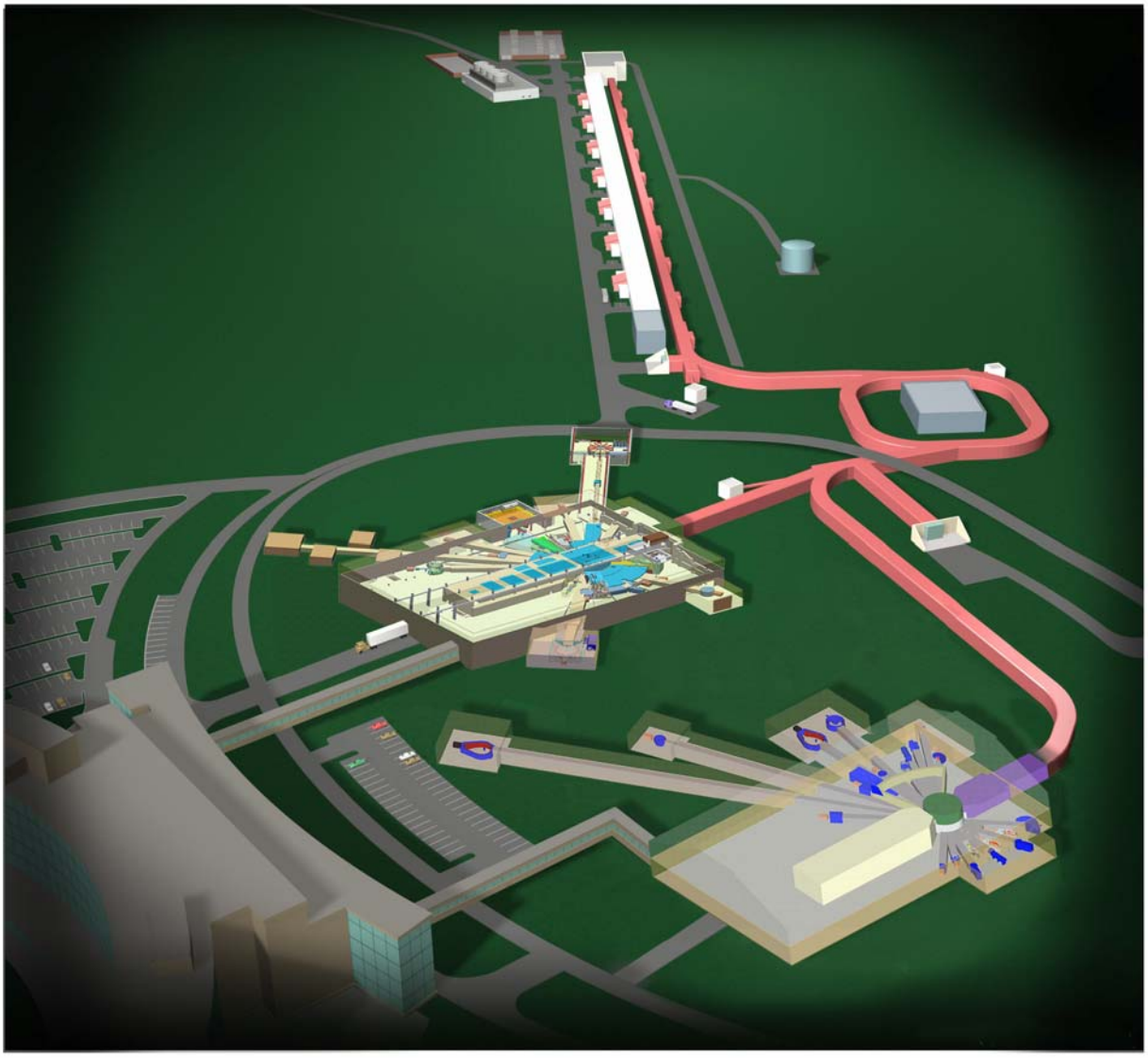

Fig. 1.1. A computer-generated aerial view of the SNS, showing, at the top, the ion source, the preaccelerator, the 1-GeV linac, and the storage ring, at center right. The extracted beam travels to the HPTS, at center right. The Central Laboratory and Office building is at the lower left. The proposed LWTS is at the lower right.

In February 2001, the consortium submitted a proposal for construction of the LWTS, funded by the NSF and involving DOE and an extended interagency partnership, and envisioned continuous design refinement and research and development (R&D) activities extending beyond May 2001. However, the size and complexity of the partnership and its implications led to a hiatus in the program and to the convening of an interagency working group (IWG) involving the NSF, DOE,

the U.S. Department of Commerce, and the National Institutes of Health. The one-year design activity concluded in April 2001. The February 2001 proposal was withdrawn and the development work put on hold until IWG establishes the necessary framework for interagency collaboration. This report summarizes the conceptual basis for the LWTS, documenting the accomplishments of the NSF-funded study. It will serve as a basis for future discussions of the implementation of the LWTS.

1.3 LWTS Benefits

When the LWTS is constructed, it will provide the scientific community with unprecedented capabilities using the world's most powerful beams of long-wavelength neutrons in an installation carefully optimized for scientific applications.

Only the LWTS and its neutron-scattering instruments will provide opportunities to investigate materials in which the characteristic lengths extend to 10,000 Å and time scales range up to 10^{-7} seconds. The gains for such measurements, well matched to the capabilities of the LWTS, average about three times — and in some cases more than an order of magnitude — greater than those that can be achieved at the HPTS. The second target station will immediately increase the science output of the SNS beyond what could be accomplished by using HPTS alone. Most important, in the long term, the LWTS will more than double the scientific capability of the SNS, for about 20% of the capital cost.

The simplest measure of performance is the neutron intensity scattered from a sample. One of the LWTS design goals has been to deliver, on average, a factor of three more neutrons per pulse than the HPTS. Given the substantial leap forward that the HPTS represents over current sources (gains of order 100 for combined source/instrument performance), the LWTS will open up qualitatively new areas of investigation that are not feasible at existing sources simply because the majority of neutron-scattering experiments are flux limited. Further, this factor-of-three gain over the HPTS does not take into account more subtle, but significant, advantages such as improved pulse resolution, reduced backgrounds for longer-flight-path instruments, greater wavelength band due to the reduced repetition rate, and wider d-spacing coverage for restricted geometries such as pressure cells (again because of the lower repetition rate).

In general, increased intensity in and of itself is the least exciting feature of improved performance expected from the LWTS. Of greater significance is the new science that the facility will enable because of the improved resolution it offers. The combination of moderators tailored to produce long-wavelength neutrons with appropriate pulse width and the 100-ms interval between pulses provide unique capabilities in the LWTS. For example, a backscattering spectrometer with 200 neV resolution that is 10 times better than anything available in the United States today will reveal new information on growth processes and chemical reactions through spectroscopy of rotational tunneling, translation, diffusion, and hindered motion that is complementary to nuclear magnetic resonance (NMR). High intensity is useful for studying smaller or weakly scattering samples and is important in determining details of protein structure such as the location of water in the ribosome. These studies require neutron sensitivity to hydrogen in cases where the water is not well bound, but they are not possible at present sources because of the requirements for large crystals. Off-specular reflectivity, providing access to in-plane momentum transfer, will reveal details of two-dimensional structures in magnetic

multilayers, on surfaces, and in complex polymer assemblies. In fundamental physics investigations, improved signal-to-noise, polarized beams, and use of time structure to eliminate systematic errors will offer better insight into the weak interaction.

The proposed plan ensures that an experienced, diverse, and dynamic scientific contingent will exploit the capabilities of the LWTS and that the facility will serve the full potential of the university-based user community. The two facilities, HPTS and LWTS, both offer opportunities for the scientific community to participate in formulating the case for, prioritizing, and taking part in the design and development of the SNS instruments. The combined capacities of the two target stations represent wide opportunities for instruments conceived by teams from universities, industry, and government laboratories.

1.4 Why Neutrons?

Neutron scattering is a unique and powerful tool used by scientists to study the structure and dynamics of materials at the atomic, molecular, and macromolecular levels. The past 30 years have seen an immense broadening of the fields of science addressed by neutrons, driven to a large extent by developments in the use of long-wavelength (cold) neutrons. Cold-neutron applications have grown with special vigor in recent years — examples abound at the research reactors at the National Institute of Standards and Technology (NIST), Institut Laue-Langvin (ILL), the modified Japan Research Reactor-3 (JRR-3M) at the Japan Atomic Energy Research Institute (JAERI), and at IPNS and the ISIS pulsed spallation neutron source, which show that good cold-neutron scattering facilities attract large numbers of users. Cold-neutron instruments represent the largest contribution to the shift from neutrons' being principally a tool of physicists to their being a probe used by the much broader community of scientists.

Neutrons offer the following advantages as scientific probes:

- Neutrons are electrically neutral; they penetrate centimeters of most materials, enabling *in-situ* studies.

- Neutron cross sections exhibit no regular dependence on atomic number and are similar in magnitude across the periodic table, so they are sensitive to light elements in the presence of heavy ones.

- Certain large differences in isotopic scattering cross sections (e.g., H/D and ^{6}Li/^{7}Li) make neutrons especially useful for the study of light atoms in materials.

- The range of momentum transfers available allows researchers to examine a broad range of length scales (0.1 to 10^{5} Å); this capability is important for many different materials and applications.

- Thermal and cold (long-wavelength) neutrons cover a range of energies sufficient to probe a wide range of atomic or magnetic excitations (1.0 to 10^{-7} eV), as well as slow dynamic processes such as polymer chain reptation, on time scales up to 10^{-7} seconds.

- Neutrons have magnetic moments and are sensitive probes of magnetic ordering and excitations.

- Neutrons can be polarized, allowing separation of the nuclear and magnetic cross sections.

- The simplicity of the magnetic and nuclear interactions facilitates straightforward interpretation of results.

2. GENERAL DESCRIPTION OF THE PROPOSED LWTS

This section briefly describes the reference technical concept for the proposed LWTS target system design, arrangement of neutron-scattering instruments, and proton beam and accelerator systems.

The LWTS design concept incorporates a number of innovative, yet well-verified elements derived from the experience of the designers and from knowledge of recent successful developments elsewhere. Applied to the LWTS, these contribute to the accomplishment of the LWTS goals, which are themselves a departure from precedent. An expert review of a preliminary version of the LWTS conceptual design, held in January 2000, endorsed the ideas presented here.

2.1 Overview

Throughout the concept development, the LWTS facility and instrument design groups maintained close collaboration with the scientific community and those formulating the science case to produce the best possible facility.

The guiding theme of the LWTS design is to build a facility that augments the capabilities of the HPTS. Emphasizing the use of long-wavelength neutrons means using the coldest possible moderators with low pulsing frequency and consequent low target power; all of these are complementary requirements. Tentatively and to give scale to the development of the concept, we assumed that the LWTS will operate at 10 Hz and 333 kW (1/6 of the nominal SNS beam power). The goal is to exceed the intensity of the HPTS by at least a factor of three on a per-pulse basis for long-wavelength neutrons. The proposed design surpasses the goal, quite substantially in some cases. We adopted several target system innovations on the basis of recent successful developments elsewhere that apply to the use of long-wavelength neutrons. In January 2000, we subjected the preliminary design to review by a panel of world experts, who approved the proposed design.

Work so far has led to a preliminary configuration of the target, experimental hall, and instruments that are — for reasons of economy — similar to those of the HPTS, with a number of innovative features and a distinct design. The proposed target is a vertically extended, water-cooled solid tungsten target. However, we have continued to evaluate the mercury target alternative (similar to that used in the HPTS), which could provide operational advantages. All three proposed moderators are cryogenic (20 K pelletized, solid methane cooled by supercritical hydrogen, and 100 K circulating liquid methane), with extensive use of guides in two configurations: large-aperture gently curved guides and compact benders. The design also includes some beams with line-of-sight view of at least one moderator. The use of guides and benders allows two viewing moderators to be arranged in “slab” configuration. The third moderator, viewed through straight holes, is arranged in a “wing” configuration upstream from the target. Moderators move vertically for service and replacement. The asymmetric experimental hall has heavy crane coverage and attached galleries for distant long-flight-path instruments, which have lighter-duty crane coverage.

Before May 2001, we completed extensive neutronic and engineering optimizations and evaluations of alternatives to the base-case assumptions. Later sections of this document describe the LWTS conceptual design in technical detail, including the results of engineering evaluations, and contain an extensive discussion of the scientific case and of the instrument concepts.

The current version of the LWTS concept provides 21 neutron beams, three of which view the 100 K moderator directly, while the remainder view 20 K moderators — one decoupled for high resolution, the other undecoupled to provide highest intensity — through curved guides. From a preliminary selection of 20 instruments, we chose three on which to concentrate first. In the longer term, we will prepare specifications for a larger number of instruments. The following paragraphs describe, very generally, the target systems, neutron-scattering instruments, and protein beam and accelerator systems.

Figure 2.1 illustrates the target and the target/moderator/reflector concept of the LWTS.

Figure 2.2 illustrates the target.

Figure 2.3 shows the preliminary layout of target, guides, and instruments; the layout matches moderator types, flight path, and guide systems with conceptual instruments.

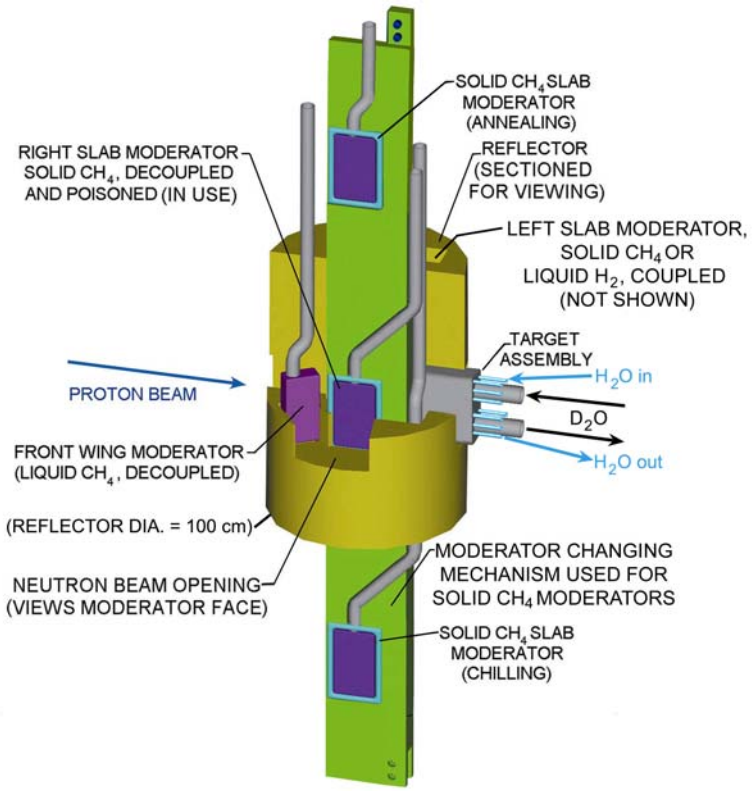

Fig. 2.1. Target/moderator/reflector concept.

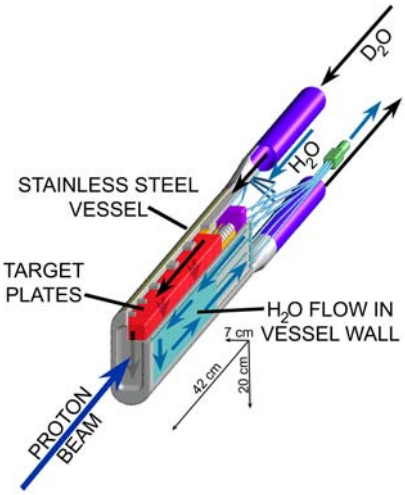

Fig. 2.2. Target concept.

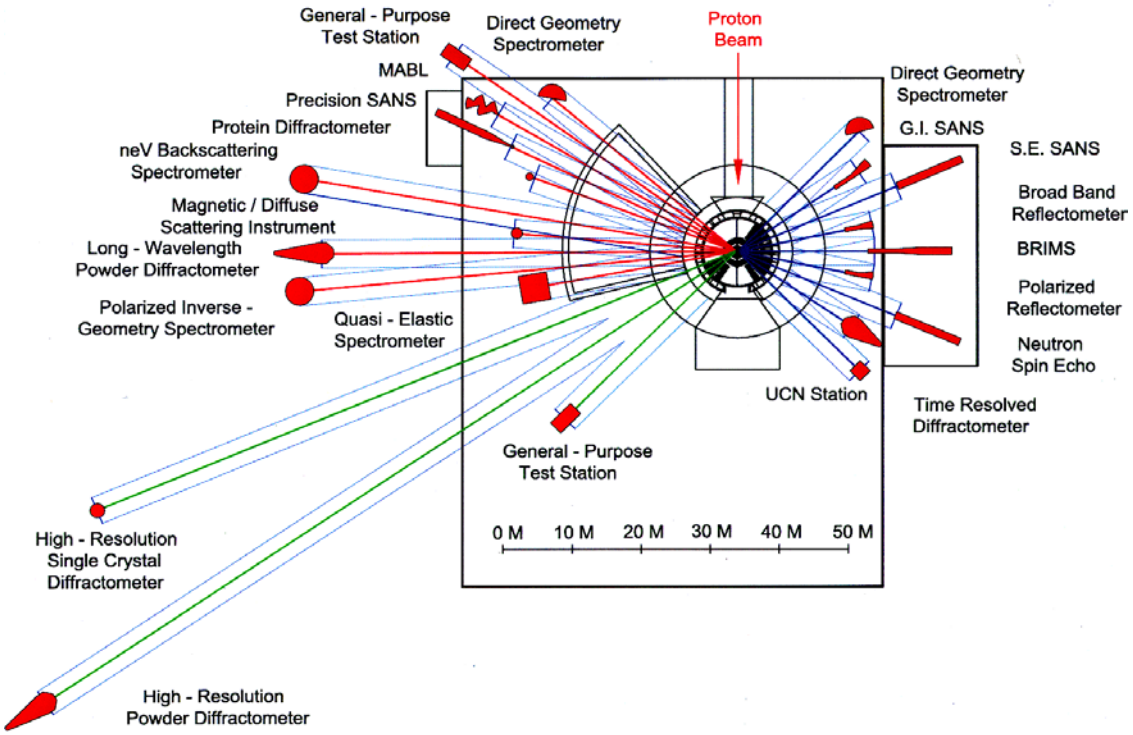

Fig. 2.3. Preliminary layout of target, guides, and instruments.

2.2 Target Systems Design

The LWTS reference concept includes a vertically extended target constructed of high-density metal plates (e.g., tantalum, clad tungsten) measuring 7 cm wide × 20 cm high × ~40 cm thick, with deuterium oxide (D_2O)("heavy water") cooling (see Fig. 2.2). The proton beam footprint is a 5- × 15-cm elliptical shape with a flat distribution similar to that of the HPTS. The nominal proton beam power is 1/3 MW, corresponding to 10-Hz operation. Preliminary engineering assessments indicate that thermal power densities allow convective cooling without excessive

dilution of the target material and that thermal shock stresses are acceptable. The shape of the target maximizes neutron production and coupling to the moderators while minimizing proton leakage to the surroundings. The total target length is sufficient to exhaust the nuclear cascade and leave little power in the downstream shielding.

The proposed design affords high atomic number and mass density for high neutron yield, high strength, and good material properties at high temperatures. Coolant passes across the faces of the target plates, maintaining single-phase convective heat transfer at the surfaces and limiting plate-center temperatures. Where needed, a thin cladding of the target plates furnishes corrosion resistance. Plates are spring loaded to take up dimensional changes caused by thermal- and radiation-induced growth. The target vessel is welded stainless steel with D_2O-flow plena that distribute the coolant. Additionally, the flat target vessel walls are filled and cooled with water to provide a premoderator volume and assist in heat removal from the target region.

2.2.1 Target-Moderator-Reflector

Reflectors placed around the target and the moderators, as shown in Fig. 2.1, reflect neutrons into the moderators. Active cooling removes the considerable heat generated in the reflectors and moderators by the slowing of neutrons and the absorption of gamma radiation. The target-moderator-reflector assembly has space for all the beam ports and coolant piping. The reflectors are D_2O-cooled beryllium. The side slab moderators are of solid methane (S-CH_4) or liquid hydrogen (L-H_2), and the front-wing moderator consists of liquid methane (L-CH_4).

The target-moderator-reflector assembly includes portions of the piping for each cooling system, portions of the neutron beam channel, and mechanisms for moving or changing out components. This arrangement allows the target to be removed horizontally into a hot cell. Independently of the target location, any of the moderators can be individually removed from the reflector. Raising the moderator-reflector assembly allows easy replacement of components. During operation, the target-moderator-reflector assembly rests inside a sealed space defined by a stationary liner inside the biological shield. The sealed space contains the radioactive gases and activated solids produced in the target-moderator-reflector assembly. A helium atmosphere surrounds the target-moderator-reflector; the neutron beamlines are helium-filled or provided with vacuum, and a helium atmosphere bathes the shielding.

2.2.2 Beamlines and Shielding

The biological shield consists of an inner core of iron and iron-loaded concrete and an outer layer of concrete, as shown in Fig. 2.4. The shield permits all parts of the hall that houses the scattering instruments to be occupied during operation. The innermost portion of the shield is equipped with an active cooling system. Protons from the accelerator system enter the biological shield from the high-energy proton transport line through a water-cooled, double-walled vacuum window. The window is the interface between the vacuum of the proton beamline and the helium atmosphere of the target tank.

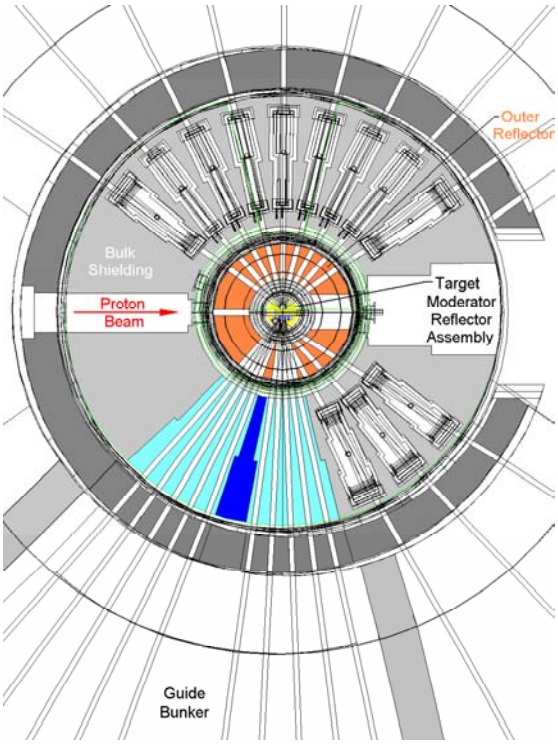

Fig. 2.4. Shield and beam transport arrangements in the LWTS.

Beam benders, curved guides, and associated shielding bend the beams away from the straight-through component of fast and high-energy neutrons, which stop in the shielding. The two curved-guide clusters shown at the bottom of Fig. 2.4 emerge into a shielded bunker; their lines of sight end within the curved guides in the bunker. At the top of the figure, guides extend through movable gates to shielded compact beam benders, then through guides to neutron beam instrumentation.

2.3 Neutron-Scattering Instruments

Instruments for the LWTS are being selected on the basis of how well they match the overall science needs of the SNS. The instruments will capitalize on the following features of the LWTS design concept: high flux of long-wavelength neutrons, use for magnetic scattering, etc.; long flight paths, enabling high resolution; very wide accessible wavelength band, for example, for kinetic experiments requiring minimal adjustment of instrument parameters during measurement; and extensive use of neutron optic devices, which work best at long wavelengths. Figure 2.3 illustrates one possible arrangement of instruments around the source.

Instrument designs follow an established protocol developed for the SNS HPTS and other facilities. Because the slab geometry for the LWTS moderators requires the use of curved beamlines, designers must pay careful attention to neutron guide components that efficiently transport long-wavelength neutrons and minimize loss of useful short-wavelength neutrons.

2.4 Proton Beam and Accelerator Systems

The operation of the LWTS concurrently with the HPTS presents no insurmountable problems. The most significant requirement is that the accelerator systems be capable of delivering a 2-MW beam to HPTS with pulses that do not exceed 34 kJ during each acceleration cycle, while providing the LWTS with its proton beam.

An optical model developed for the beamline to the LWTS (RTBT2), includes a pulsed dipole and a pulsed quadrupole for achromatic beam matching into the LWTS.

Additional requirements for LWTS operation include two beamline protection devices, which are required for operation of the LWTS during periods of maintenance for HPTS and vice versa. The scheme for providing redundant protection is a Fermi National Accelerator Laboratory–style beamstop, which will be installed in RTBT1, the beamline to HPTS, between a pair of collimators. Brookhaven National Laboratory (BNL) has undertaken development of concepts and detailed design of the RTBT2.

2.4.1 Pulse- and Power-Sharing

The most promising option to achieve the pulse- and power-sharing goals for the LWTS is to increase the energy of the linac, which is possible in the SNS superconducting machine. With the energy of the linac at 1.3 GeV and the ion source peak current at 52 mÅ, the linac pulse length (i.e., the number of accumulated turns in the ring) would be reduced to maintain the 34-kJ-per-pulse limit on HPTS. We could then extend the surplus duty cycle to provide an independent pulse train at about 10 Hz to the LWTS. The linac would then run dual pulse trains with the 10-Hz LWTS pulse train interleaved between 60-Hz HPTS pulses exactly 180 degrees out of phase with the HPTS pulses. This arrangement would allow the maximum time between pulses for recovery of kicker voltages, etc., while preserving regular 60-Hz HPTS operation and providing low-frequency, lower-power beam to the LWTS. Table 2.1 illustrates this option. (The length of the pulse delivered to the target would remain unaffected at about 0.5 μsec.).

Table 2.1. Sharing of pulse and power between HPTS and LWTS.

Target Station	Pulse Rate (Hz)	Linac Pulse Length (μsec)	Ion Current (mA)	Energy (GeV)	Power (MW)
HPTS	60	1000	52	1	2.04
HPTS	60	770	52	1.3	2.04
LWTS	10	up to 1000	52	1.3	up to 0.44

2.4.2 Buildings and Conventional Facilities

The design and construction of the buildings and conventional facilities supporting the LWTS and ancillary equipment are, to the extent practicable, the same as those of the facilities supporting the HPTS. The goal of this approach is to minimize the cost of these facilities by using available and proven designs for the HPTS, while maintaining a LWTS concept and layout that optimizes the facility's unique aspects for long-wavelength neutron scattering.

The concept and general layout of the LWTS buildings and conventional facilities (see Fig. 1.1) was developed at Argonne and ORNL as a part of the specifications of the LWTS proton beam delivery, neutron generation, scattering instrument, and ancillary equipment systems. Argonne will work with ORNL and the SNS design team at ORNL, because ORNL will eventually be responsible for the costing, schedule, detailed design, and construction of the LWTS, including the buildings and conventional facilities.

Table 2.2. Parameters of the LWTS.

PARAMETER	
Pulsing frequency	10. Hz
Proton energy	1.0 GeV
Beam power on target	333 kW
Energy per pulse	33.3 kJ
Target material	Tungsten
Primary coolant	D_2O
Premoderators	H_2O
Moderators (3) All 20-cm h x 12-cm w	High Resolution Cold Moderator: Poisoned decoupled slab, flat L- H_2-cooled S-C H_4 @ 20 K
	High Intensity Cold Moderator: Coupled slab, grooved L- H_2 or L- H_2–cooled S-C H_4 @ 20 K
	High Resolution Broadband Moderator: Poisoned decoupled front wing, flat L- CH_4@ 100 K or L- H_2–cooled S-C H_4 @ 20 K

3. TARGET SYSTEMS DESIGN

3.1 LWTS Target Design Features and Assembly

The LWTS target consists of D_2O-cooled, high-density metal plates in a water-cooled stainless steel vessel, as shown in Fig. 3.1. The stainless steel target vessel is a weldment fabricated from five separate pieces, also shown in Fig. 3.1. This target design and depiction are adapted from a solid target backup concept developed for the SNS [3.1.1] and from an earlier concept for a 1-MW IPNS upgrade [3.1.2].

3.1.1 Design Features

The largest, central vessel piece is machined from a solid forging. The D_2O supply and return cooling headers on the top and bottom are left open to facilitate machining of the interior features and the rear of the proton beam window. A large rectangular box cavity is machined from the center of the forging to hold the target plates. The side surfaces of the large forging are machined to receive flat plates that form the cooling water passages for the vessel.

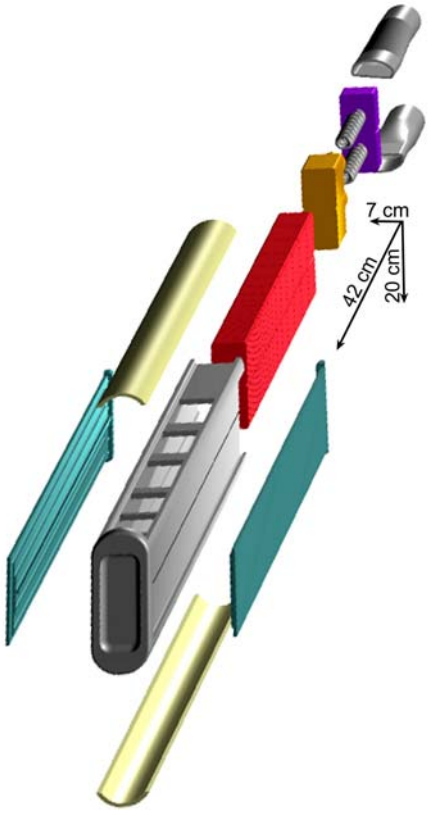

Fig. 3.1. Stainless steel target vessel weldment.

The cooling passages are milled into the inner side of the flat side plates, and the plates are welded to the large forging. The individual cooling passages in each plate are separated by ribs that slide into dovetail grooves in the large forging. This arrangement provides good separation between the flow passages and reduces the deflections and stresses in the vessel and the plates.

3.1.2 Assembly

The side plates are welded on the vessel, and the half-pipe sections are welded on the large forging to form the D_2O supply and return headers and complete the weldment. After this step, the spring-loaded pusher plate and springs are installed. Then the backing plate is installed with the proper preload, and it is welded to the target vessel to hold it in place. At this point, the D_2O pipes that supply the D_2O headers and provide support for the target are ready to be assembled. First, a transition piece is welded to the target vessel attached to each header, and then the pipes are welded to the transition pieces. Then a target chamber flange is welded to the opposite ends of the D_2O supply and return pipes.

Finally, stainless steel tubes are brazed between the rear of the target vessel and the target chamber flange to provide cooling water to the target vessel.

3.2 Moderator and Neutron Beam Port Locations

Figures 3.2, 3.3, and 3.4 illustrate the locations of the target, moderators, and reflector as well as the neutron and proton beamline cutouts in the reflector.

A 20-mm-thick H_2O premoderator and target vessel cooling layer separate the slab moderators from the target. Guides can approach to within about 1 m of the target center. Cut A-A in Fig. 3.3 is the location used for Fig. 3.2.

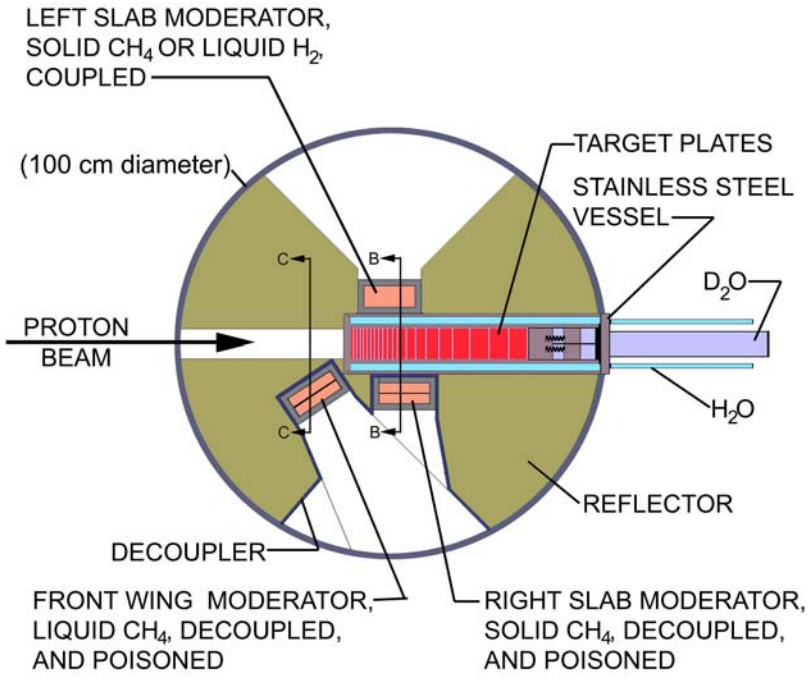

Fig. 3.2. A cross-sectional view taken at the horizontal midplane of the target and showing the relative positions of the target-moderator-reflector components. Cuts B-B and C-C are the locations of the views in Figs. 3.3 and 3.4.

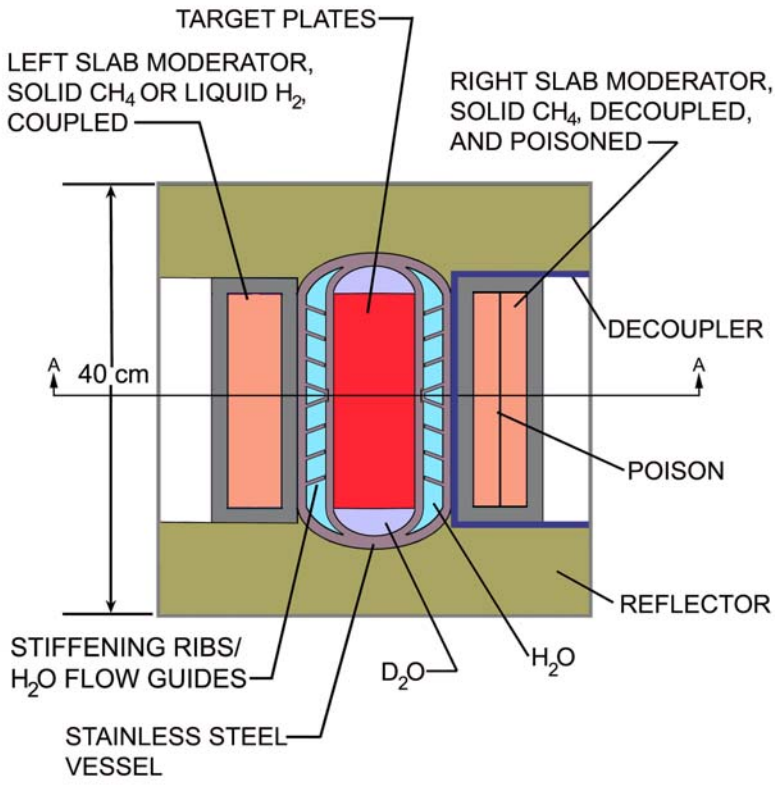

Fig. 3.3. Cross section at the vertical midplane (cut B-B) through the target and slab moderators. These are usually 22 K solid methane moderators, one decoupled and poisoned, the other coupled. The coupled moderator may, at times, be a liquid hydrogen moderator. The two slab moderators each serve instruments on their respective sides.

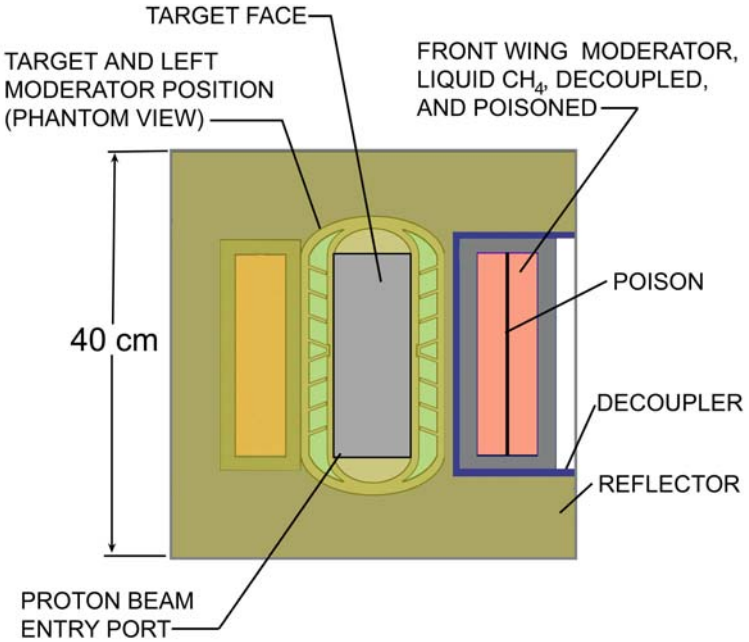

Fig. 3.4. Cross section (cut C-C) through the front moderator, a decoupled, poisoned liquid CH_4 moderator. This moderator serves three beams.

3.3 Moderators

3.3.1 Moderator Materials

We have selected moderator materials for LWTS on the basis of extensive knowledge of the experience and developments worldwide. After careful evaluation, we adopted innovative technologies that will provide the highest level of performance of the LWTS. In some instances, implementation will require continued R&D efforts. Participants in the LWTS design continue to take part in those efforts in the course of their regular work.

Moderators for an LWTS-scale source must not only provide effective coupling to the primary source and spectra and pulse characteristics appropriate for the instruments, but also must be able to withstand the high-radiation environment. (Recall that the source power of LWTS, 333 kW, is more than twice that of ISIS [160 kW] and about 20 times that of IPNS [equivalent to about 15 kW on account of its uranium target].) The following candidate materials are likely to satisfy performance and radiation-tolerance requirements:

- Liquid hydrogen (L-H_2) at 20 K
- Liquid methane (L-CH_4) at 100 K
- Solid methane (S-CH_4) at 20 K

Each of these materials has its problems, which are the subject of ongoing research at various institutions; other materials are also currently being studied.

We chose L-H_2, L-CH_4, and S-CH_4 as the basis for LWTS performance estimates and engineering analyses. In the case of the coupled moderator, we leave open the question of L-H_2 or S-CH_4, which present different advantages. We offer evaluations of both because we expect that the demands of the instruments will dictate the final choice.

3.3.1.1 Liquid Hydrogen

Because the products of radiation damage are only different forms and combinations of hydrogen atoms, which disappear or recombine to the original material, L-H_2 suffers no permanent macroscopic radiation damage effects, which makes it attractive for use in the LWTS. In L-H_2 (actually, supercritical H_2 at about 15 atm pressure to avoid the possibility of bubbles) flows through the moderator system, cooled in an external heat exchanger. There are two molecular spin states: ortho hydrogen (spin 1, the two proton spins aligned) and para hydrogen (spin 0, the two spins antialigned). The para state is favored in thermodynamic equilibrium (approximately 99.8% at 20 K). Moreover, the two have very different low-energy neutron scattering cross sections and produce considerably different spectra and pulse characteristics. Measurements on operating pulsed sources provide no definitive answer about what ortho-para ratio is best in a given situation. Further, ionizing radiation tends to force the thermodynamic equilibrium toward the "normal" state of room-temperature hydrogen with an ortho-para concentration ratio of 3:1. This effect, which has not been well accounted for in measurements to date, leaves doubt as to the concentration ratio of the measured materials and may require that engineering measurements be taken to control the ratio at the desired value. Most studies assume pure para hydrogen, as we have done in LWTS studies of L-H_2 moderators. The drawbacks of L-H_2 are its rather low

proton density, which makes for longer pulses than those from more dense materials, and the lower low-energy intensities and nonmaxwellian spectra that follow from the low scattering cross section of para hydrogen below about 15 meV. Some of these subjects were addressed at the International Workshop on Cold Moderators for Pulsed Neutron Sources, held at Argonne in 1997 [3.3.1]. All these questions were addressed at a special topical session of the American Nuclear Society in June 2001. Because of its performance drawbacks and in spite of its apparent operational advantages, we did not choose L-H_2 for the LWTS, but will consider it as a backup.

3.3.1.2 Liquid and Solid Methane

The condensed phases of methane are very attractive in cold moderator applications because their high proton densities translate into short pulse widths. Also, methane has a high density of rotational states (spacing about 1.0 meV) that facilitates loss of the last bits of energy in the thermalization process and produces a good maxwellian spectral shape with an effective temperature near its physical temperature. However, L-CH_4 suffers permanent radiation damage because the products of radiolysis combine into nonvolatile and solid products that deposit in the moderators and piping. S-CH_4 may be subject to similar effects, although these have not been definitively observed in practice. Accumulation of the radiolysis products is quantitatively different in the two materials because of the different mobilities of intermediate entities in the low-temperature solid and the higher-temperature liquid.

Liquid Methane

Liquid methane moderators in IPNS and ISIS exhibit radiation aggregation problems; however, even in ISIS, the operational problems are few enough that they are tolerated because of the neutronic advantages offered by L-CH_4. The L-CH_4 moderator in the LWTS is located where the radiation damage rate is similar to that in the ISIS case in spite of the higher power of LWTS. Furthermore, a premoderator around the LWTS moderator will reduce the radiation damage rate by about a factor of two with little penalty on the intensity. We are confident that the L-CH_4 moderator will have sufficient service lifetime (about six months in the ISIS case) to qualify for use in LWTS. The vertical moderator access provided in the LWTS, which does not require moving the target or reflector, will make for relatively easy replacement compared to that at ISIS and IPNS. An alternative to liquid methane — liquid propane — has been used successfully for many years at the 5-MW reactor at the Kurchatov Institute in Moscow, Russia [3.3.2]. Tests of a liquid propane moderator in a pulsed spallation neutron source have not yet been conducted.

Solid Methane

Solid methane moderators may have problems of solid product accumulation similar to those encountered when using liquid methane. (Recently, after six years of operation, the IPNS S-CH_4 "H" moderator had to be replaced, possibly for this reason, but it has not yet been examined.) In addition, cold (~20 to 30 K) S-CH_4 exhibits a radiation-induced thermochemical instability, "burping," in which reactive, metastable radiolysis products, assumed to be CH_3^+, accumulate in the solid matrix. When their density reaches a critical value, these products spontaneously recombine, heating the material and increasing their recombination rate until all the stored energy is released. Fairly high temperatures can result [3.3.3]. In addition, H_2, which collects in the solid matrix, is released when the temperature exceeds about 65 K, increasing the pressure in

the container. Periodic annealing, carried out about every two and a half days in IPNS, releases the stored energy before it accumulates to dangerous levels. The LWTS design incorporates several moderators to alternate in service in each of the slab positions. This arrangement facilitates exchange for annealing and replacement on a regular schedule.

Because the thermal conductivity of solid methane is rather low, in IPNS and in the neutronically-evaluated LWTS basis concept, the moderator vessel contains 10%-dense aluminum foam that is thermally anchored to the cooled surfaces to transport the heat. The engineering analysis of the effectiveness of this concept is not yet complete. However, we follow closely the experience at the 2-MW IBR-2 reactor at the Joint Institute for Nuclear Research (JINR) in Dubna, Russia, where a solid methane moderator has been operating successfully for several years [3.3.4]. We maintain frequent communication with scientists at Dubna who, with support from the laboratories involved in the Advanced Cold Moderator Collaboration (ACoM), are working on the problem of methane irradiation-induced thermochemical instability.

A new development is pelletized solid moderator media, cooled by flowing cold helium (He) gas or L-H_2. There are at least two research efforts underway to investigate this concept. In both, the participants communicate through ACoM. The more advanced effort is by C. A. Foster of Cryogenic Applications F Inc. (CAF Inc.), of Oak Ridge, Tennessee, under DOE Small Business Innovative Research (SBIR) sponsorship. CAF Inc. has succeeded in forming 3-mm prisms of solid methane and of solid ammonia in substantial quantities, and has demonstrated their transport to a collection vessel and developed a method of removal by rapid sublimation. Methane pellets are sticky at the 70 K temperature of formation, while ammonia pellets are not, and flow freely to fill a container. Figure 3.5 shows a stack of S-CH_4 pellets in the collection vessel. The packing fraction — that is, the ratio of the volume of the solid to the total volume — is approximately 62%. In application, L-H_2 would flow through the pellet-filled vessel, cooling the material and adding to the proton density.

Fig. 3.5. Methane pellets in a collection vessel [3.3.2].

The combination of methane, with a proton density of 7.8×10^{22} protons/cm^3, and L-H_2, with a proton density of 4.4×10^{22} protons/cm^3 filling a container with 62% solid, provides an average proton density of 6.5×10^{22} protons/cm^3, which is nearly equal to the proton density of the 90% methane in the foam-filled system assumed in the neutronic analysis: 7.0×10^{22} protons/cm^3. (For reference, the proton density of water at 300 K is 6.7×10^{22} protons/cm^3.) Thus the analyses closely approximate the prospects for the L-H_2–cooled pelletized methane moderator. We have completed Monte Carlo calculations of L-H_2–cooled pelletized S-CH_4 moderators with colleagues in the Nuclear Engineering Department of the University of Illinois, Urbana-Champaign (UIUC). The calculations indicate that pellets of reasonable sizes (e.g., ~3.0 mm) behave neutronically as homogenized systems. These results will allow us to carry out more detailed optimizations of L-H_2–cooled pelletized S-CH_4 moderators in a simple way. Continuing work at CAF Inc., supported by a Phase II SBIR grant, aims for larger-volume production of pellets and a cooling system to reduce the temperature of produced S-CH_4 pellets and render them unsticky. A video presentation of the production and processing of methane and ammonia pellets is available from CAF Inc., Oak Ridge, TN.

3.3.1.3 Ammonia

Experience with pellet production at CAF Inc. has encouraged interest in using ammonia (NH_3) as cold moderator material. The mechanical properties of the as-formed pellets are already suitable for use in a pelletized moderator. Furthermore, the proton density of solid ammonia, 9.3×10^{22} protons/cm^3 at 23 K [3.3.5], substantially exceeds even that of solid methane. Additionally, the rotor modes of the ammonia molecule are of comparable spacing to those of the methane molecule, spaced about 1.0 meV apart. If these remain in the cold solid, ammonia may serve as a suitable cold moderator in the LWTS. A drawback of natural ammonia is its rather large absorption cross section, caused by capture in ^{14}N; these losses render it inferior to other choices as a moderating medium. However, the separated isotope ^{15}N has almost no capture cross section for low-energy neutrons. Using old data on natural ammonia and invoking a new procedure for correcting for the absorption effect [3.3.6], we found that the spectral intensity of the separated-isotope ammonia, $^{15}NH_3$, exceeds that of solid methane in the conditions tested (77 K). The cost of a charge of $^{15}NH_3$ would be approximately $100,000, too much to contemplate for a direct test but affordable in a major installation such as the SNS, provided that a system of replenishment — i.e., a small-scale, special-purpose isotope separator — were available.

In an L-H_2–cooled, pelletized $^{15}NH_3$ moderator with 62% solid, the proton density would be 7.4×10^{22} protons/cm^3. A new set of moderator spectrum and pulse width data, such as might be obtained, for example, at the Hokkaido linac with natural ammonia and using the correction procedure, would enable a definitive assessment of the prospects for solid $^{15}NH_3$ moderators. In addition, quasi-elastic neutron-scattering data, which are easy to obtain at the IPNS spectrometer QENS, would show whether low-energy energy-transfer modes remain in the solid to the extent useful for low-temperature moderation. The radiation-thermochemical instability problems and the problems of managing radiation products in ammonia moderators still need to be addressed. Nitrogen compounds do not agglomerate in long chains like carbon compounds involved in radiolysis of hydrocarbons; therefore, we maintain active interest in a L-H_2–cooled pelletized $^{15}NH_3$ moderator option for use in the LWTS. Section 9 further discusses palletized moderators as a significant R&D need.

3.3.2 Summary

Table 3.1 lists the proton densities of some relevant moderator materials.

Table 3.1. Proton densities in some moderator materials.

Material	Condition	Proton Density, Molecules/cm^3
H_2	22 K, 15 atm	4.4×10^{22}
CH_4	22 K	7.9×10^{22}
NH_3	23 K	9.3×10^{22}
H_2O	300 K	6.7×10^{22}

3.4 Reflectors

The reflector redirects some of the source neutrons that would otherwise miss the moderator back into it and returns those that leak out while slowing down. The purpose of decoupling a reflector from a moderator is to prevent neutrons thermalized in the reflector from entering the moderator and leaking out with long time constants characteristic of the reflector. In a room-temperature reflector, decoupling the two components requires the use of cadmium; this conclusion is based upon the cut-off energy of the transmission cross section and the spectral temperature of the thermalized neutron field within the reflector.

3.4.1 Reference Design

The reference reflector is a D_2O-cooled beryllium structure, inerted with helium and decoupled with cadmium at the appropriate moderators and decoupled from the bulk shielding by Boral.

3.4.2 Other Reflector Materials Considered

3.4.2.1 Cold Beryllium

Although beryllium (mass 9.01) metal is the best reflector known for pulsed source applications and is ubiquitous in present spallation sources operating at room temperature, there is a chance that beryllium cooled to lower temperature (say, 77 K) may provide improved intensity because the long-lived thermal neutron spectrum is depressed to lower energies at the lower temperature than at room temperature. The lower energies of the spectrum, in turn, allow decoupling at lower energies (say, using gadolinium) than is necessary in the room-temperature reflector (decoupling with cadmium or thick boron), resulting in a gain in the low-energy neutron range. The effects are calculable and the cooling system design is straightforward engineering. Beryllium provides a significant neutron multiplication because of Be(n,2n) processes (threshold ~ 2.0 MeV).

Although this option has not yet been exploited in our base design, we have calculated the performance of a variant design in which the beryllium is cooled to 77 K; this design results in a

20% increase in long-wavelength intensity on decoupled moderators and a 50% increase in long-wavelength intensity on coupled moderators.

3.4.2.2 Lead

The advantage of lead, used as a reflector, is that it provides shielding as well as serving as the reflector. The disadvantage of lead is that it produces a long tail on the pulse of neutrons from the moderator, because of the long slowing-down time in the (mass-207.2) material. The tail represents a background for important classes of neutron-scattering measurements. This tail may be tolerable for coupled moderators. Lead also provides a small neutron multiplication because of Pb(n,2n) processes (threshold ~10.0 MeV). On the other hand, lead has a rather low melting temperature and a tendency to creep under load.

3.4.2.3 Heavy Water

The use of D_2O (deuteron mass number D = 2.01) as a reflector is almost as good as beryllium metal because of its low mass and in spite of its lower atomic density and scattering cross section. Moreover, it is easy to remove the heat deposited by nuclear processes, and it has no cracks or voids. However, D_2O has little shielding value although it provides a significant neutron multiplication because of D(n,2n) processes (threshold ~ 2.5 MeV).

3.4.2.4 Metal Deuterides

Certain metal hydrides have, theoretically, substantially higher hydrogen densities than water. As deuterides, the practical deuterium density may exceed that in D_2O, in which case the metal deuteride would present advantages both in slowing-down power and in shielding, because of the metal matrix.

Initial studies have shown no significant advantage for the metal deuterides.

3.5 Neutron Beamlines

3.5.1 Neutron Beam Transport

Figure 3.6 shows the shielding and beam transport arrangements at a larger scale than the preceding figures.

At the bottom of Fig. 3.6 are the two curved-guide clusters, which emerge into a shielded bunker. Their lines-of-sight end within the bunker. At the top of Fig. 3.6, guides extend through movable gates to the shielded compact beam benders, where the lines-of-sight end, and then through guides to neutron beam instrumentation.

Some Guide Formulas

Guide Tube Gain

Straight Guide

The guide tube gain for a fully and uniformly illuminated, straight one-dimensional guide is

$$G = \begin{cases} 1 + (\theta_c / \psi_o)^2 ; & \theta_c \le \psi_o \\ 2\theta_c / \psi_o ; & \theta_c \ge \psi_o \end{cases}$$

where θ_c is the critical angle, $\theta_c = \gamma_c \lambda$, and $\psi_0 = H/L$. H is the width of the guide and L is the length of the guide. $\gamma_c = m\ \gamma_c^{Ni}$, where the factor m relates the critical angle for the guide material to that for natural nickel, γ_c^{Ni} = 0.0017 radians/Å.

Curved Guide

For a fully, uniformly-illuminated, one-dimensional curved guide, the gain is that calculated for a straight guide multiplied by the factor T

$$T = \begin{cases} \frac{2}{3} K^2 ; & K \le 1 \\ \frac{2}{3} K^2 [1 - (1 - 1/K^2)^{3/2}] ; & K \ge 1 \end{cases}$$

where $\lambda^* = (1/\gamma_c)\sqrt{2H/R}$. Here, λ^* is the characteristic wavelength for the guide, R is the radius of curvature of the guide, and $K = \lambda/\lambda^*$.

Line-of-Sight Distance

The line-of-sight distance through a curved guide is $L_{sight} = \sqrt{8HR}$ as the figure illustrates. The (shielded) length of a guide required to provide background reduction may be substantially greater (typically, ~10-20%) than the line-of-sight distance. In the instance of a **compact bender** (a stack of curved guides with many channels) the length required for background suppression must exceed the line-of-sight calculated for the **outside dimension** of the stack, not for a single channel.

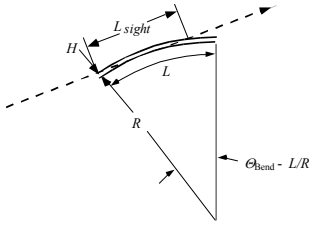

Partially Illuminated Guide

It is usually impractical that the entrance to a guide be adjacent to the source, but rather the guide must begin some distance away. Then there may be no source to illuminate some paths that the guide might otherwise transmit. This is the partially illuminated case that we treat here. Defining

$\psi_o = H / L$, as above,
$\psi^* = (H^* - H) / 2L^*$,
$\psi_M = (H^* + H) / 2L^*$, and
$\psi_s = (H^* + H) / 2(L^* + L)$,

in which H is the width of the guide, H^* is the width of the (symmetrically located) source, L is the length of the guide and L^* is the distance from the source to the entrance of the guide, the gain for a partially-illuminated straight guide is

$$G = \begin{cases} 1 + (\Theta_c / \psi_o)^2 ; & \Theta_c \le \psi_o \\ 2\Theta_c / \psi_o ; & \psi_o \le \Theta_c \le \psi^* \\ (\Theta_c + \psi^*) / \psi_o + & \\ + (\Theta_c - \psi^*)(\psi_M - \Theta_c) / (\psi_o(\psi_M - \psi^*)) ; & \psi^* \le \Theta_c \le \psi_M \\ (\psi_M + \psi^*) / \psi_o ; & \Theta_c \ge \psi_M \end{cases}.$$

This is for the most common case of a long guide, that is, for the situation $0 < \psi_0 < \psi_s < \psi^* < \psi_M$. ($\psi_s$ is irrelevant to the gain factor in this case.) The general result (see reference) includes several more cases.

Reference

J. M. Carpenter and D. F. R. Mildner, "Neutron Guide Tube Gain for a Remote Finite Source," Nucl. Instr. & Meth. 196 (1982) 341-348.

3.5.2 Neutron Guides and Benders

Figures 3.7 and 3.8 illustrate the curved-guide cluster and the compact beam bender concepts.

Measurements at SINQ at Paul Scherrer Institute (PSI) have indicated little transmission of fast and high-energy neutrons past the line-of-sight point (downstream, outside the bunker wall) in this structure. The radius of the bunker is about 25 m, and the guides extend about 5 m into the primary shield. The figure does not show the extensions of the guides into the guide hall. In SINQ (~1-MW proton beam) the guides view the cold source tangentially. Figure 3.8 schematically illustrates a compact beam bender.

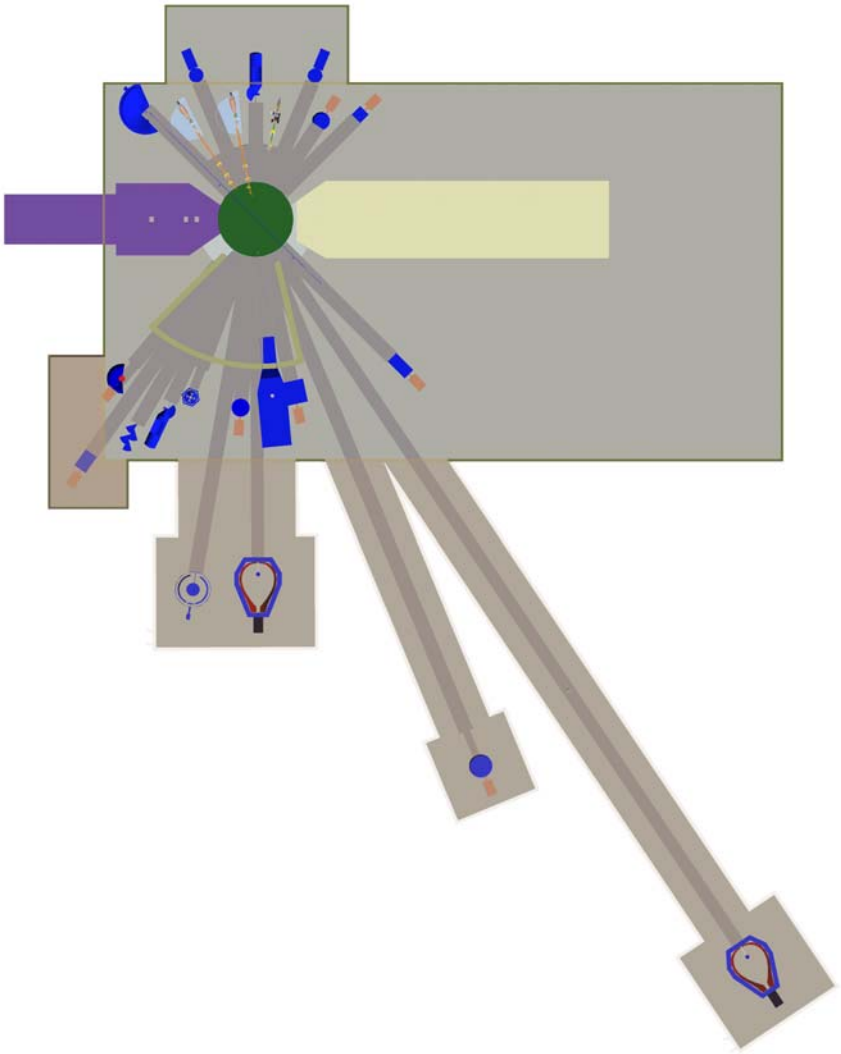

Fig. 3.6. Plan view of the shield and beam transport arrangements in the LWTS (Fig. 2.3 provides the reference set of scattering instruments).

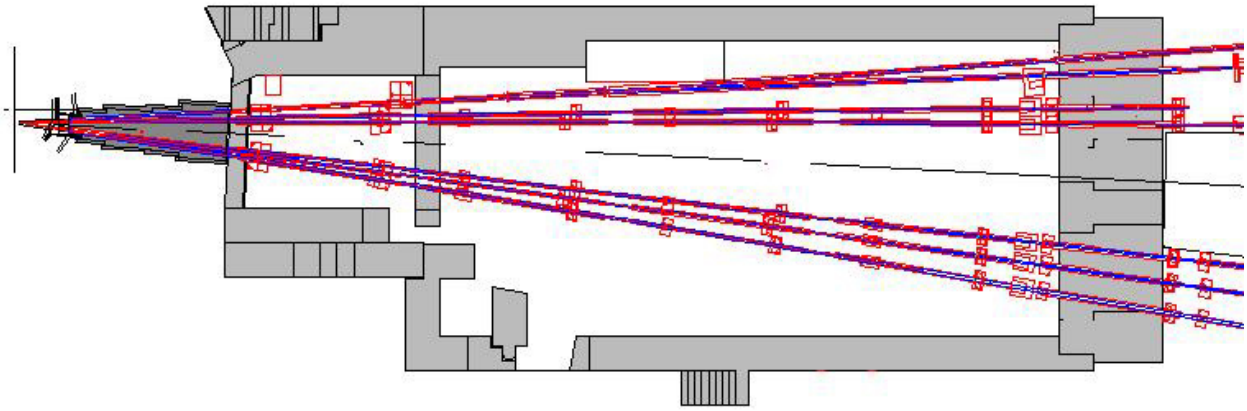

Fig. 3.7. The SINQ curved-guide cluster at PSI and its shielding bunker.

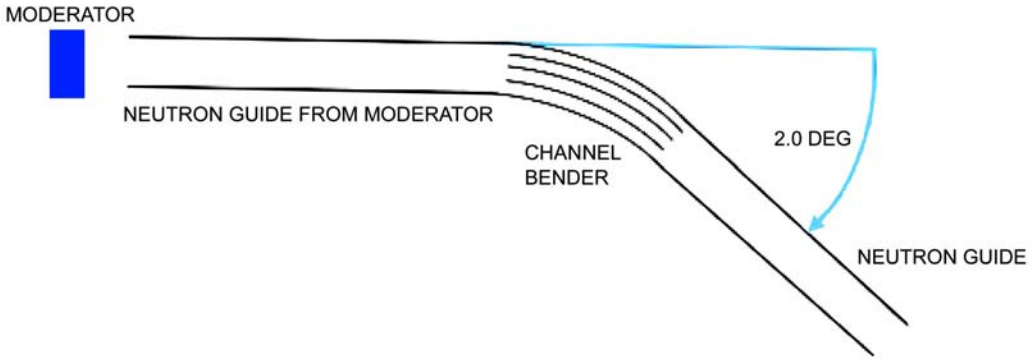

Fig. 3.8. Schematic representation of a compact beam bender. These are essentially stacks of narrow, curved guide channels. In practice, it is possible to efficiently bend a beam of 4-Å neutrons about 2 deg in a length of about 1 m. Standard curved-guide formulas describe their performance.

3.6 Shielding for Neutron Guides and Benders

Shielding issues relating to the fast and high-energy neutron backgrounds caused by the slab moderator configuration and the curved guides and compact beam benders are appropriate subjects for experimental evaluation in the Alternating Gradient Synchrotron (AGS) Spallation Target Experiment (ASTE) testing program at BNL. We will take part in this collaboration, already underway for this and other purposes, which involves several other laboratories committed to high-power spallation neutron source developments in Europe, Japan, and the United States.

3.7 Cooling Systems

3.7.1 Target

The components of the water-based cooling systems, including the D_2O target cooling system, will be sized for more than a tungsten or tantalum target requires to accommodate potential upgrades in the target material, e.g., use of depleted uranium alloys.

The target station will have five independent cooling systems. The target plate cooling system and the reflector cooling systems are heavy-water systems. The target vessel wall cooling system, the combined cooling system, and the moderator/premoderator cooling systems are de-ionized water systems. The combined system cools the biological shield, the target tank, and the proton beamline window. Whenever possible, components will be identical across the various systems to simplify design, procurement, and spare parts inventory.

For reference and general evaluations, the table below lists the shielding mean free paths for high-energy neutrons (E > ~ 200 MeV) and for fast neutrons (~1. < E < ~ 20 MeV).

High-energy neutron mean-free-paths and fast neutron removal mean-free-paths in representative shielding materials.

Material (At Wt.)	Density, gm/cm^3	Number Density, at/cm^3	λ_{HE}, cm	λ_{Fast}, cm
Beryllium (9)	1.85	1.2×10^{23}	50.	8.34
Iron (55.8)	7.8	8.3×10^{22}	17.34	6.25
Copper (63.5)	8.96	8.5×10^{22}	15.8	5.92
Tungsten (183.9)	19.3	6.3×10^{22}	10.1	5.08
Lead (207.2)	11.3	3.3×10^{22}	17.8	9.25
Uranium (238.0)	19.0	4.8×10^{22}	11.1	5.97
Concrete	2.39	NA	46.1	10.4
Chemtree 1-20-26*		NA	32.9	8.7
Water	1.0	6.7×10^{22} [a]	90.25	9.62
Earth	1.6	NA	ca. 85.	
Superdense iron-concrete **	5.5	NA	24.1	7.6

* A proprietary formable iron mortar
** Recent entry not in original table; 55 vol% Iron, 45 vol% concrete
[a] protons/cm^3

Reference: M. Barbier, "Shielding and Activation Study for the Intense Pulsed Neutron Source at Argonne National Laboratory," MITRE Corporation report MTR-6998. September 1995.

3.7.2 Liquid Drain and Retention Tank System

Included in the design of the target cooling systems is a suspect liquid waste retention system. This collection system serves as a radioactive containment and ensures that no release to the environment or unwanted contamination of facilities and personnel will occur in the event of component failure.

All piping and components are welded whenever possible, with the exception of some flanged fittings to allow component removal for maintenance. Piping runs are housed in metal troughs to capture any leakage and, by gravity drain, direct the waste to the suspect liquid retention tank.

3.8 References

3.1.1 SNS-TSR-182-rev. 1, March 28, 2001.

3.1.2 IPNS Upgrade: A Feasibility Study. Argonne National Laboratory Report ANL-95/13 (April 1995).

3.3.1 J.M. Carpenter and E.B. Iverson, Eds., *Proc. Int. Workshop on Cold Moderators for Pulsed Neutron Sources*, Sep. 29–Oct. 2, 1997, Argonne National Laboratory, a brochure of the Megascience Forum of the Organization for Economic Cooperation and Development, Publication Service, OECD, 2 rue André Pascal, 75775 Paris, Cedex 16, France (1998).

3.3.2 M.G. Zemlyanov, "Propane Cold Neutron Source: Creation and Operation Experience," *Proc. Int. Workshop on Cold Moderators for Pulsed Neutron Sources* [1], p. 87–96.

3.3.3 J.M. Carpenter, "Thermally-Activated Release of Stored Chemical Energy in Cryogenic Media," *Nature Magazine* **330**, 358–360 (1987).

3.3.4 A.A. Beliakov, I.T. Tretiakov, E.P. Shabalin, V.V. Golikov, and V.I. Luschikov, "Solid Methane Moderator for the IBR-2 Reactor," *Proc. Int. Workshop on Cold Moderators for Pulsed Neutron Sources* [1], p. 73–78.

3.3.5 R.W.G. Wykoff, "Crystal Structures," 2nd ed., Vol. 2, p. 117, John Wiley & Sons, Inc. (1964).

4. PROPOSED INSTRUMENTS

The technical concept for the LWTS described in Section 2 provides for up to 21 independent neutron beams: 9 viewing the coupled slab moderator, 10 viewing the decoupled slab moderator, and 3 viewing the front wing-like moderator. In this section, we describe 11 instruments that capitalize on the unique capabilities of the LWTS. These instruments emerged from discussions of scientific needs and opportunities summarized in Section 8. Table 4.1 lists their key parameters. We have studied four instrument concepts in greater detail than the others, carrying out simulations to confirm performance projections: the broad-range intense multipurpose small-angle neutron scattering (BRIMS SANS), the 200-neV crystal analyzer spectrometer, the magnetism and diffuse scattering spectrometer (MiDaS), and the high-resolution powder diffractometer. The remaining instrument concept descriptions are less detailed but are sufficient to allow performance comparisons with existing instrumentation and proof-of-principle tests and to provide meaningful guidance for facility design.

Table 4.1. Parameters for proposed instruments.

	Moderator		L1 (m)	L2 (m)	Wavelengths used (Å)	Range	Incident Beam Optics
Broad-range intense multipurpose SANS	Coupled	S-CH_4	27	4–8	1–14.5 1–12.7	0.0025–0.7 $Å^{-1}$ 0.0020–0.4 $Å^{-1}$	supermirror bender
200-neV crystal analyzer spectrometer	Decoupled	S-CH_4	63.4	2	Variable 6.22 Å band	0.05–1.2 $Å^{-1}$ ±420 µeV	curved guide funnel, chopper
Magnetism diffractometer	Decoupled	S-CH_4	32	1	1–13	d = 0.5–23 Å $\Delta d/d$ 2×10^{-3} (1Å)	natural nickel guide, polarizer, choppers
Broad-band reflectometer	Coupled	S-CH_4	18	2	1–20	$Q_{max} \geq 0.3$ $R_{min} \leq 10^{-6}$	supermirror bender
Grazing incidence SANS reflectometer	Coupled	S-CH_4	18	1–3	1–20	0.0008–0.5 $Å^{-1}$	supermirror bender
Neutron spin echo spectrometer	Coupled	S-CH_4	17	22	7–22	0.03–200 nsec	supermirror bender, polarizer, choppers
Polarized neutron reflectometer	Coupled	S-CH_4	18	2	1–20	0–60°	supermirror bender, polarizer
Ultra-cold neutron station	Coupled	S-CH_4	18	varies	1–20 especially 9	varies	supermirror bender, choppers
Direct-geometry spectrometer	Decoupled	S-CH_4	25	5	1–13	E_{max} 200 meV ΔE 2–1000 µeV	curved guide choppers
High-resolution powder diffractometer	Decoupled	S-CH_4	120	4–7	0.5–6.5 (5 Hz)	d = 0.4–3.1 Å ?d/d 3×10^{-4} (1Å)	ballistic guide choppers
Protein diffractometer	Decoupled	S-CH_4	32	0.5	1–13	d = 1.5–10 Å $\Delta d/d$ 4×10^{-3} (90°)	supermirror bender

We have selected the instruments proposed for the LWTS because they provide unique new capabilities for the scientific community and because they exploit the large bandwidth and high cold-neutron brightness provided by the LWTS — features not available at other neutron sources. All these concepts are based on existing technology and could be built immediately.

This suite of instruments supplements the range and performance of existing instruments and instruments proposed for other neutron sources, complements those of the HPTS, and permits rapid, broad-band measurements on evolving sample systems. They will help to close the gap between energy energy/time and wave vector/length scales measurable on existing neutron spectrometers and those currently observable by other methods and, consequently, allow entirely new classes of experiments.

The instrument design concepts are the joint work of those who prepared the science case and experienced instrument scientists from Argonne's IPNS. We are continuing to optimize these designs and expect to discover numerous opportunities for improvements in performance, some of which depend upon the success of modest developments of new components and techniques. We emphasize that the performance of instruments so far evaluated represents a lower limit on what can be achieved.

4.1 Broad-Range Intense Multipurpose SANS

4.1.1 Requirements of the Science Community

Small-angle neutron scattering has extensive uses for characterizing materials in such fields as polymers, biology, ceramics, metallurgy, porous materials, and magnetism. SANS has high sensitivity in the size range of 1 to 100 nm and enables probing complex hierarchical structures that have several distinct length scales. Small-angle x-ray scattering has high sensitivity in the same length scale, but the differing scattering cross sections for neutrons offer unique advantages for the study of multicomponent systems and magnetic materials. Hydrogen/deuterium substitution is notably powerful in studying polymers and biological materials.

The broad SANS community needs an instrument that combines the best features of the reactor-based and time-of-flight (TOF) SANS instruments and that is at the same time capable of measuring data in a Q-range of 0.001–0.7 Å in a single, fast measurement. With such an instrument, scientists will be able to carry out new kinds of studies such as pressure-dependent protein folding kinetics [4.1.1] and temperature-dependent phase separation and crystallization kinetics in polymers and metallic alloys.

4.1.2 Instrument Design and Advantages

We have designed a versatile, high-throughput TOF SANS instrument, BRIMS SANS for the proposed LWTS. BRIMS can cover a Q-range of 0.002–0.4 Å in a single measurement. Options will be available to extend the Q-ranges on both ends by selecting collimation options and beam-stop size as well as the position of the area detector. We set the maximum length of the instrument at 31 m with the sample at 23 m and the entrance aperture at 15 m from the source. We are optimizing BRIMS to take advantage of the 10-Hz source frequency (offering broad wavelength bandwidth) and of the cold-neutron spectrum from a tall, coupled, solid methane moderator. Frame definition choppers or mirror filters eliminate neutrons with wavelengths greater than 15 Å, the maximum wavelength enabled by the 10-Hz pulsing frequency. BRIMS employs a movable, 100 × 100-cm^2 position-sensitive area detector with small pixels and a high data rate. The detector can be either 27 m (λ_{max} = 14.6 Å) or 31 m (λ_{max} = 12.75 Å) from the

source, providing for different compromises in flux, Q-range, and Q-resolution, depending on the experiment. For example, the longer sample-to-detector distance gives slightly higher resolution and higher density of Q points, while shorter sample-to-detector distances allow higher flux on samples and a broader Q-range. Offsetting the detector horizontally will increase Q_{max} and improve the resolution and statistical quality of the data at middle- and high-Q regions. The Q_{min} and Q_{max} in this instrument are

$Q_{min} = 4\pi \sin \theta_{min}/\lambda_{max}$ and

$Q_{max} = 4\pi \sin \theta_{max}/\lambda_{min}$. [4.1]

The available bandwidth ($\Delta\lambda$) or the maximum wavelength (λ_{max}) useful in a given frame can be calculated using the following:

$\Delta\lambda = \lambda_{max} = 3955.$Å-m/sec/fL [4.2]

where f is the repetition rate and L is the length of the instrument. A bank of detectors at high scattering angles, for which there is already precedent, can extend the Q_{max} and increase the counting rate at the larger Qs, but we have not yet included one in our proposed concept.

One essential consideration in this design is to separate the neutrons useful for SANS (λ = 1–15 Å) efficiently from the high-energy and γ-ray components of the direct beam to reduce the background. The prompt neutron spectrum from the target and moderator system contains large numbers of fast and high-energy neutrons and γ-rays that must be prevented from entering the collimation system. Currently, four different techniques are in use at different pulsed neutron sources to reduce or eliminate the fast neutrons. The SANS instrument at the KENS pulsed source at the High Energy Accelerator Research Organization (KEK) in Japan uses a long curved neutron guide to bring the detector out of sight of the source [4.1.2]. The low-Q (LOQ) instrument at ISIS [4.1.3] employs a beam bender (an array of short, narrow curved guides placed side by side) for this purpose. The two SANS instruments at IPNS employ cold MgO filters [4.1.4-4.1.6], and the low-Q diffractometer (LQD) instrument at the Manuel Lujan Neutron Scattering Center (MLNSC) at Los Alamos National Laboratory (LANL) [4.1.7] uses a T_0 chopper to attenuate the fast neutrons.

In the conceptual BRIMS, a guide and bender assembly separates the cold neutrons from the direct fast neutron and γ ray beam so that the area detector is completely out of the line of sight of the source. To improve the flux at short wavelengths, we have assumed the use of high-index supermirrors. The input snout guide from the source leads to a 2-m-long, 44.625-mm-wide bender consisting of several 15-cm-tall vertical blades. Each consists of a 0.2-mm SiO_2 substrate with 3.5-μm-thick, m = 3.5 supermirror on the reflecting side, a proven technology. The width (w) of each guide channel is as follows:

$$W = \frac{l}{2\theta_B} (m\lambda_C\gamma_{Ni})^2 \qquad [4.3]$$

where λ_C is the critical wavelength (we design for λ_C = 1 Å), l = 2 m (the length of the channel), θ_B is its bend angle, and γ_{Ni} = 1.7 mrad/Å determines the critical angle of the coating. Thus, the number of blades depends on the required bend angle. For example, a 2-m-long, 11.95-mR bender has 15 channels while a 40-mR bender has 50 channels.

Recipes for Instrument Shielding Materials

Here we provide recipes for several types of shielding materials that we manufacture locally and use successfully for various purposes in IPNS instruments.

"Caramel Corn"

Typical Purposes: Bulk shielding around instruments and detectors.
Composition (for blocks 8 x 12 x 12 in^3 ~20 x 30 x 30 cm^3):

Ingredient	Weight, kg	wt. %
Epoxy 828	3.93	22.7
Epoxy 3030	2.73	15.8
Polyethylene beads	8.45	48.9
Borax	2.18	12.6
Total	17.3	

Note: Proportions of liquid and solid adjusted to fill container uniformly.

"Crispy Mix"

Typical Purposes: High-density Boron, Low-albedo shielding; detector backing, flight path liners, collimators; sheets and shapes.
Composition (for sheet ~1 x 30 x 30 cm^3):

Ingredient	Weight, gm	wt. %
Epoxy 828	100.	6.2
Epoxy 3030	70.	4.3
B_4C	1440.	89.4
Total	1610.	

Note: The less epoxy (pre-mixed), the better. Mix thoroughly, be patient, have faith, pack carefully into mold corners. Top ("up" side) is dryer (lower albedo) than bottom.

Lead-borated-epoxy Bricks

Typical Purposes: High density shielding around choppers, collimators, fast-neutron hot spots. Composition (for 10 bricks 2 x 4 x 8 in^3 ~ 5 x 10 x 20 cm^3):

Ingredient	Weight, kg	wt. %
Epoxy 828	3.05.	4.1
Epoxy 3030	2.05	2.8
Borax	0.57	0.8
Lead shot	68.2	92.3
Total	73.8.	

Note: Proportions of liquid and solid adjusted to fill container uniformly.

Materials:
Epoxy (Shell), cured density ~ 1.20 gm/ cm^3
Lead shot ~ 1.-mm dia. spheres
B_4C ~ 0.5-mm grit; US standard sieve grades 14 to 36
Borax (anhydrous) technical fine grade $Na_2B_4O_7$
Polyethylene (low-density) mold stock, beads ~ 5. mm dia x 2.5 mm thick, density ~ 0.92 gm/ cm^3

Eliminating radiological and detector background problems caused by high-energy neutrons in the beam requires heavy shielding material along the line of sight through the bender and collimator system. A straight section of guide and shielding after the bender gives this protection. This configuration separates the direct beam from the beam incident on the sample, with the heavy shielding ending 2 m upstream from the sample position.

We evaluated the instrument using acceptance diagrams and the Los Alamos Neutron Instrument Simulation Program (NISP) Monte Carlo simulation package. The basis of performance calculations is the flat coupled solid methane moderator of LWTS (see Sec. 7.0), viewed perpendicularly. BRIMS (Fig. 4.1) combines features from the best steady-state and pulsed-source SANS instruments. Table 4.2 lists key design parameters for the instrument. By using Monte Carlo simulations with the scattering kernels for spherical particle and delta function scatterers, we characterized the effects of various collimation choices on count rate, Q-resolution, and Q_{min}, as described in Table 4.3.

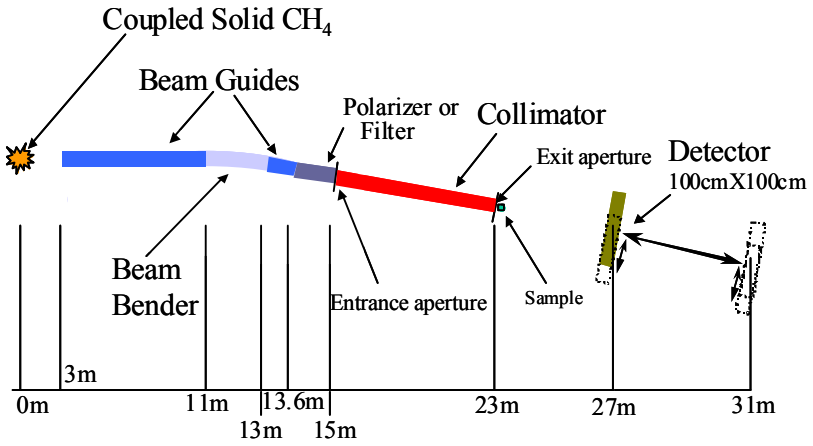

Fig. 4.1. Schematic of the BRIMS instrument proposed for the LWTS at SNS.

Table 4.2. Instrument design parameters for the BRIMS.

Component	Description
Moderator	Coupled solid CH_4 slab
Beam size at moderator	12 cm (width) × 20 cm (height)
Source-to-beam bender	11.0 m
Bender length, supermirror index	2.0 m, 3.5 times that of Ni
Source-to-entrance aperture distance	15.0 m
Source-to-sample distance	23.0 m
Sample-to-area detector distance	4.0 to 8.0 m (variable)
Area detector active area	100 × 100 cm^2
Pixel resolution	3 to 5 mm (fwhm)

Using neutrons with λ ranging from 1–14.5 Å in a TOF mode, BRIMS will produce higher count rates than any instrument currently existing anywhere in the world and will do so in a single measurement. Figure 4.2 compares Monte Carlo simulations and analytical calculations for BRIMS (in its high-throughput configurations) with the current world's best SANS instrument, D22 at ILL. Simulations assume a 2-cm sample diameter for the ILL-D22, but a 1.5-cm sample diameter for BRIMS. BRIMS's counting rate excels for each Q value in the typical SANS Q-range of 0.0025–0.7 Å, while retaining comparable resolution. Moreover, D22 requires three settings to cover a Q range of 0.002–0.5 Å.

Table 4.3. Some instrument settings for BRIMS. (Parameters in bold and regular text correspond to 4 m and 8 m sample-to-detector distances, respectively. The configurations marked with an (*) were extensively modeled using NISP).

Entrance Aperture Diameter (cm)	Sample Aperture Diameter (cm)	Beam Stop Diameter (cm)	Entrance Aperture to Sample Aperture (m)	Sample-to-Detector Distance (m)	Relative Intensity from Acceptance Diagrams	λ_{max} (Å)	Q_{min} (Å^{-1})	Q_{max} with 1-Å Neutrons (Å^{-1})
4*	1.33	4	8	4	1.00	14.5	0.00217	0.785
3*	1.5	6	8	8	0.72	12.75	0.00185	0.393
3	1	3	8	4	0.32	14.5	0.00163	0.785
2*	1	4	4	4	0.57	14.5	0.00217	0.785
2	1	4	8	8	0.141	12.75	0.00123	0.393
2	0.67	2	8	4	0.063	14.5	0.00108	0.785
1.35	0.67	2.67	8	8	0.029	12.75	0.00082	0.393
1.35*	0.45	1.35	8	4	0.0130	14.5	0.00073	0.785
0.9	0.45	2	8	8	0.0058	12.75	0.00062	0.393

The best cold-source reactor-based SANS instruments currently have an advantage over those at present-day pulsed sources in terms of both flux and resolution for $Q < 0.002$ Å^{-1}. However, as the figure shows, the use of multiple converging aperture collimation on the BRIMS substantially reduces this advantage. Simulations of the multiple aperture geometry and experimental tests of the feasibility of constructing such a device are underway, as are evaluations of further refinements of the design.

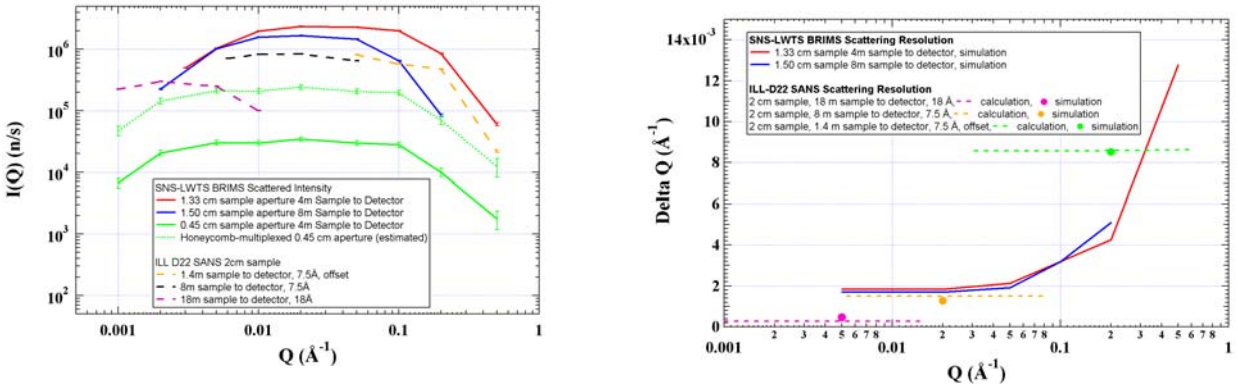

Fig. 4.2. Comparison of count rates and resolution at BRIMS and D22 using the results of Monte Carlo simulations and analytical calculations.

4.2 Crystal Analyzer Spectrometer

4.2.1 Requirements of the Science Community

Studies of chemical and biomolecular dynamics often require systematic investigation of many similar molecules under slightly different conditions, demanding a large range of energy transfers and energy transfer resolutions for optimum study. There is a gap between the resolution accessed by neutron spin echo (NSE) techniques (in the time domain) and that accomplished in existing high-resolution direct- and inverse-geometry spectrometers. Filling this niche in energy resolution will allow systematic studies over the large ranges of energy transfer required by many disciplines.

4.2.2 Instrument Design Advantages

The proposed 200-neV crystal analyzer spectrometer (CAS), using the mica (002) (d=10…Å) reflection, offers a remarkable Q-range — 0.05 $Å^{-1} \leq Q \leq 0.6$ $Å^{-1}$ — with a high Q-resolution (0.002 $Å^{-1} < \delta Q < 0.015$ $Å^{-1}$) and excellent energy transfer range (- 60 μeV < ω < 60 μeV). The resolution of this spectrometer, 200 neV, lies well below that achieved in existing instruments of the same type, including the design goal of the HPTS backscattering spectrometer. The initiative for the inverse geometry spectrometer came about with the plans to build the LWTS [1.1], which will provide a high flux of long-wavelength neutrons and a long interval between pulses. The instrument design employs mica analyzers close to backscattering geometry (scattered-neutron wavelength of 20 Å) to provide extremely high-energy transfer resolution [δω ≤ 0.2 μeV full-width half-maximum (FWHM) elastic]. We used the Monte Carlo simulation program McStas [4.2.1], developed at Risø National Laboratory, to optimize the layout of individual components and to estimate the instrument performance. Figure 4.3 shows the scattering chamber of the CAS.

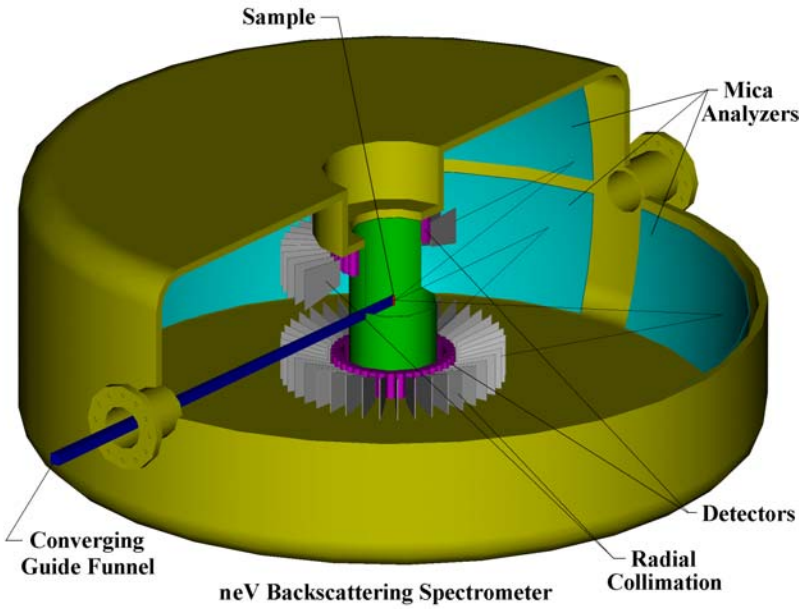

Fig. 4.3. The scattering chamber and the CAS guide system at the LWTS.

We adopt the simple, traditional formalism to guide our initial analysis and choices of parameters; that formalism is the basis for the following discussion. Consider that the uncertainty in the energy transfer for a CAS can be separated into a term dependent on the primary spectrometer ($\delta\omega_P$, components before the sample) and on a term dependent on the secondary spectrometer ($\delta\omega_S$, components after and including the sample). If, as is traditional, we assume that the terms are independent and that the uncertainties add in quadrature, the energy transfer resolution is [4.2.2],

$$\delta\omega = \sqrt{\delta\omega_P^2 + \delta\omega_S^2} \quad , \qquad [4.4]$$

where

$$\delta\omega_{\mathrm{P}} = 2E_i \left(\left(\frac{\delta L_i}{L_i} \right)^2 + \left(\frac{\delta t_0}{t_i} \right)^2 \right)^{\frac{1}{2}}, \qquad [4.5]$$

and

$$\delta\omega_S = 2\left(E_i^2 \left(\frac{\delta t_f}{t_i} \right)^2 + E_f^2 \left[\left(\cot(\theta_B)\delta\theta_B \right)^2 + \left(\frac{\delta d}{d} \right)^2 \right] \right)^{\frac{1}{2}}, \qquad [4.6]$$

where E_i is the incident neutron energy, L_i is the moderator-sample distance, t_i is the incident neutron flight time, t_0 is the emission time of the neutron from the moderator, and t_f is the time for the scattered neutron of selected final energy to travel from the sample to the analyzer to the detector.

In a CAS, the final neutron wavelength, λ_f, is fixed by Bragg reflection from the analyzer crystals, $\lambda_f = 2d\sin\Theta_{\mathrm{B}}$, and $E_f = h^2/2m\,\lambda_f^2$. We assume that the first term in Eq. 4.5 is small compared to the second and, therefore, that the contribution from the primary spectrometer to the resolution arises from the moderator pulse width (δt_0). On the other hand, the contribution from the secondary spectrometer (Eq. 4.6) represents uncertainty in the lattice parameter (δd) of the crystal analyzers and the uncertainty of the Bragg angle $\delta\theta_B$, which has contributions both from the analyzer crystal mosaic and the sample dimensions.

The decoupled poisoned solid methane moderator at LWTS generates a pulse with a width of 90 μsec for λ = 20 Å, corresponding to elastic scattering of a scattered neutron wavelength of λ_f = 20 Å (E_f = 0.2045 meV) reflected from the (002) planes of mica. To achieve the timing resolution necessary for the desired $\delta\omega$ requires that the spectrometer have a long primary flight path. An initial flight path around 63 m long from moderator to sample provides the desired primary-flight-path resolution.

According to the traditional analysis and for practical reasons, the analyzers should be slightly off the backscattering orientation. We find that this component of the resolution, $\cot(\theta_B)\delta\theta_B$, can be relaxed from exact backscattering (θ_B = 180°, cot θ_B = 0) without increasing the overall resolution significantly [4.2.3]. A sample/detector geometry with a Bragg angle of 87.5˚ is a reasonable choice. In contrast to spectrometers such as the ISIS spectrometer IRIS that have less stringent resolution requirements, the sample size in our CAS can easily dominate the first and second terms in Eq. 4.6. Restricting the sample size is not an issue in cases where only limited amounts of sample are available. However, when sufficient sample is available, a restricted beam size lowers the counting rate in the detector. Optimization of the secondary spectrometer requires keeping the first term of Eq. 4.6 small compared to the second. Constraining the design to a 2-m sample-analyzer flight path leads to an optimized sample size of 2 × 2 cm^2 and a contribution of 0.41˚ to $\delta\theta_B$ due to sample size. The total contribution of the sample size to Eq. 4.6 is then 163 neV (to be added in quadrature to the $\delta\theta_B$ contribution from the analyzer mosaic). At this stage, we ignore resolution contributions associated with the detector and those caused by zigzag paths [reference] in the guide.

It is also important to understand the contributions to the Q-resolution for energy transfers near the elastic peak. In this case, the momentum transfer is

$$Q = \frac{4\pi sin\left(\varphi / 2\right)}{\lambda_f} \qquad [4.7]$$

where ϕ is the angle between the incident neutron beam and the scattered beam directions. Differentiating Eq. 4.6 and considering that the uncertainty in λ_f is small, the uncertainty in Q is

$$\delta Q = \frac{4\pi cos\left(\varphi / 2\right)}{\lambda_f} \frac{\delta\varphi}{2} . \qquad [4.8]$$

The contributions to $\delta\phi$ are the incident beam divergence ($\delta\phi_i$), the divergence due to sample size $\delta\phi_S$, and the angular acceptance of the analyzer ($\delta\phi_A$).

We carried out a preliminary guide optimization by iterating a Monte Carlo simulation. We selected a curved guide 30 m in length with a radius of curvature of 1 km, giving a characteristic wavelength of 7.9 Å when the critical angle is equal to that of natural nickel. The guide begins at 8.34 m from the moderator, accepting 20-Å neutrons with 0.5˚ divergence. The straight guide extends a total of 18.77 m and terminates in a 6-m-long natural-nickel funnel with an exit cross section of 2 × 2 cm that ends 25 cm from the sample position. The total initial flight path length is thus 63.36 m. The estimated total guide gain (ratio of neutrons on the sample with and without a guide) is 360 for 20-Å neutrons. The spectrometer tank is a 4-m-dia vacuum vessel. Table 4.4 describes the guide components. Figure 4.3 illustrates the scattering chamber design.

Table 4.4. Instrument design parameters for the CAS.

Component	Description
Moderator	Decoupled solid CH_4 slab (30 mm poisoned); δt_0 = 90 μsec for λ = 20 Å
Source-to-sample distance	63.36 m
Source-to-start of guide distance	8.34 m
Curved guide length	30 m
Straight guide length	18.77 m
Guide funnel length	6 m (natural Ni)
End of funnel– to-sample distance	0.25 m
Sample– to-analyzer distance	2 m
Guide	20 cm (H) × 15 cm (V) guide/funnel
Analyzer crystal	mica (002), Bragg angle = 87.5°
Sample	2 × 2 cm^2 cross section (geometry varied)

The time required to obtain a desired number of counts (P_T) in the peak channel is

$$t = P_T \times \frac{1}{F_D} \times N_Q \times \frac{N_R}{2}, \qquad [4.9]$$

where F_D is the counting rate per Q-point and per energy transfer bin; N_Q is the total number of single Q-points summed into the detector (equal to 10 in this case); and N_R is the number of bins across the elastic peak into which counts are stored, with a typical value of 20. The factor 2 corrects for the approximately triangular shape of the resolution function. For this example, for a 10% scattering sample, the time required to obtain 4,000 counts in the peak time channel is approximately 15 min.

We conducted a similar analysis to measure the performance of this instrument if positioned at the HPTS. The results show a decrease of a factor of 4 in flux on samples at the HPTS. Moreover, pulse-suppression choppers, required on HPTS to eliminate intervening pulses, would cause uncertainty in background.

A disk chopper located directly outside the bulk shielding eliminates frame overlap at the sample position. The bandwidth chopper gives a wavelength band of 6.219 Å delivered to the sample. This band provides a range of energy transfers for the mica (002) reflection of ± 60 μeV. Table 4.5 shows the performance of the instrument for near-elastic scattering.

Table 4.5. Spectrometer performance for near-elastic scattering.

Analyzer Crystal	λ_f (Å)	$\Delta\lambda$(Å)	ω-range (μeV)	$\delta\omega$ (FWHM) (μeV)	Q-range (Å^{-1})	δQ (FWHM) (Å^{-1})
Mica (002)	20	6.219	-60–60	0.215	0.05–0.6	0.015–0.002
Mica (004)	10	6.219	-420–420	1.14	0.1–1.2	0.03–0.004

These simulations assume that the analyzer crystals are made of micas, alumino-silicate minerals with a sheet structure that has two layers of silicate tetrahedra arranged between a layer of hydrated metal-oxide octahedra. They exist in different species such as muscovite, annite, phlogopite, fluoro-phlogopite, and biotite. Slabs of single-crystalline mica are of interest as cold-neutron monochromators or analyzers in high-resolution spectrometers because of their large lattice spacing (about 20 Å). Recent investigations [4.2.4] of synthetic fluorinated mica, fluoro-phlogopite $K_2Mg_6(AlSi_3O_{10})_2F_4$, show strong (002 and 006) reflections and a weak (004) reflection with very low thermal diffuse scattering. In natural phlogopite, $K_2Mg_6(AlSi_3O_{10})_2(OH)_4$, all reflections are consistently strong but have higher diffuse backgrounds. Fluorinated mica has unique characteristics: high chemical stability, excellent reflectivity, freedom from outgassing at high temperature in vacuum, excellent electrical insulation, high heat tolerance (up to 1100° C), nonradioactive background, and high flexibility and cleavability, which are much superior to those of natural micas. Furthermore, fluorinated mica is hydrogen-free, which helps reduce incoherently scattered neutron background. Large fluorinated mica crystals of high quality can be grown by a Bridgeman-Stockbarger method [4.2.5]. Given these advantages it is reasonable to consider fluoro-phlogopite as an option, despite its higher price than natural materials. However, optimization of the crystal analyzers is crucial to the operation of the spectrometer. Parameters such as neutron reflecting properties [4.2.6] and ideal crystal thickness, mosaic width, and relative plane spacing uncertainty ($\delta d/d$) have not yet been fully explored.

Possible improvements to the current design could include changing the moderator poison depth to a shallower position. This choice would improve the resolution but cause a loss of flux on sample. Moderator studies reveal that as poison depth varies, the time average flux varies approximately as the inverse square of the pulse width at each wavelength. The instrument design is also constrained by the initial flight path length. Because of the high transmission of the natural Ni guide, this distance can be increased without significantly changing the instantaneous flux on sample. The sole effect of increasing the length of the flight path would be to decrease the range of energy transfers accessible in a single-frame measurement. This increased length option could increase the resolution of the instrument by improving the resolution of the primary spectrometer.

Other optional possibilities include moving the spectrometer to a coupled moderator and using a pulse-shaping chopper to modify the long time tail of the moderator pulse. However, because of the large bandwidth necessary (6.219 Å) for the instrument, this solution may not be viable. Another possibility is to use a Drabkin filter [4.2.7]; the basic idea of this option is to create a resonance condition so that only neutrons with two parameter values (time and wavelength) related in a selected way will be transmitted. Neutrons that do not fulfill the conditions (for example, neutrons from the moderator tail) will not appear in the filtered beam. After transmission through the energy filter, the wavelength-time relation is much sharper than before. The device also will filter out any steady background of delayed neutrons, the small fraction of neutrons that are constantly emitted from the target. The Drabkin filter produces and requires a polarized neutron beam and a consequent loss in the neutron flux on the sample of at least a factor of 2.

Including higher-order reflections in the data analysis to extend the ranges of both energy and momentum transfer would also improve the instrument.

We have envisioned this instrument as a backscattering spectrometer, which is the best-understood version but is still a limiting case of the time-focused crystal-analyzer family of spectrometer instruments. A recently completed, general analysis of CASs will soon appear in the literature [references]. No instrument has yet incorporated the results of that analysis, but we will use the new theory to guide further refinements of the design of the 200-neV CAS proposed here. The opportunities for improvement in the design of this class of spectrometers will surely lead to significant enhancements in its performance.

Issues that require further R&D are characterization of mica and other crystals and detector development.

4.3 Magnetism Diffractometer

4.3.1 Requirements of the Science Community

The working group on magnetism identified spin density measurements and diffuse/critical scattering as areas of neutron research that are currently not served by existing neutron facilities in the United States and are of the highest priority for magnetism research in the future. We propose to construct a magnetism and diffuse-scattering spectrometer, MiDaS at the LWTS to meet these needs.

4.3.2 Instrument Design and Advantages

The MiDaS will have the following characteristics:

- High intensity at long wavelengths for magnetic and diffuse scattering,
- Access to large volumes of reciprocal space to map out diffuse scattering,
- Low angular divergence (0.1°) and *d*-spacing resolution ($\Delta d/d$~0.2%) for distinguishing critical scattering around Bragg reflections as well as for diffuse scattering
- Use of polarized neutrons to resolve magnetic from nuclear scattering and to measure Bragg flipping ratios
- Construction with nonmagnetic materials (aluminum or stainless steel) to facilitate use of high magnetic fields
- Low backgrounds for measuring weak scattering and/or small samples

Table 4.6 lists MiDaS instrument design parameters, and Fig. 4.4 provides a conceptual sketch of the MiDaS instrument.

We have completed a detailed study of the resolution and neutron transport systems. The following paragraphs describe the primary components of the spectrometer and their roles and calculated performance.

Table 4.6. Instrument design parameters for the MiDaS.

Component	Description
Moderator	Decoupled solid CH_4
Source-sample distance	30 m
Flight path	7×7 cm supermirror guide
Resolution	$\Delta d/d \approx 2 \times 10^{-3}$ at d ≈ 1 Å
d-Spacing range	0.5–23 Å
Detector	2-D PSD with 1×1 cm resolution
Polarization	Removable polarization cavities

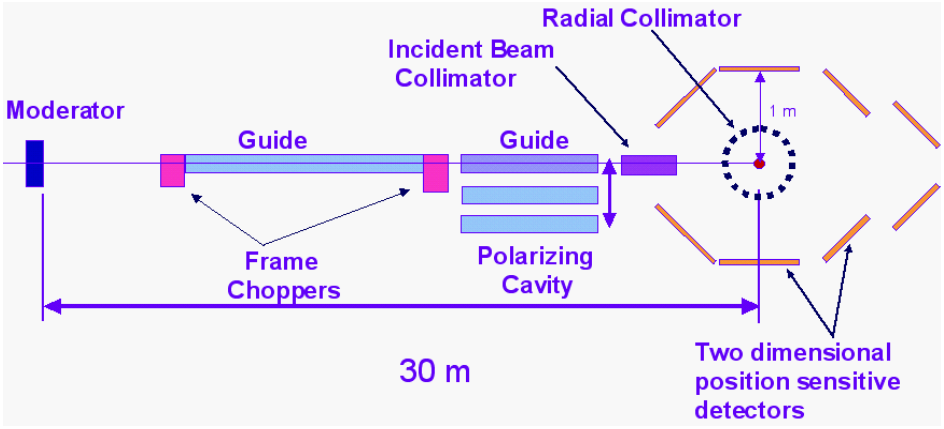

Fig. 4.4. Sketch of the MiDaS at the LWTS.

4.3.2.1 Moderator

The resolution requirements for critical and diffuse scattering and cold neutrons are best met by the decoupled solid methane slab moderator (see Sec. 7). A considerable gain in intensity can be obtained by using a coupled moderator (at the expense of resolution). Scientists have recently proposed using a Drabkin filter [5] to chop the tail of the neutron pulse while maintaining the higher peak flux of this type of moderator; however, the performance of this device for this purpose is still under investigation.

4.3.2.2 Primary and Secondary Flight Paths

The time-resolution performance of a solid methane moderator gives $\Delta d/d$ of ~0.2% at backscattering angles with a primary flight path of 30 m (see Table 4.7). A secondary flight path of 1 m provides a secondary divergence of 0.06° for a 1 × 1 × 1 mm^3 sample, roughly matching the primary divergence.

Table 4.7. Resolution of MiDaS at various scattering angles.

Scattering Angle (°)	Secondary Flight Path (m)	d_{max} (Å)	$\Delta d/d$ (%)
148	1	6.3	0.2
90	1	8.5	0.27
60	1.5	12	0.3
30	2.5	23	0.5

4.3.2.3 Neutron Transport

Monte Carlo simulations show that a straight 7 × 7 cm supermirror guide (with collimation before the sample) provides considerable flux of thermal neutrons for crystallographic investigations. Assuming unpolarized operation using neutrons from the proposed decoupled 20 K solid methane moderator with wavelengths from 0.5 to 12 Å, the flux at the sample position is 2.4 × 10^7 n/s/cm_2 assuming an rms incident beam divergence of 0.06°. For polarized operation using wavelengths from 2 to 10 Å, the flux at the sample position is 6.0 × 10^6 n/s/cm_2 assuming a 90% transmission efficiency for the polarizing optics. Simulations indicate that the divergence

of the beam from a 23-m supermirror guide will be ~0.05° at the sample (see Fig. 4.5). We performed simulations using a straight guide to simplify and improve our understanding of the results; however, it will be necessary to use a curved guide or a T_0 chopper to avoid the intense fast neutron and gamma flash of the slab moderator.

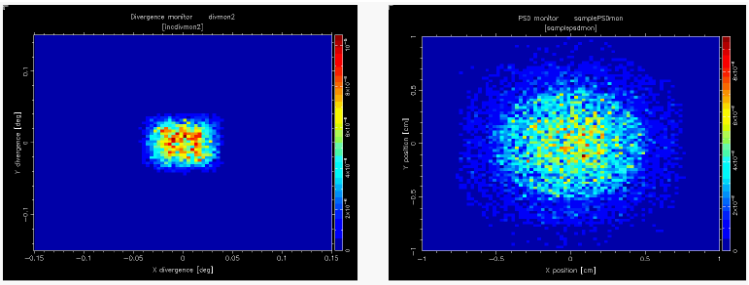

(a) (b)

Fig. 4.5. Maps of (a) horizontal and vertical divergence and (b) beam spatial intensity distribution calculated using Monte Carlo simulation of the MiDaS neutron transport system. The simulation model places a 23-m straight supermirror guide 6 m away from the moderator. In front of the sample is a collimation package reducing the beam cross section from 7 × 7 cm to 0.1 × 0.1 cm over a distance of 0.5 m.

4.3.2.4 Polarized Beam

The Hahn-Meitner Institute (HMI) in Berlin has recently demonstrated solid-state supermirror polarizing cavities [7] that efficiently transmit one spin state over a broad wavelength range (2–10 Å) while rejecting the other. A radio-frequency spin flipper can be used to change the spin state over the same wavelength range. MiDaS employs a similar spin filter/spin flipper assembly that will be interchangeable with a section of normal supermirror guide for use in unpolarized experiments.

4.3.2.5 Choppers

Frame-definition choppers will select an optimum wavelength range for the polarizing cavity or define an optimum wavelength band for unpolarized neutron scattering. It may be necessary to use a T_0 chopper in addition to the frame-definition choppers to control the fast-neutron background.

4.3.2.6 Detector Arrangement

The arrangement of detectors around the sample is still under investigation. On the basis of current experience with TOF spectrometers, we plan to place detectors to cover a large solid angle around the sample. To improve resolution at lower scattering angles, we plan to consider increased secondary-flight-path lengths (see Table 4.7).

4.3.3 Conclusions

MiDaS will take advantage of the peak in brilliance at 4 Å from the solid methane slab moderator at LWTS. If MiDaS were placed at the HPTS, it is possible that it would function

adequately at 20-Hz. However, because the methane moderator at the LWTS provides a gain of 9 on a per-pulse basis over the hydrogen moderators at the HPTS, MiDaS at the LWTS will have an overall intensity advantage of four and a half times compared to 20-Hz operation at the HPTS.

4.4 Ultra-High Resolution Powder Diffractometer

4.4.1 Requirements of the Science Community

Structural complexity, in the form of very large unit cells, phase coexistence, subtle superlattices and distortions, or expanded length scales, is increasingly important in the physical sciences; examples range from proteins, designer porous solids, and self-assembled nanostructures to engineering alloys and cement. Existing synchrotron x-ray diffractometers offer excellent resolution ($\Delta d/d \sim 10^{-4}$) and have expanded our understanding of many important materials such as C_{60} derivatives, high-Tc superconductors, zeolites, and piezoelectrics. Neutron diffractometers with comparable or better resolution and good data rates (as proposed here) will be even better suited to addressing these problems because of their sensitivity to light atoms, different scattering contrast levels, good intensity at high Q, and sensitivity to magnetic ordering.

4.4.2 Instrument Design and Advantages

The ultra-high-resolution powder diffractometer (UHRPD), with an excellent data rate (about five times that of ISIS-HRPD) and resolution matching that of x-ray diffractometers operating at synchrotron sources, will enable qualitatively new capabilities for neutron powder diffraction. Results from the UHRPD will be the basis for properly optimized joint refinements of neutron and highest-resolution x-ray data. Table 4.8 lists the proposed design parameters for UHRPD; Fig. 4.6 shows a schematic illustration of the instrument.

Table 4.8. Instrument design parameters for the UHRPD.

Component	Description
Moderator	Decoupled solid CH_4
Source-sample distance	120 m
Flight path	Ni guide with frame-overlap choppers
Flux at the sample	$\sim 1 \times 10^6$ n cm^{-2} s^{-1}
d-Spacing range	0.4-3.1 Å in the first frame at 5-Hz repetition rate
Resolution	$\Delta d/d \approx 3 \times 10^{-4}$ at d ≈ 1 Å
Detector	4 m for the highest resolution 2-D PSD with 1 × 1 cm resolution; ~5.8 m^2 total area

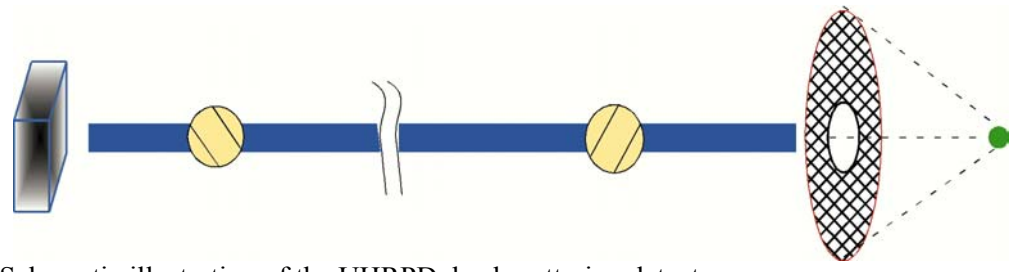

Fig. 4.6. Schematic illustration of the UHRPD, backscattering detector.

The very sharp pulses provided by a decoupled, poisoned solid methane moderator in the under-moderated wavelength regime at the LWTS (see Sec. 6) are the basis for the high-resolution performance of the UHRPD. The UHRPD is located either at the upstream wing moderator (assuming that it is of 20 K solid methane) or at one of the curved guides viewing the solid methane slab moderator. Monte Carlo simulations, based on a simple disk-shaped detector at back-scattering angles, confirm the resolution of the instrument, $\Delta d/d = 3 \times 10^{-4}$ at d = 1 Å, and provide our estimate that ~10 min is sufficient to collect a high-quality data set for a typical 1-cm^3 sample. The resolution degrades slowly at d-spacings larger than 1 Å.

Detailed design optimizes the guide and detector arrangements. While the instrument can operate at 10 Hz, we expect that the broader bandwidth achieved with 5-Hz operation (by eliminating alternate pulses with choppers) is desirable for many experiments. Adjusting the phases of the frame definition choppers makes it possible to move the d-spacing range to larger values to study large-cell structures. The combination of a cold moderator and guide tube provides an excellent neutron flux of long-wavelength neutrons for such applications.

Including detector coverage at smaller angles significantly enhance the performance of this instrument. Experience with simulations of the SNS HPTS powder diffractometer shows that it can also be cost effective to consider partial-arc detector coverage with the horizontal plane scattering optimized for resolution and the vertical plane scattering optimized for flux on sample.

4.5 Broadband Reflectometer

4.5.1 Requirements of the Science Community

Neutron reflectometry is a powerful technique for resolving the structure of materials in thin films and at surfaces and interfaces. Routine uses include studying the adsorption of surfactants, biologically relevant lipids, proteins, and polymers upon substrates of interest and probing the nature of thin polymer films and biological membranes. The knowledge gained from neutron reflectometry underpins improvements in such diverse products as adhesive tape, nonstick surfaces, surgical materials, and drug delivery systems. High-flux broadband neutron-diffraction and reflectometry instruments allow researchers to observe the kinetics of the processes occurring in evolving samples by making several rapid measurements over the timescale of the process. The interesting possible applications of this reflectometry technique include studies of the relaxation of polymers upon melting, the organization or collapse of biological membranes, and real-time growth of layers in an *in situ* sputtering chamber.

4.5.2 Instrument Design and Advantages

Because many of the most interesting applications for broadband reflectometry involve relaxation in liquids, the sample surface of this instrument is horizontal with active vibration isolation of the sample position and a goniometer to allow solid samples to be tilted. While we have not investigated the design of this instrument in detail, we base our considerations on the successful surface profile analysis reflectometer (SPEAR) instrument at the Lujan center at Los Alamos. Table 4.9 shows the preliminary design requirements for this reflectometer. The

instrument uses a compact supermirror bender to suppress the higher gamma-ray and fast-neutron background that results from viewing a slab moderator.

Table 4.9. Instrument design parameters for the BROAD-REF.

Component	Description
Moderator	Coupled solid CH_4 slab
Source-to-sample distance	16 m
Source-to-detector distance	19.5 m
Wavelength range	1–20 Å
Nominal Q range	0.008–0.3 $Å^{-1}$
Nominal range of reflectivity	Better than 10^{-6}
Detector	100 × 100 cm^2 area detector, 3–5 mm FWHM pixel size
Sample environments	Solid/liquid interface cells, solid/liquid interface Poiseuille shear cell, Langmuir trough, UHV evaporator, UHV oven

The LWTS coupled solid methane moderator provides an excellent basis for a broadband reflectometer with substantially better performance than that of the SPEAR instrument. The higher power of the LWTS and the improved long-wavelength neutron flux from this target-moderator geometry produce a relative gain in intensity (a factor of 15–30). Furthermore, the 10-Hz source pulsing frequency provides greater bandwidth than SPEAR and allows researchers to place the instrument farther away from the moderator, yielding more space for shielding. Experiments that require 1-h measurement times with SPEAR will be measurable in minutes by this instrument. We estimate that, when access to reflectivities below 10^{-4} is not required, we can perform meaningful studies of the kinetics of processes with timescales of a few minutes or less.

4.6 Grazing Incidence SANS Reflectometer

4.6.1 Requirements of the Science Community

The ability to measure structures in a range from the angstrom up to the micron size has major applications in structural biology and biotechnology — two rapidly growing disciplines. These applications include interfacial structure in drug delivery systems, membranes and their intermolecular interaction, protein adsorption and critical phenomena in fluid systems, biocompatibility, and sensors (see, for example, Ref. 4.6.1). Grazing incidence small-angle scattering (GI-SANS) allows researchers to access a much greater resolvable length scale than conventional SANS. Also, as noted by Gliss et al. [4.6.2], GI-SANS is complementary to atomic force microscopy but is able to probe internal composition by virtue of neutron contrast. Further applications involve studies of phase separation in polymer films, correlations among magnetic domains, inorganic templating at air/water interfaces [4.6.3], as well as investigations of complex fluids under flow, vesicles and gels, reaction kinetics, and surfactants at interfaces

Despite the wealth of information available from scattering at grazing incidence, few successful studies have been reported. The most significant reason for this is that all experiments have been conducted on instruments optimized for either SANS (with the sample placed in reflection

geometry and using only the intrinsic beam divergence for illumination) or reflectometry (using collimation tightened for the experiment). These awkward adaptations of existing instrumentation for tests of GI-SANS have furnished compromised results. The proposed instrument, designed for the purpose, will overcome these problems.

4.6.2 Instrument Design and Advantages

In reflection geometry, the specularly reflected beam and the diffusely scattered intensity are significantly offset from the incident beam. Thus, the detector shielding, while still necessary, does not limit the largest resolvable length scale. The GI-SANS instrument at the LWTS will be the first dedicated instrument optimized for such measurements and will be located on the most intense source of long-wavelength neutrons available. These factors will provide the LWTS with an instrument far surpassing any other available in the world. The GI-SANS instrument has similarities to the off-SPEC instrument proposed for the second target station at ISIS (shown in Fig. 4.7); However, the GI-SANS instrument would have greater flexibility, allowing movement of the two-dimensional detector to $\geq 90^{\circ}$ laterally. The inclusion of an additional one- or two-dimensional position sensitive detector (PSD) would enable simultaneous measurement of grazing incidence diffraction in parallel with specular/off-specular studies.

Table 4.10 lists parameters of the instrument.

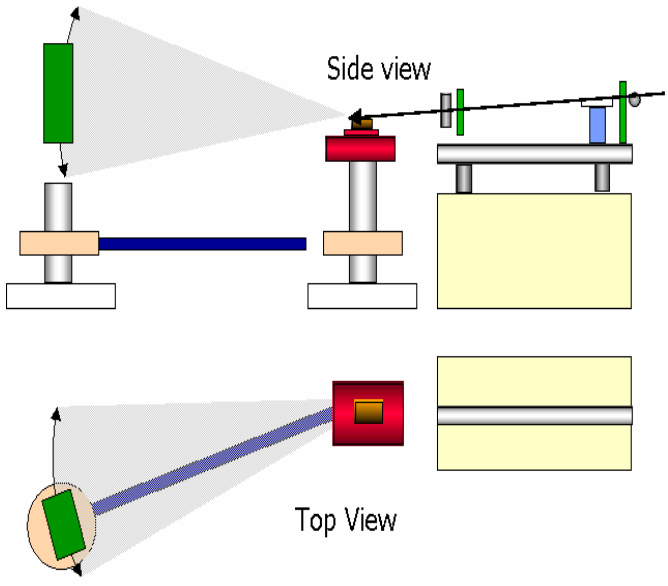

Fig. 4.7. Schematic illustration of a GI-SANS instrument.

Table 4.10. Instrument design parameters for the GI-SANS.

Component	Description
Moderator	Coupled S-CH_4 slab
Source-to-sample distance	17 m
Sample-to-detector distance	Variable, typically 6 m
Flight path	Bender, frame overlap mirror, λ > 20 Å), supermirror guide
Resolution	Variable 3–10% $\Delta Q/Q$
Nominal range of reflectivity	Better than 10^{-5}
Incident energy	1–20 Å

The broad-pulse, high-intensity beam available to the GI-SANS instrument from the LWTS coupled cold moderator is ideal for both small-angle scattering and reflectometry. This hybrid instrument simultaneously measures GI-SANS and grazing incidence diffraction data with specular and off-specular reflectivities, with emphasis on the former. Its design offers great flexibility in the choice of resolution and wave vector range; both can be optimized to the systems of interest.

Potentially large gains in flux are also possible through the use of spin-echo techniques [4.6.4]. This area of active study will be evaluated in detail at a later time. The distances listed in Table 4.10 are for the conventional instrument only.

4.7 Neutron Spin Echo Spectrometer

4.7.1 Requirements of the Science Community

Neutron spin echo is a proven technique for achieving very high energy resolution in a scattering experiment, examining slow dynamics in condensed matter, and directly measuring the intermediate scattering function S(Q,t). Its applications include virtually all types of soft condensed matter systems, polymers, complex fluids, and studies of glassy dynamics and magnetic fluctuations.

The current state of the art in terms of resolution is IN15, where the maximum measurable Fourier time t_{max} = 200 ns. Many soft-matter systems reveal interesting features only at low Q in SANS (e.g., $Q < 0.05$ Å^{-1}), where the relaxation is already too slow for current instruments to observe. An ambitious (but realistic) goal for a next-generation NSE instrument is to probe 1-μs Fourier times. The relaxation rate $\Gamma(Q) \sim Q$, so that extension to lower Q (mesoscopic structures) automatically requires larger t_{max}. However, it is necessary to achieve this extension while keeping the flux high and the background low.

4.7.2 Instrument Design and Advantages

The first NSE instrument, IN11, was built in the late 1970s (Mezei, ILL). NSE spectrometers now exist only at research reactor installations [4.7.1–4.7.5]. Further versions of this generic type are IN15, NSE-Jülich, NSE-NIST, MESS (Saclay), and C2-2 (JRR3, Tokai). Other instruments using NSE are SPAN (HMI), which has wide angular coverage but lower resolution and is otherwise similar to IN11; resonance (zero field) NSE (Saclay/Munich); resonance/TAS

on a triple axis spectrometer (HMI and Munich [planned]); coils on TAS (ILL, Zeyen); PONTA (Tokai); and SPINS (NIST).

Recently, measurements at IN15 configured in TOF mode demonstrated the feasibility of NSE on a pulsed source. While this instrument is still very much in the testing phase, the preliminary results are quite promising in two configurations: the standard configuration using 8- to 15-Å neutrons probed 0.03–200-ns Fourier times, while a configuration using 17.5- to 25-Å neutrons (reflected by a focusing mirror) provided access to 0.1–450-ns Fourier times — already a significant advance over the 200-ns maximum Fourier time that can be achieved with conventional NSE.

A TOF-NSE instrument such as the aforementioned maps out in one measurement a broad area in the Q–t plane, where t is the Fourier time, while a conventional NSE instrument quickly measures a broad range of Fourier times for a single value of Q. For simple diffusion processes, the information at the different values of Q is similar and can be combined, making TOF-NSE spectrometers competitive in performance with conventional, steady-state NSE instruments. In situations where the scattering function $S(Q,t)$ varies strongly with Q, the two classes of instruments are complementary. In these situations, a high-flux TOF instrument can rapidly map $S(Q,t)$ to identify the Q values of greatest interest so that the conventional spectrometer can precisely study the Fourier spectra at these values.

For reference, we record the expression for the Fourier time:

$$t = (2|\gamma_n|\mu_N m_n^2/h^3)\lambda^3 Bl \qquad [4.10]$$

where $t_{seconds} = 1.8635 \times 10^{-10} \lambda^3_{angstroms} (Bl)_{Tesla\text{–}meter}$

in which γ_n is the neutron gyromagnetic ratio, μ_N is the nuclear magneton, m_n is the neutron mass, h is Planck's constant, λ is the neutron wavelength, and Bl is the magnetic field integral along the precision path.

The Jülich/HMI collaboration intends to form an instrument design team to design an advanced NSE spectrometer at the HPTS, in anticipation of further developments at the European Spallation Source (ESS) (currently under consideration). As instrument design studies proceed, it will become clearer whether such an instrument would be better sited at the LWTS.

Our current plan is to roughly follow the design choices of IN11 (with appropriate improvements) for the first spallation-source instrument. This design, shown in Fig. 4.8, will resemble the Jülich or NIST spectrometer but will be more compact. Note that the second arm can rotate around the sample position to achieve larger scattering angles and larger Qs. Table 4.11 summarizes our preliminary estimates for key instrument parameters; we will refine these values after further optimization.

As part of this effort, we are investigating the possibility of using superconducting main coils, needed to reasonably access 1-μs Fourier times. The development of improved magnetic field correction elements is also a vital part of this preliminary study of NSE at spallation sources. In addition, we are considering other, more speculative concepts, including an instrument with

multiple second arms fixed in a ring around the sample for parallel measurements over a very broad range of Q and a SANS instrument that uses spin-echo techniques to access micron length scales [4.7.6].

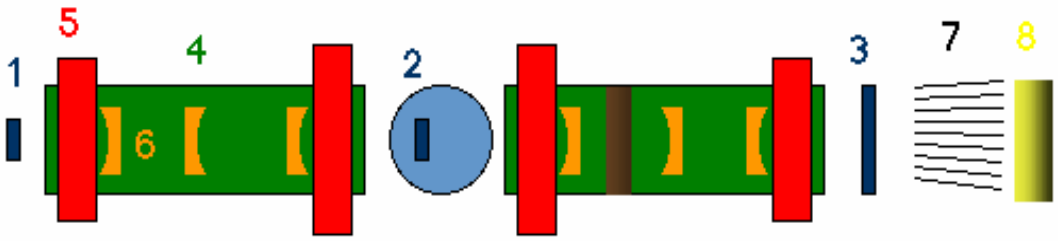

Fig. 4.8. Schematic illustration of a typical NSE spectrometer:

1. π/2 flipper (starts Larmor precession),
2. π flipper (performs equivalent of time inversion of spin at sample)
3. π/2 flipper (stops Larmor precession)
4. main solenoid (field integral < 0.5 T_m)
5. compensation coil (in anti-sense series with main coils; reduces coupling)
6. radial correction coil (satisfies echo condition for nonaxial and divergent neutrons)
7. polarization analyzer (radial array of polarizing supermirror blades), and
8. area detector (30 × 20 cm^2)

Table 4.11. Instrument design parameters for the NSE spectrometer.

Component	Description
Moderator	Coupled solid CH_4 slab
Source-to-sample distance	17 m
Sample-to-detector distance	5 m
Beam conditioning elements	Bender, frame overlap mirror, λ > 25 Å), supermirror guide, frame definition choppers, broadband transmission polarizers, broadband radio-frequency spin flippers
Resolution	Variable 3–10% ΔQ/Q
Fourier time range	0.05–1,000 ns
Incident wavelength	Variable 15-Å band, usually 7–22 Å

The NSE instrument at the LWTS will provide access to features of S(Q,t) at long length and time scales. Fourier times of 1 μs will enable researchers to study slow processes at mesoscopic scales that overlap with dynamic light scattering. The neutron pulse width from the coupled solid methane moderator produces a wavelength resolution $\Delta\lambda/\lambda$ around 5%, which allows better definition of the wavelength than is typical at reactor instruments (which use $\Delta\lambda/\lambda$ around ~10 to ~20%). The better definition provides additional benefits in terms of Q-resolution and reduction of echo-signal distortion.

A rough scaling argument, based on the time-average fluxes of the ILL cold source and of the LWTS coupled moderator, indicates that the LWTS TOF NSE would have a data rate at least three times that of the ILL TOF-NSE test, assuming otherwise comparable instrument configurations. The LWTS instrument will perform substantially better after optimization, providing still higher intensity, allowing access to 1-μs Fourier times, and opening new vistas in NSE spectroscopy.

4.8 Polarized Reflectometer

4.8.1 Requirements of the Science Community

Polarized neutron reflectometry (Pol-Ref) can unambiguously determine multiaxial magnetic depth profiles in systems of scientific and technological importance, such as spin valves and spring magnets. One application of the proposed instrument is to determine the size and distribution of magnetic domains and their correlation in magnetic materials. Until now, scientists could only infer certain information about the microscopic underpinning of the magnetization process through the application of models (Preisach models) of the hysteresis cycle, fitted to measurements of the depolarization of the beam transmitted through the sample and scattered at small angles. Only if a large range of wavelengths is available, as in a TOF instrument is it possible to monitor the consistency of the results.

4.8.2 Instrument Design and Advantages

The design of the LWTS polarized reflectometer allows researchers to measure reflectivities over a large range of momentum transfers without changing the instrument geometry. A full determination of the magnetic structure requires the free and independent choice of the neutron polarization axes before and after reflection (see Fig. 4.9). The full definition of the magnetic state of the sample requires that magnetic fields be applied to the sample according to a predetermined magnetic history. An assembly of three mutually perpendicular magnets satisfies that requirement. Table 4.12 lists the proposed instrument parameters for the polarized reflectometer.

The coupled S-CH_4 slab moderator of LWTS provides adequate resolution and high intensity for Pol-Ref, and the 10-Hz pulsing frequency enables efficient use of a broadband of wavelengths.

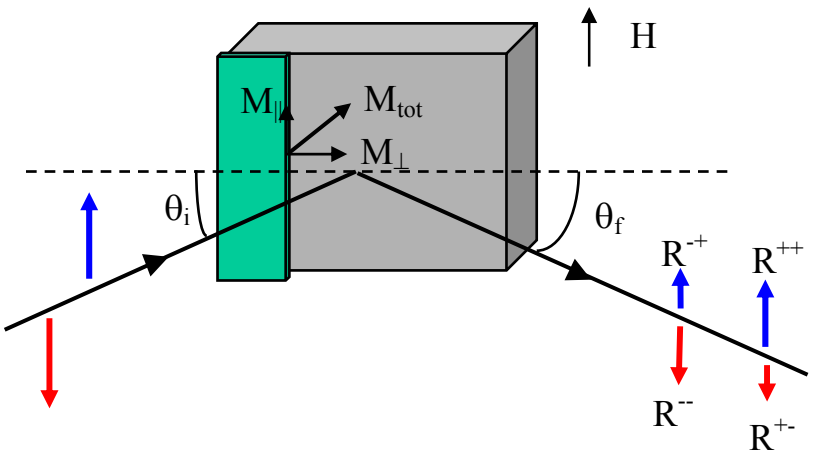

Fig. 4.9. Schematic illustration of Pol-Ref.

Table 4.12. Instrument design parameters for the Pol-Ref.

Component	Description
Moderator	Coupled S-CH_4 slab
Source-to-sample distance	18 m
Sample-to-detector distance	20 m
Footprint at sample	50 mm^2
Range of reflection angles: (2θ)	60°
Range of angles subtended by counter	10°
Range of angles subtended by analyzer	2°
Magnetic field	0 to 2 Tesla, in the x-y-z directions
Polarization	Polarizer/spin rotator in front of the sample, analyzer/spin rotator after the sample
Temperature	1.2–300 K

Final selection of incident and scattered beam polarization techniques will come only after carefully reviewing the progress of developments now underway. The similar magnetism reflectometer planned for the HPTS, with full polarization capabilities, utilizes systems of stacked polarizing supermirrors for incident beam polarization and scattered beam polarization analysis. Although ^{3}He spin filter technology is undergoing rapid development and may ultimately become viable for Pol-Ref and the HPTS instrument, limitations in the degree and constancy of polarization and the resulting transmission preclude its strong consideration in the near term. As with the HPTS instrument, Pol-Ref includes provisions for spin flippers downstream from the incident polarizer and upstream from the analyzer, along with field isolation for strong magnetic fields at the sample. Physical separation of polarization optics from the sample position accomplishes this isolation in some instances. Otherwise in extreme circumstances, additional electromagnetic guide field arrangements will be required to counteract the effects of the sample magnetic field.

The proposed LWTS polarized reflectometer provides for detailed studies of magnetic phenomena not possible before or elsewhere.

4.9 High-Resolution Chopper Spectrometer

4.9.1 Requirements of the Science Community

Among the spectrometers we describe, the direct geometry spectrometer — the high-resolution chopper spectrometer (HRCS) — is the one of greatest general utility. The scientific applications of such instruments demand definition of vector $\boldsymbol{Q}$, a wide, continuous coverage of ($\boldsymbol{Q}$, E) space, and incident energy selectable over a wide range, i.e., 1–1,000 meV. Studies of the dynamics of water in its many states, aqueous systems, and other liquids; dynamics of glassy solids; proton conduction in liquid electrolytes; and the behavior of water in cement require these capabilities.

4.9.2 Instrument Design and Advantages

The HRCS employs a chopper in the direct beam to generate incident neutrons of well-defined energy and a filter to define polarization. Linear position-sensitive detector (LPSD) arrays covering a very large solid angle record the intensities of the scattered neutrons, with energies

and polarization states determined by TOF and possibly spin analyzers. The goal is to achieve an efficient measurement of the scattering function S($\boldsymbol{Q}$, E; α, T, P, …) over a wide range of momentum transfer ($\boldsymbol{Q}$), energy transfer (E), and spin states (α) for a controlled sample environment characterized by temperature (T), pressure (P), and other parameters.

The HRCS offers the flexibility to access a wide range of continuous ($\boldsymbol{Q}$, E) space with tunable resolutions $\Delta\boldsymbol{Q}$ and ΔE. For experiments requiring different resolving power and intensity for distinct features of scattering, a user may select several incident energies, thereby varying the ($\boldsymbol{Q}$, E) range and ($\Delta\boldsymbol{Q}$ and ΔE) *without disturbing the sample*. The array of LPSDs enables the user to determine dispersion relations of collective excitations such as long-wavelength Brillouin scattering and spin-density waves in magnetic systems. Because of the wide dynamic range and good energy resolution, the HRCS can efficiently measure excitations of individual particles from atoms to macromolecules, including translational and rotational diffusion, quantum tunneling, and localized vibrations.

Optimization of the LWTS instrument will be in the direction of long-wavelength applications. Table 4.13 lists the proposed design parameters for the HRCS at the LWTS; Fig. 4.10 is a schematic illustration of the proposed instrument. The appropriate location for the HRCS is the decoupled front wing moderator (see Sec. 6), which will provide high-resolution pulses and admit short-wavelength as well as long-wavelength neutrons.

Table 4.13. Instrument design parameters for the HRCS.

Component	Description
Moderator	Decoupled S-CH_4 slab
Source-to-sample distance	25 m
Sample-to-detector distance	5 m
Flight path	Straight supermirror guide
Beam preparation	Multiple Fermi and/or disk choppers Spin polarizing filters
Flux at the sample	Variable depending on filters ~10^4 to 10^6 n/cm^2 sec
Resolution	1% < $\Delta E/E_0$ < 4%, $\Delta Q/Q$ better than 5%
Incident energy	0.2–100 meV
Detectors	1-D position PSDs from –20° to 140°

This spectrometer will be superior to all current world-class instruments, as Table 4.14 shows. The availability of polarization analysis will allow scientists to fully characterize magnetic scattering processes and discriminate against incoherent scattering. Polarized ^{3}He filters in the incident beam and in the scattered beams seem to be most appropriate choices for these functions. The resolution at low energies will surpass those of all the existing direct geometry cold-neutron spectrometers. The dynamic range is wide enough to overlap the epithermal-neutron energies with those of the chopper spectrometers at the HPTS, to which HRCS will be a powerful complement.

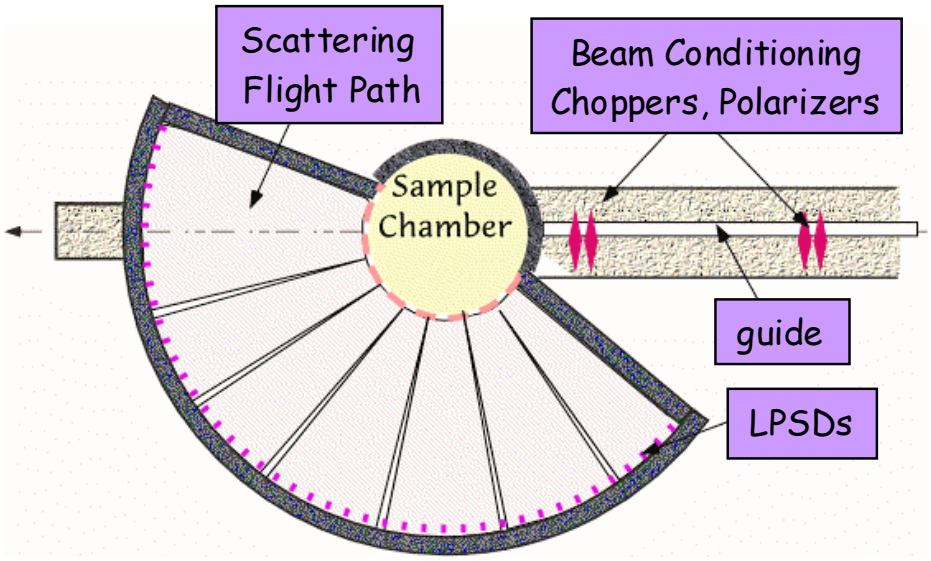

Fig. 4.10. Schematic illustration of the HRCS.

This instrument, comparable in scale with the current world's best, MAPS at ISIS, will provide resolution superior to that of MAPS, access to lower energies and wavevectors, and higher intensity on sample.

Table 4.14. Characteristics of comparable spectrometers world wide.

Instrument	Maximum E-Loss (meV)	ΔE (FWHM) Range μeV)	Polarized Beam Capability
This instrument, HRCS	**200**	**2–1000**	**Yes**
IN4-ILL	100	200–500	No
IN5-ILL	20	3–200	No
IN6-ILL	3	50–170	No
IN10-ILL	0.02	0.3–1.5	No
IN11-ILL	0.02	0.015	No
NEAT-HMI	15	2–2000	No
MIBEMOL-Saclay	15	20–2000	No
DCS-NIST	15	2–2000	No
MARI-ISIS	1500	100–30000	No
HRMECS-IPNS	800	200–32000	No
HET-ISIS	1500	100-30000	No
MAPS-ISIS	1500	100-30000	No

4.10 Protein Crystal Diffractometer

4.10.1 Requirements of the Science Community

Through hydrogen-bonding interactions, steric interactions, and charge compensation and transport, hydrogen plays an important role in the function of proteins. Consequently, a precise knowledge of the distribution of hydrogen atoms within protein molecular structures is critical. However, hydrogen is not easily observable in x-ray structures, and protein crystal structures are

difficult to measure on current neutron diffractometers because of limitations in flux and sample size.

4.10.2 Instrument Design and Advantages

The proposed protein diffractometer (PXD) enables fast and efficient measurement of Bragg intensities from macromolecular single crystals. This instrument consists of a Kappa or full-circle goniometer with an array of two-dimensional position-sensitive area detectors covering a large solid angle (up to five steradians). At the LWTS, the long-wavelength neutron spectrum and low repetition rate are well suited for a single-crystal macromolecular diffractometer, which will dramatically increase the number of protein and nucleic acid structures that can be determined. Table 4.15 lists the design parameters for the PXD at the LWTS; Fig. 4.11 is a schematic illustration of the proposed instrument. The decoupled solid CH_4 moderator of LWTS provides the wavelength resolution needed for PXD, and the low, 10-Hz pulsing frequency allows efficient use of a broadband of wavelengths.

The PXD collects full hemispheres of diffraction data with a resolution of 1.5 Å on macromolecule crystals (on the order of 1 mm^3 in volume) in a few days or less. These data, in combination with x-ray diffraction data, will provide direct observation of hydrogen atoms in waters of hydration and within protein molecules.

Figure 4.12 shows the ***k***-space covered by three of the six detectors of the PXD.

Table 4.15. Instrument design parameters for the PXD.

Component	Description
Moderator	Decoupled S-CH_4
Source-to-sample distance	30 m
Sample-to-detector distance	0.5 m
Flight path	Curved guide
d-Spacing range	1.5–10 Å
Resolution	$\Delta d/d \approx 4 \times 10^{-3}$ at $2\Theta = 90°$
Incident wavelengths	1–13 Å
Detector	Array of 2-D PSDs
Sample orienter	Kappa or full-circle goniometer

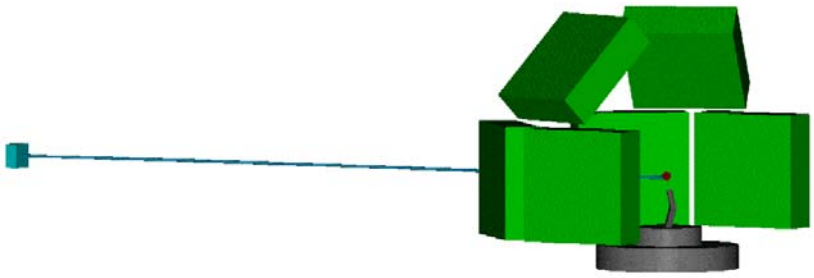

Fig. 4.11. Schematic illustration of PXD.

It is possible to achieve an increased neutron current density on the sample using focusing devices. A firm, XOS of Albany, N.Y., has developed a polycapillary optics technology that is

effective in focusing a beam of cold neutrons onto a small spot (Figs. 4.13 and 4.14a). This concept uses the property of total external reflection of neutrons at small grazing angles from smooth solid surfaces. Hollow glass capillary tubes, curved gently so that the incidence angle at each reflection is less than the critical angle, deflect the neutrons through angles up to several degrees. An array of thousands of such fibers then collects neutrons and takes them to a wavelength independent focus at a point. We have demonstrated the focusing ability of a monolithic optic (Fig. 4.14b) in the incident beam of the IPNS single-crystal diffractometer (SCD) as shown in Fig. 4.15. Such devices increase the flux on the sample but sacrifice angular resolution. The experimenter can adjust this compromise according to the needs of the experiment, possibly even synchronously as a function of time (wavelength).

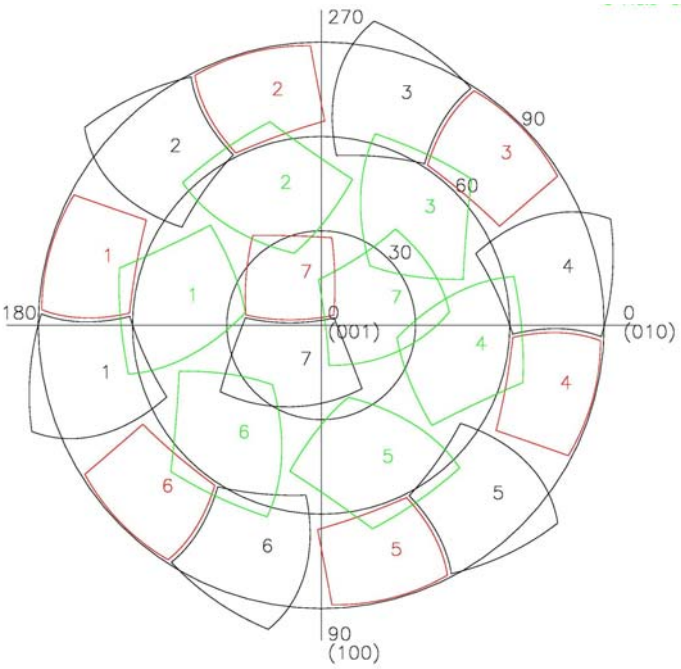

Fig. 4.12. Projection of three area detectors onto a sphere in Q-space for seven (numbered) orientations of the sample. These three detectors (distinct colors), in fixed locations, represent half of the detector array shown Fig. 4.11.

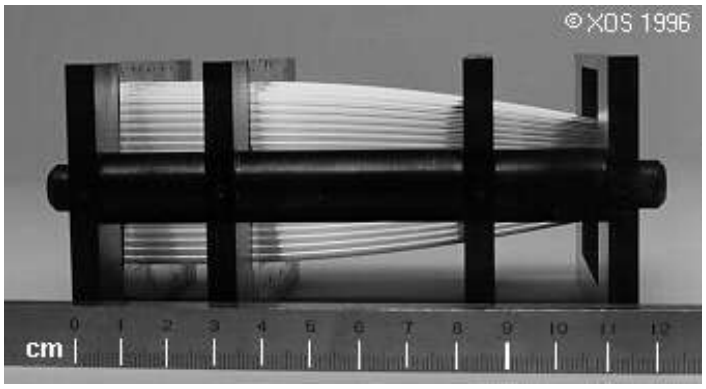

Fig. 4.13. Photograph of a multifiber polycapillary neutron focusing optic.

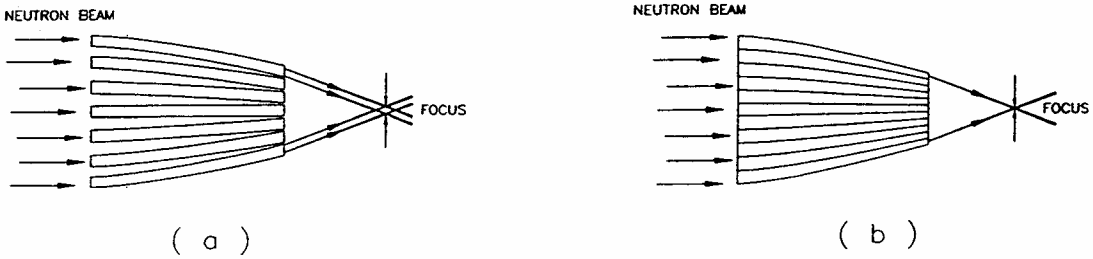

Fig. 4.14. Schematic drawings of (a) multifiber polycapillary neutron focusing optic and (b) monolithic polycapillary focusing optic.

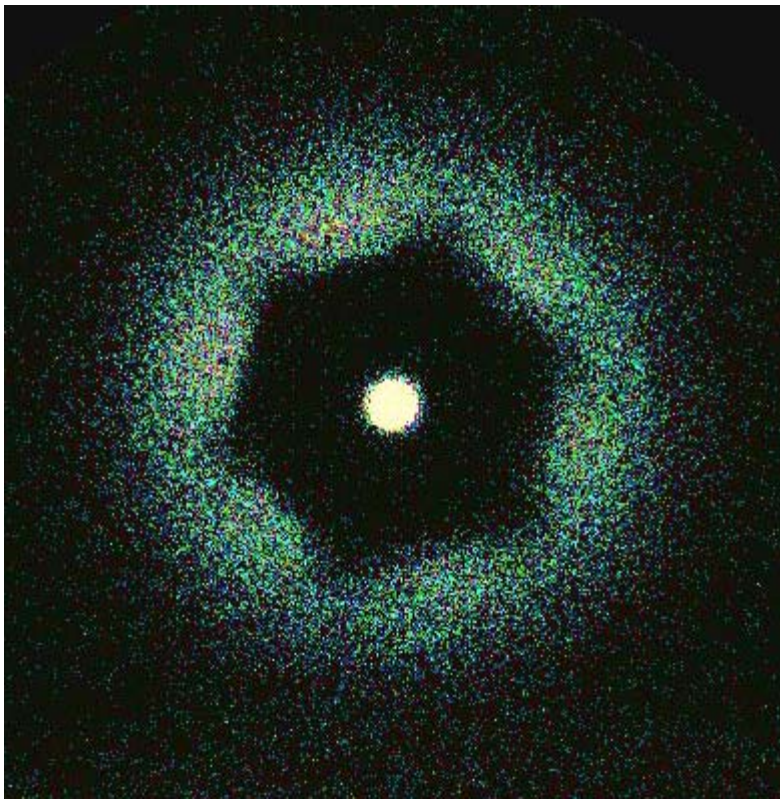

Fig. 4.15. Image of focused beam of neutrons on the IPNS SCD beamline with wavelengths of > 4 Å. The focal spot is about 0.5 mm in diameter, and the intensity in the spot is about six times the intensity without the optic.

4.11 Ultra-Cold Neutron Station

4.11.1 Requirements of the Science Community

The ultra-cold neutron (UCN) station will be the site of a variety of experiments, each with its own geometry, to be installed in sequence for periods of about six months to two years, to explore aspects of fundamental neutron physics. The beamline will be designed for flexibility and access, and thus will benefit from an extreme location on the beam cluster. The figure of merit for most cold-neutron-beam experiments is the capture flux (i.e., the flux weighted by $1/v$). In contrast, for the UCN source, we need the most neutrons possible at 9 Å without concern for

beam divergence. Many experiments are sensitive to the uniformity or symmetry of the neutron intensity distribution coming out of the guide (the more uniform and symmetric, the better).

Because these experiments are lengthy and limited by counting statistics, they are extremely sensitive to fast-neutron and gamma background and thus must be out of line of sight of the moderator and target assembly and must be well shielded. Table 4.16 summarizes the design parameters of the UCN station.

Table 4.16. Instrument design parameters for the UCN station.

Component	Description
Moderator	Decoupled slab
Source-to-detector distance	15 m
Flight path	3 m supermirror, compact bender; 4-m clear space for optics, choppers, etc; extreme of beam cluster
Detector	Flexible for 6-monthly changes
Ancillary equipment	Dilution refrigerator

4.11.2 Instrument Design and Advantages

To provide the largest possible area and divergence from the beam while maintaining uniformity and reducing the fast neutron and gamma background, the beamline should have the widest possible compact bender assembly (with a supermirror coating of around m = 3) and should efficiently pass neutrons with wavelengths greater than 1 Å. The beamline should also be relatively short (around 15 m) to allow for the use of a broad spectrum (up to 20 Å) with no pulse overlap in a large experimental apparatus. It should have up to 4 m available space for its own incident optics. In addition, certain experiments will require choppers for additional prompt-radiation background suppression (T_0 chopper), frame definition, and energy definition. For these experiments, researchers will require routine access to neutron flux monitors, supermirror polarizers and analyzers, and other neutron and gamma detectors for beam and background characterization.

To evaluate design details, we will complete simulations of the transmission efficiency and output beam profile for benders and chopper assemblies. These studies will contribute needed information for characterizing the beam in specific experimental installations.

Use of the beam as a UCN source requires a high-cooling-power dilution refrigerator. Specific experimental groups will supply other primary and ancillary apparatus when they install their experimental equipment.

The coupled cold slab moderator beam cluster at the LWTS, which provides the maximum per-pulse long-wavelength neutron flux, would be the ideal location for the UCN station. This station will also benefit from the large wavelength range accessible without frame overlap contamination that results from the 10-Hz pulse frequency. Because the sharpness of pulses is not a significant concern for any of the experiments currently envisioned, the long tail on the emission times from this moderator will not pose any difficulties.

4.12 References

4.1.1 J. Woenkhaus, R. Kohling, P. Thiyagarajan, K. Littrell, S. Seifert, C.A. Royer and R. Winter, *Biophysical J.,* in press (2000).

4.1.2 Y. Ishikawa, M. Furusaka, N. Nimura, M. Arai & K. Hasegawa (1986) J. Appl. Cryst. 19, 229-242.

4.1.3 R.K. Heenan & S.M. King, Proc. International Seminar on Structural Investigations at Pulsed Neutron Sources, Dubna, 176-184 (1993).

4.1.4 P. Thiyagarajan, J.E. Epperson, R.K. Crawford, J.M. Carpenter, T.E. Klippert, and D.G. Wozniak, *J. Appl. Cryst.*, **30**, 280-293 (1997).

4.1.5 P. Thiyagarajan, V. Urban, K. Littrell, C. Ku, D.G. Wozniak, H. Belch, R. Vitt, J. Toeller, D. Leach, J.R. Haumann, G.E. Ostrowski, L.L. Donley, J. Hammonds, J.M. Carpenter and R.K. Crawford, Proceedings of ICANS XIV - The XIV Meeting of the ICANS, June 14-19, 1998, Starved Rock Lodge, Utica, Illinois, edited by J.M. Carpenter & C. Tobin, Volume **2**, 864-878. Springfield, VA: National Technical Information Service.

4.1.6 P. Thiyagarajan, R.K. Crawford & D.F.R. Mildner, *J. Appl. Cryst.* **31**, 835-840 (1998).

4.1.7 P.A. Seeger, R.P. Hjelm, and M.J. Nutter, *Mol Cryst. Liq. Cryst*, **18A,** 101-117 (1990).

4.2.1 K. Lefmann and K. Nilesen, *Neutron News*, **10/3**, 20 (1999).

4.2.2 K. Herwig, Oak Ridge National Laboratory ES-1.1.8.4-6017-RE-A-00 (1999), and private communication

4.2.3 C.J. Carlile and M.A. Adams, *Physica B*, **182**, 431 (1992).

4.2.4 P. Allenspach and D. Engberg, PSI - Focus Progress Report (1998).

4.2.5 P. Han, H.C. Materials Corporation, private communication (1998).

4.2.6 J.M. Carpenter, *J. Appl. Cryst.*, **17**, 249–256 (1984).

4.2.7 J.M. Carpenter, *J. Appl. Cryst.*, **17**, 249–256 (1984).

4.6.1 P. Müller-Buschbaum, J.S. Gutmann, R. Cubitt, and M. Stamm., "Probing the In-Plane Composition of Thin Polymer Films with Grazing-Incidence Small-Angle Neutron Scattering and Atomic Force Microscopy," *Colloid Polym. Sci.*, **277:** 1193 (1999).

4.6.2 C. Gliss, H. Clausen-Schaumann, R. Günther, S. Odenbach, O. Randl and T.M. Bayerl, "Direct Detection of Domains in Phospholipid Bilayers by Grazing Incidence Diffraction of Neutrons and Atomic Force Microscopy," *Biophys. J.*, **74:** 2443 (1998).

4.6.3 W.A. Hamilton, P.D. Butler L.J. Magid, Z. Han and T.M. Slawecki, "Fast Relaxation of a Hexagonal Poiseuille Shear-Induced Near-Surface Phase in a Threadlike Micellar Solution," *Phys. Rev. E*, **60:** R1146 (1999).

4.6.4 W.G. Bouwman, M. van Oossanen, O. Uca, W.H. Kraan and M.T. Rekveldt, "Development of Spin-Echo Small-Angle Neutron Scattering", *J. Appl. Cryst.*, **33:** 767 (2000).

4.7.1 F. Mezei (ed.), "Neutron Spin Echo", Notes in Physics, vol. 128, Springer, Berlin (1980).

4.7.2 M. Monkenbusch, R. Schaetzler, D. Richter, *Nucl. Inst. Meth.*, **A399:** 301-323 (1997).

4.7.3 B. Farago, G. Ehlers, G. Kali, and A. Wischnewski, "The First Time-of-Flight Echo," ILL report (2000).

4.7.4 M. Koppe, Gahler et al, *Physica B*, **266:** 75-86 (1999).

4.7.5 http://www.ncnr.nist.gov/-reference list of NSE papers under NG-5 NSE.

4.7.6 W.G. Bouwman, M. van Oossanen, O. Uca, W.H. Kraan, and M.T. Rekveldt, "Development of Spin-Echo Small-Angle Neutron Scattering," *Appl. Cryst.*, **33:** 767–770 (2000).

4.1.1 J.M. Carpenter, “Time Focusing of Pulsed-Source Crystal Analyzer Spectrometers I. General Analysis,” *Nucl. Inst. Meth. Phys. Res.* (2001) in press.
4.1.2 J.M. Carpenter, E.B. Iverson, and D.F.R. Mildner, “Time Focusing of Pulsed-Source Crystal Analyzer Spectrometers II. Practical Expressions,” *Nucl. Inst. Meth. Phys. Res.* (2001) in press.
4.1.3 D.F.R. Mildner and J.M. Carpenter, “Time Uncertainty for Guided Long-Wavelength Neutrons on a Pulsed Neutron Source,” submitted to *Nuc. Inst. Meth. Phys. Res.* (2001).
4.1.4 J.M. Carpenter and J. Faber, Jr., "Design Study of a Time-of-Flight Small-Angle Diffractometer for a Pulsed Neutron Source," *J. Appl. Cryst.*, **11**, 464–465 (1978).
4.1.5 J.M. Carpenter, *J. Appl. Cryst.*, **17**, 249–256 (1984).
4.1.6 P. Thiyagarajan, J. E. Epperson, R. K. Crawford, J. M. Carpenter, T. E. Klippert, and D. G. Wozniak, "The Time-of-flight Small-Angle Neutron Diffractometer at IPNS," *J. Appl. Cryst.*, **30**-, 280–293 (1997).
4.1.7 T. Keller, A. Wiedenmann, T. Krist, A. Danzig, U. Keiderling, G. Steiner, F. Mezei, "Design and Performance of the Polarized Beam at the SANS Instrument at the BER II Reactor", submitted to *J. Nucl. Instrument.*

5. CONVENTIONAL FACILITIES

5.1 Introduction

The proposed LWTS building offers a serviceable and appropriately shielded environment for the LWTS neutron-scattering research programs. The building (a) shelters the experiment facilities for most of the scattering instruments; (b) meets their space and utility requirements; (c) encloses the proton beamline shielding; (d) provides a hot-cell complex used for target systems maintenance; and (e) houses the electrical, cooling, waste, and HVAC systems that serve the proton beamlines, the target-moderator-reflector-shield assembly, and the experimental facilities. To save design and construction costs, the LWTS building will be identical to the HPTS building

5.2 Long-Wavelength Target Station Building

The LWTS building consists of two main areas: (1) the non-nuclear facility, which includes the experiment hall and associated neutron scattering instruments, and (2) the nuclear facility, which contains the target, the high bay, the bulk shielding, the maintenance hot-cell complex, target primary utility systems, and the waste handling systems.

The large main floor contains the target area, the instrument floor area, and the target and instrument shops. A partial basement houses utility systems and waste handling systems. This basement also provides a secure and controlled area for loading casks of activated and/or contaminated materials and devices onto trailers for transport to other locations. The design of this area is a structure configured to transfer the extremely heavy loads of the target area shielding to the building foundations.

The location of the target cell on the main floor enables large floor areas on either side for neutron instruments. A high bay over the target cell provides for controlled access to the target area, removal and replacement of the moderator components, and servicing of the target monolith. This high bay extends the length of the main building. Ther high bay area is also a cryogenic refrigeration room with a hydrogen equipment room (HER).

In addition the LWTS building includes several small satellite buildings that house the instruments for beamlines that extend beyond the enclosed instrument floor. A compressor building located adjacent to the LWTS building houses the helium compressor and systems supporting the cryogenic equipment in the high bay area. A support pad outside the target building will contain a hydrogen storage tank, with blast protection.

The proposed target control room offers space for operator workstations, equipment racks, and safety-related control equipment. The room has a raised floor for equipment cables and cooling.

5.3 Structural and Architectural Considerations

The LWTS building supports, encloses, and protects equipment and personnel from normal environmental conditions and natural phenomena (e.g., seismic activities, wind, flood) as

required for PC-2 structures in DOE STD 1020-94. The 1997 Standard Building Code has been used as the building code of record. Wind design is in accordance with ASCE 7-95 and is based on a wind speed (gust) of 90 mph with exposure (C) and an importance factor of 1.07. Seismic design is in accordance with the 1997 Uniform Building Code and the site-specific seismic response spectra. Inelastic code reduction factors (R) are applied only to the earthquake portion of the total design load. No R factor is applied to the wind loads. To limit inelastic behavior, R is not greater than 1.75.

The design floor live loads in the LWTS building vary depending on shielding, equipment loads, fork truck loads, etc., but in no place are they designed for less than 500 psf.

The HER houses active components of the cryogenic moderator system, such as the circulators and related valves. It is not expected to be a radiological area, and the major hazard in the HER is hydrogen.

6. TARGET AND MODERATOR NEUTRONICS

The LWTS includes state-of-the-art features applicable to long-wavelength neutrons, uniquely combined to enhance the intensities and pulse characteristics of neutron beams: a vertically extended target; tall slab moderators; a tall, upstream wing moderator; pelletized cryogenic moderators; premoderators; and a combination of decoupled poisoned moderators and a grooved coupled moderator. The target is tungsten with D_2O cooling, which is the most efficient possible in the 333-kW proton beam, and the reflector is beryllium, the most effective in all its impacts.

We arrived at this combination of features in the target/moderator/reflector system on the basis of careful consideration of worldwide experience and recent developments and after extensive Monte Carlo neutronic simulations. We carried out a certain amount of parameter optimization, but there remains a need for further refinement. We responded to those who formulated the scientific requirements in numerous disciplines and delivered extensive guidance to the instrument designers, who responded with suggestions. In this section, we record indicative assessments of the several alternatives that we have identified and representative appraisals of systems that remain subject to detailed optimization. We expect that as refinements of instrumental needs become evident, appropriate choices and compromises will become clear.

This section reports the results of neutronics calculations performed for the LWTS target station described in Sec. 2. The following discussion describes the models and methods used, thoroughly characterizes the base case, reports on the results of sensitivity studies, and briefly discusses target activation and afterheat. Sec. 8 discusses heat deposition in the target and moderator in detail.

6.1 Computational Model

We used the Monte Carlo radiation transport code MCNP-X version 2.1.5 [6.1.1] to calculate moderator performance and thermal power generation in the target and moderator systems. While MCNP-X is still considered a beta-release code, it is based on the LAHET [6.1.2] and MCNP [3] codes, which are well-accepted standard codes for this type of analysis. MCNP-X has the advantage that it calculates both the high-energy ($E > 20$ MeV) and low-energy ($E < 20$ MeV) portions of the calculation for all particles. The code employs the Bertini model, which is generally accepted for particle energies less than 3 GeV, for the intranuclear cascade calculation. We used no pre-equilibrium particle emission, since we found no difference in results with that feature turned on.

The MCNP-X code employs a combinatorial geometry that represents the physical system using generalized quadratic surfaces to define cell boundaries. The modeled system is somewhat simpler than the actual design of the target station. For example, the model does not include coolant pipes for moderators and approximates the multiplicity of nested vessels surrounding the moderators as single homogenized volumes. However, the model provides sufficient detail to obtain adequate estimates for quantities such as neutron beam characteristics of the moderators and energy deposition in the moderators and target.

The basis of most calculations is a 1-GeV proton beam with a two-dimensional beam current density profile (see Fig. 6.1) represented in terms of an error function with the equations

$$\rho(r) = \rho(x,y) = \begin{cases} \frac{1}{2}\left[1 + erf\left(\frac{r_0 - r}{a}\right)\right] & r < r_0 \\ \frac{1}{2} erfc\left(\frac{r - r_0}{a}\right) & r > r_0 \end{cases}$$

where $r = \sqrt{x^2 + y^2}$, $r_0 = \sqrt{x_0^2 + y_0^2}$, x_0 and y_0 are defined by the ellipse $\left(\frac{x_0}{7.5}\right)^2 + \left(\frac{y_0}{2.5}\right)^2 = 1$, and $a = 1.52 \cdot (r_0/7.5)$ [chosen so that $\rho(10,0) = 0.01$].

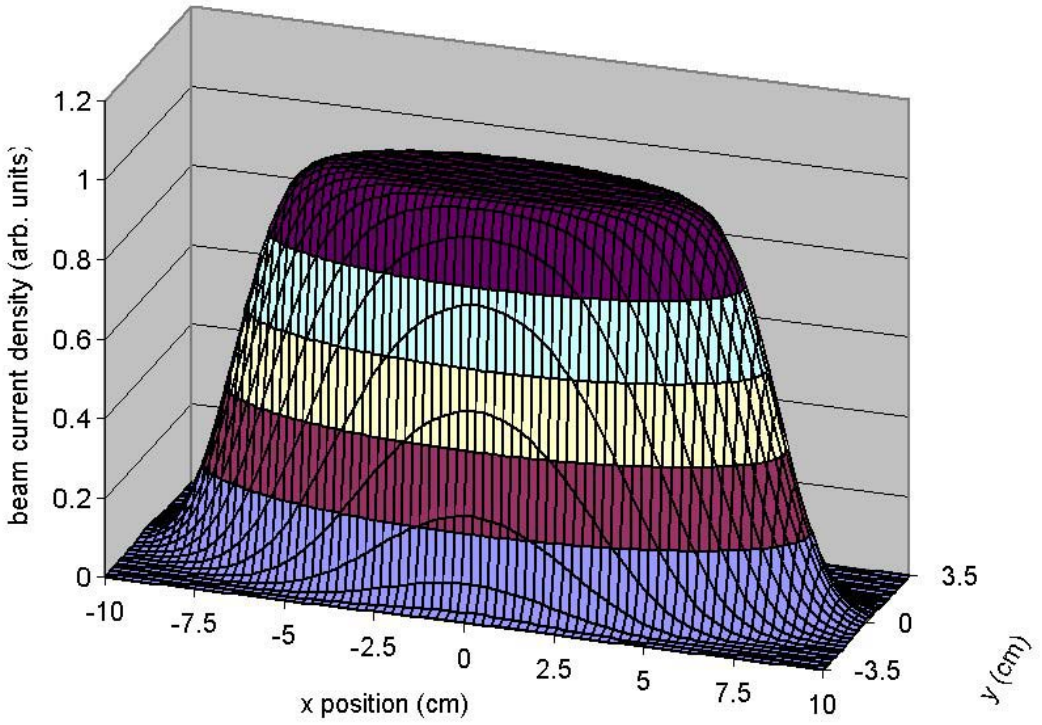

Fig. 6.1. Proton beam profile used for neutronics analysis of LWTS.

The reference model (Fig. 6.2) contains three moderators adjacent to the neutron-producing target, two in slab geometry and one in a wing position upstream of the target. The "port slab" moderator is the slab moderator to the left of the target when viewed from the perspective of the incident proton beam. It is fully coupled to the reflector. It consists either of solid methane at 22 K (90% by volume) and aluminum (10% by volume) or of liquid hydrogen at 20 K. Each moderator material has its own particular advantages and disadvantages, and the choice between the two materials should be based on the needs of instruments that view the moderator. The "starboard slab" moderator is to the right of the target when viewed from the perspective of the incident proton beam. It consists of solid methane at 22 K (90% by volume) and aluminum (10% by volume). It is decoupled from the reflector with cadmium and poisoned with gadolinium at a depth of 2.5 cm beneath the viewed surface. The front wing moderator is on the

starboard side, just upstream of the target. It consists of either liquid methane at 100 K or the methane-aluminum mixture at 22 K, and it is decoupled with cadmium and poisoned with gadolinium at a depth of 2.5 cm beneath the viewed surface. We present results for all of these moderator materials.

Table 6.1 summarizes the important neutronics parameters of the LWTS reference model.

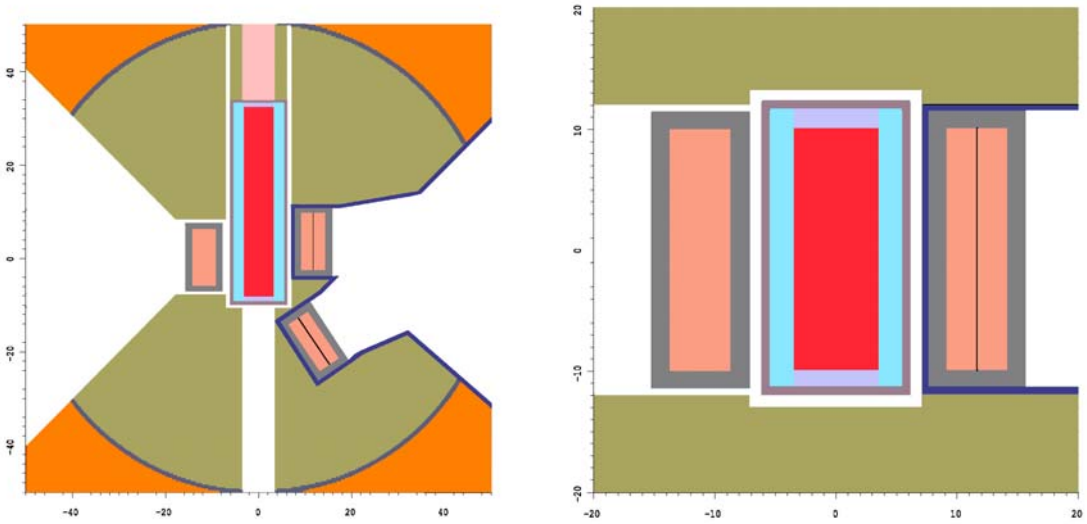

Fig. 6.2. Horizontal (left) and vertical (right) cutaway views of the LWTS neutronics model (decoupler layer not to scale). Protons are incident from below in the left panel.

Table 6.1. Geometrical and material features of the MCNP-X LWTS neutronics model.

Component	Geometry and Dimensions	Material
Target	Rectangular plates 7 cm wide × 20 cm tall	Tungsten
Housing	Rectangular, 0.6 cm thick	Stainless steel
Coolant	Channel gap between plates 0.1 cm; 1 cm thick above and below target	Heavy water
Premoderator	2 cm-thick region on target sides	Light water
Moderators		
Coupled slab	20 cm tall × 12 cm wide × 5 cm deep	L-H_2 or S-CH_4
Decoupled slab	20 cm tall × 12 cm wide × 5 cm deep	S-CH_4
Decoupled wing	20 cm tall × 12 cm wide × 5 cm deep	Liquid or solid S-CH_4
Decoupler	1 cm around decoupled moderators and neutron beamlines (except moderator faces)	Cadmium (diluted), density 0.0046 atoms/bn-cm
Poison	50 μm thick	Gadolinium, density 0.0304 atoms/bn-cm
Reflector	Cylinder, 100 cm diameter × 100 cm high	Heavy-water-cooled Be
Shield	Radially to 6 m, vertically ± 4 m	Water-cooled Fe

All three moderator materials have a high hydrogen density (L-H_2 to a lesser extent), which makes them very efficient moderators. By proper choice of overall thickness and poisoning depth, it is possible to tune each moderator to optimize trade-offs between neutron pulse width,

spectral temperature, and overall flux as appropriate for the instruments. We have not yet undertaken optimizations of this type, so the performance figures given here can be improved upon. In any case, the moderators provide a high standard of performance.

6.2 Quantities Calculated

The spectral intensity *i(E)* of a moderator is a measure of the number of neutrons leaving the entire viewed face of the moderator, per unit solid angle in the direction of view (customarily, normal to the viewed moderator surface) at a particular energy *E*. It is related to the differential flux $\phi(E)$ at a point some large distance, *L,* from the moderator through a "$1/r^2$" relationship. That is,

$$i(E) = L^2 \, \phi(E)\big|_L \, ,$$

where the flight path is normal to the viewed moderator face. This intensity characterizes the moderator independently of the distance from which it is viewed. If the flight path is not normal to the moderator face, the observed intensity is approximately proportional to the cosine of the angle between the direction of view and the normal to the moderator surface (Lambert's Law).

The code calculates the spectral intensities in two ways: by point detector tallies, which give rapid convergence, absolute scaling, and directional sensitivity, and by leakage current tallies, which provide intensities for high-energy neutrons (the way that the point detector tally works in MCNP-X does not permit contributions from high-energy neutrons). The use of slab moderators requires careful examination of the high-energy neutron source term. Therefore, we calculate the spectral intensities up to 500 MeV using leakage current tallies, which we normalize using point detector results in an energy range where both tallies function properly.

The emission time distribution *i(E,t)* of the moderator for a given neutron energy, also called the pulse shape function, is simply the intensity distribution as a function of the time at which the neutrons leave the viewed moderator surface following a delta-function proton pulse at time $t = 0$. The spectral intensity is the time integral of the pulse shape function,

$$i(E) = \int_0^\infty i(E,t)\, dt.$$

The emission time distribution of the neutrons leaving the moderator is presumed to depend on the viewing angle only in the scaling of the overall intensity. The energy and time bins for the MCNP-X calculations provide 10 energy bins and 20 time bins per decade, such that $\Delta E/E \approx$ 23% and $\Delta t/t \approx$ 11%. The reported results are differential values averaged over such bins. Emission time distributions are calculated by surface-averaged leakage current tallies that are normalized by point detector intensity tallies.

In some instances, we present intensity on a per-proton basis, in others, on a per-pulse or per-second basis. For LWTS conditions, 1-GeV protons, 333 kW, and 10 Hz, each 33.3-kj pulse contains $N_p = 33.3$ μA-sec $= 2.08 \times 10^{14}$ protons.

6.3 High-Energy Neutron Distribution Around the Target

High-energy neutrons dominate the shielding requirements around any spallation target. We carried out a simple calculation of the distribution of high-energy neutrons from the target to provide a basis for shielding design and to aid in understanding the neutron physics of the system. The model consisted of the tungsten plates from the LWTS target and a 10-m evacuated sphere for tallying the neutron current. Fig. 6.3 shows the neutron energy spectrum for selected angular ranges around the LWTS target, as calculated using a leakage current tally. In the figure, the zero angle corresponds to the direction of the incident proton beam. The figure shows that the energy spectrum in the forward direction is much harder (shifted to higher energies), which is a result of the kinematics of the spallation reaction. The overall neutron yield per unit solid angle is also higher in the forward direction. The evaporation neutrons around 1 MeV are produced isotropically but do not appear so in the curves because of attenuation in the target at the forward and backward angles. The same data appear in Table 6.2. The total neutron leakage from the target is about 20.5 neutrons per proton.

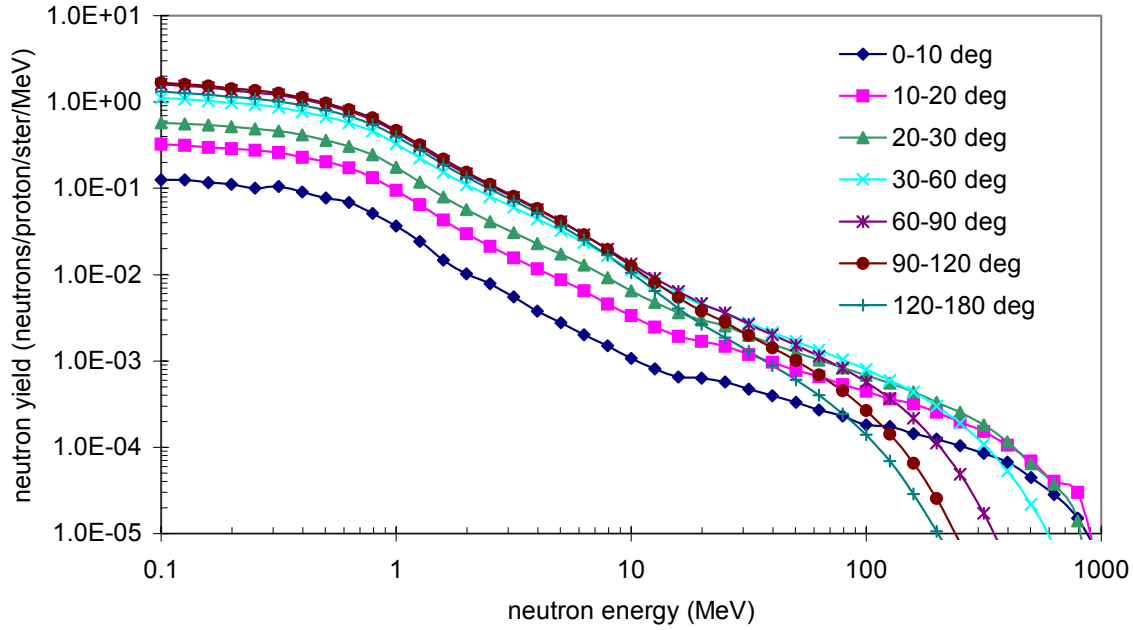

Fig. 6.3. Neutron energy spectra in selected angular ranges around the LWTS target.

Table 6.2. Neutron yield per solid angle in selected energy ranges around the LWTS target.

	Angular Neutron Yield (neutrons/proton/ster)			
Angular range (degrees)	E_n < 1 MeV	1 MeV < E_n < 20 MeV	E_n > 20 MeV	Total
0–10	0.087	0.048	0.074	0.210
10–20	0.227	0.141	0.151	0.518
20–30	0.409	0.269	0.206	0.884
30–40	0.595	0.393	0.222	1.211
40–50	0.767	0.495	0.216	1.479
50–60	0.912	0.568	0.200	1.680
60–70	1.021	0.617	0.176	1.814
70–80	1.094	0.640	0.150	1.883
80–90	1.127	0.637	0.124	1.888
90–100	1.138	0.636	0.103	1.877
100–110	1.142	0.640	0.087	1.870
110–120	1.117	0.630	0.074	1.820
120–130	1.067	0.608	0.063	1.738
130–140	0.995	0.576	0.055	1.626
140–150	0.902	0.538	0.049	1.489
150–160	0.802	0.496	0.044	1.342
160–170	0.698	0.455	0.041	1.194
170–180	0.610	0.426	0.039	1.075

6.4 Neutron Spectra and Pulse Widths — Reference Model

6.4.1 Neutron Spectra

The time-averaged neutron spectral intensity $E \cdot i(E)$ from a moderator at a pulsed source is the number of neutrons per steradian per unit lethargy per unit time. It can be represented by a Maxwellian thermal spectrum joined to a nearly - 1/E epithermal spectrum. It has the form

$$E \cdot i(E) = I_{th}\left[\frac{E^2}{E_t^2} e^{-E/E_t}\right] + I_{epi}\,\Delta(E)\left[\frac{E}{E_{ref}}\right]^{\alpha}$$

of a modified Westcott spectrum. In this equation, E_t is a characteristic energy of the Maxwellian portion of the spectrum; $\Delta(E)$ is a joining function that goes smoothly from 0 (for E far below about $5E_t$) to 1 (for E well above about $5E_t$); E_{ref} is a reference energy, typically taken to be 1 eV; and α is a constant, the "leakage exponent," with a value of about 0.05. Parameters I_{th} and I_{epi} are scaling constants for the thermal and epithermal portions of the spectrum, respectively. We use fits of this equation to the MCNP-X output data to characterize the neutronic performance of the moderators and to investigate the effects of changes introduced into the models. For the coupled moderators, there is a significant thermal-neutron leakage component from the reflector that appears at all angles but most strongly at large angles to the surface normal. To account for this in the process of data fitting, we add a room-temperature thermal term to the afore-mentioned equation corresponding to reflector-leakage neutrons. The coefficient for this term is

always much smaller than that for the moderator thermal intensity; it is not reported in any of the following tables.

For the reference geometry using flat moderators, Fig. 6.4 shows the neutron intensities for directions normal to the moderator faces. For the coupled moderators, liquid hydrogen provides a higher spectral intensity than solid methane over nearly the entire energy region. Solid methane has the advantage as a coupled moderator over the energy range 0.15–5 meV and might be preferred if the instruments viewing the coupled moderator are primarily tuned for these neutron energies. The front wing moderator using solid methane gives integrated thermal neutron intensity about 62% that of the coupled slab, with the 1-eV intensity about 60% that achieved in the coupled slab. With liquid methane in the front wing position, the moderator gives integrated thermal neutron intensity about 92% of that for the solid methane decoupled slab but at energies characteristic of the higher temperature material (i.e., the peak occurs at around 20 meV rather than at about 5 meV for the solid methane).

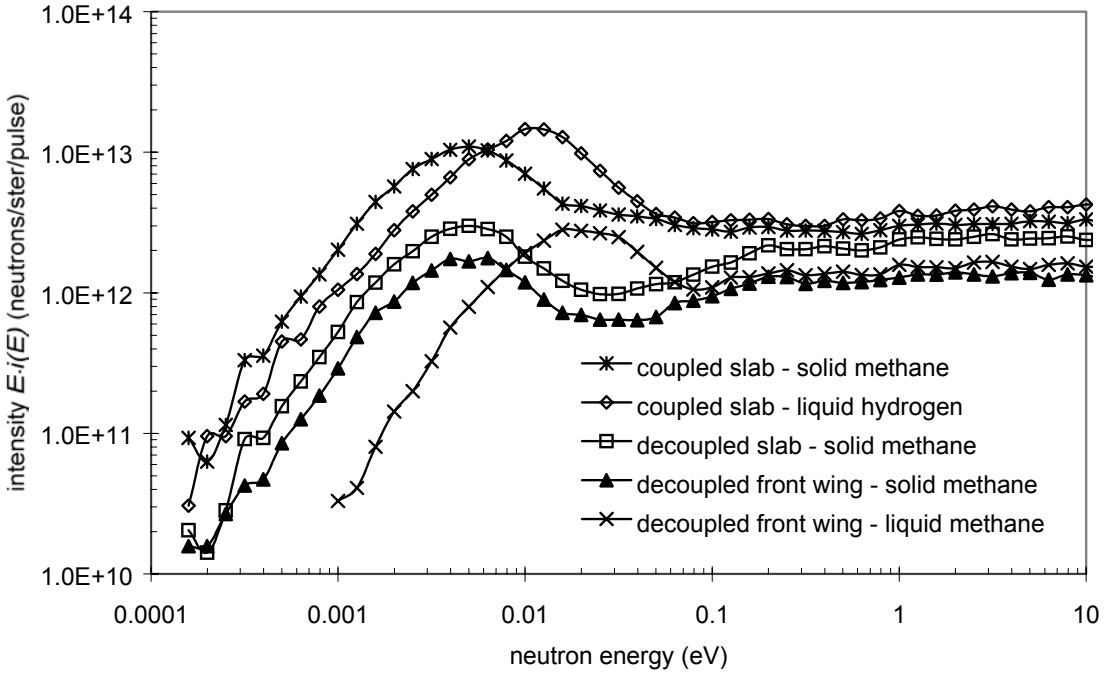

Fig. 6.4. Neutron spectral intensity for selected moderators, for the reference case described in the text.

6.4.2 Neutron Pulse Widths

The pulse shapes of neutrons emerging from a moderator are highly energy dependent (referenced to the time of crossing the viewed moderator surface) but do not depend significantly on emission angle. The widths of these pulses can be changed dramatically by varying the moderator material, its overall thickness, and the poisoning and decoupling parameters. In general, for a given moderator material, when the poison depth varies, intensities vary roughly inversely with the square of the pulse full width at half maximum at any energy. The premoderator geometry may also have an effect. Thus, there are a large number of degrees of freedom that can be varied to optimize moderators for the requirements of specific sets of instruments.

Figure 6.5 shows the energy-dependent pulse widths, FWHM, for the moderators we have considered in the reference model. In this figure, the FWHM for each moderator at each energy is that estimated by fitting the time dependence with a log-normal distribution which usually provides an acceptable result for this purpose. The flat (decoupled) methane moderators all have roughly the same pulse width for neutron energies above 0.1 eV, below which the liquid methane moderator exhibits a broader pulse. Liquid hydrogen exhibits a significantly broader pulse than the decoupled moderators at all energies, which is compensated somewhat by a higher spectral intensity overall.

The FWHM values reported here are only representative values. Pulse shape details have an important effect on the performance of a given instrument. Small changes in the decoupling and/or poisoning can give rise to variations by a factor of 2 in I_{th} and to correspondingly large variations in the pulse width. Because of the many opportunities for optimizing moderator performance, moderator details will necessarily be optimized in conjunction with instrument design. Moreover, moderator choices are likely to change many times over the life of the facility. The LWTS target/moderator/reflector system arrangement facilitates these changes.

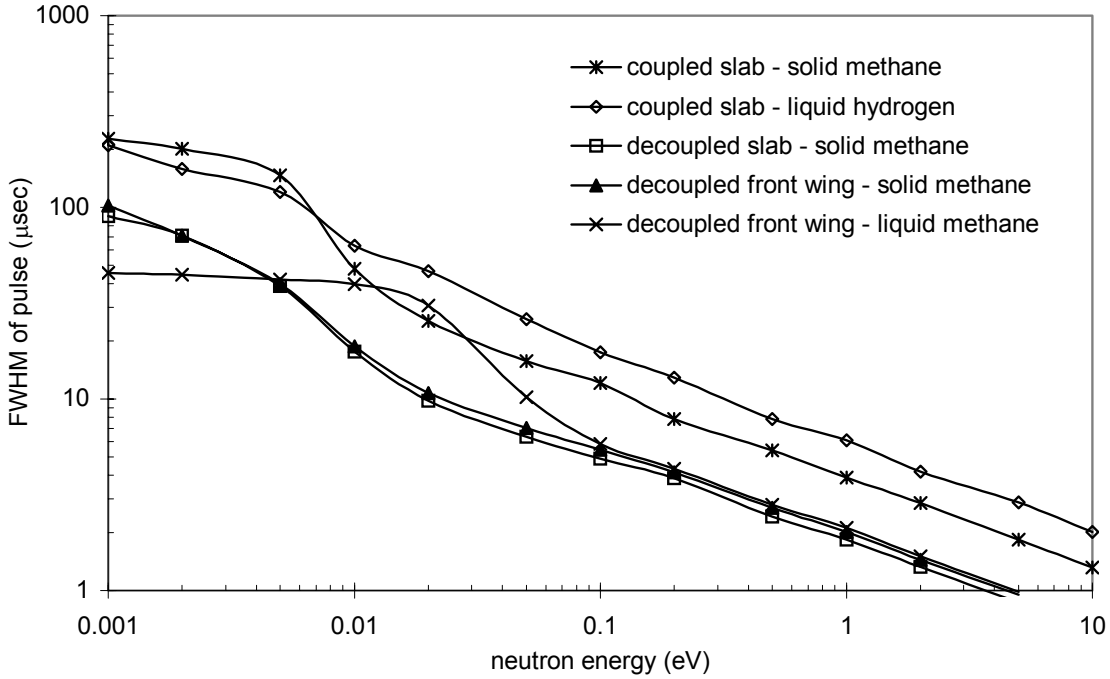

Fig. 6.5. Pulse width (FWHM) for selected moderators as a function of neutron energy.

6.5 Sensitivity Studies

We performed a large number of sensitivity studies to guide the target and moderator design process. Most of these had the objective of determining the effects of a single change around a point design and do not represent rigorous attempts to optimize design parameters. Taken as a whole, they point to the directions one should take in performing system optimizations. We describe some of these in the next section.

6.5.1 Target Position Relative to Moderators for the Slab Moderator Configuration

We calculated the effect of target-moderator position by varying the position of the target in a geometry similar to that in Fig. 6.2. For this study, we fixed two slab moderators on opposite sides of the target at the center of the reflector and shifted the target axially from the nominal position (target material starts 4 cm upstream from the reflector center) to determine the location of maximum performance.

Figure 6.6 shows the relative values of the intensities I_{th} and I_{epi} for the coupled and decoupled slab moderators as functions of the axial position of the target. The results show that the intensities occur at or near the nominal axial positions of the slab moderators and that the peak is not sharp, but allows for some axial movement of the moderators about the optimum position without sacrificing a great deal of moderator performance. Examination of these results also shows that the thermal neutron intensity in the coupled moderator is less sensitive to large variations in target position than the epithermal intensity. This is because the reflector storage component plays a significant role in coupled moderator performance.

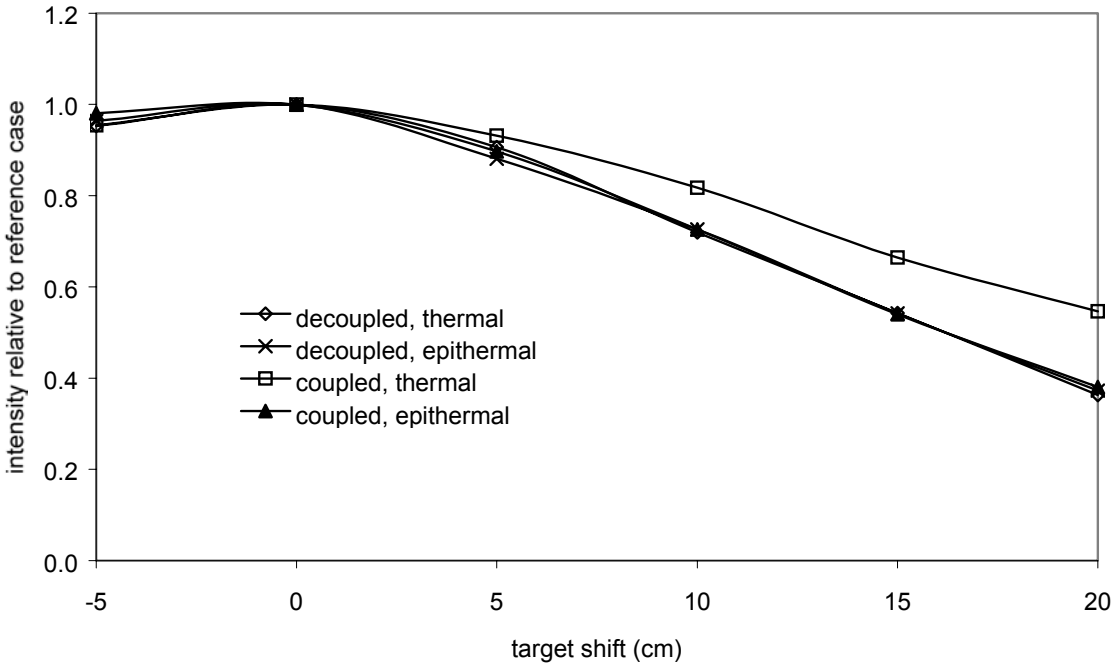

Fig. 6.6. Intensities of thermal and epithermal neutrons relative to their values at the nominal position, as functions of target shift (positive values move target upstream).

6.5.2 Beam Void Opening Angle for the Slab Moderator Configuration

The LWTS configuration has only three moderators, which maximizes the use of those moderators through curved guides. The motive of maximizing the number of beams and instruments, led us to consider broad angular access to the high-performance slab moderators, up to the 90° used in the reference case. We studied the effect of the beam opening angle for the coupled moderator by performing a calculation with this angle at 64°, permitting nine beamlines with 8° between adjacent beamlines.

Table 6.3 gives the results of this calculation for beamlines normal to the moderator faces. This table shows a major impact on thermal neutron intensity of the coupled slab moderator as reflector material is removed but the other moderators are little affected. Presumably, widening the reflector opening in front of the other moderators would similarly reduce their thermal intensity. To minimize the impact of wide openings, future design work must carefully examine the number and type of instruments that would view the coupled moderator.

Table 6.3. Thermal and epithermal spectral parameters for two different values of reflector opening angle at the coupled slab moderator (units are n/sr-pulse).

	Front Wing		Coupled Slab		Decoupled Slab	
	I_{th}	I_{epi}	I_{th}	I_{epi}	I_{th}	I_{epi}
90°	1.68E+12	9.04E+11	9.69E+12	2.20E+12	4.43E+12	2.31E+12
64°	1.70E+12	8.60E+11	1.24E+13	2.30E+12	4.49E+12	2.26E+12
delta	+ 1.2%	- 4.9%	+ 28.0%	+ 4.5%	+ 1.4%	- 2.2%

6.5.3 Flux-Trap Moderator Configuration

A split-target configuration permits the use of "flux-trap" moderators, which might not have to be viewed through a curved guide because the target material and the primary neutron source do not directly illuminate the beamlines. This flexibility comes at a significant penalty, as seen in Fig. 6.7, which shows the intensity from the two slab moderators as a function of the size of the front section of the target (for a constant total target thickness). In this particular flux-trap configuration, the gap between the two target sections is 24 cm wide (large enough that no beamlines view the target directly) and filled with water. The data in the figure show that, while moderator performance is relatively insensitive to the target division, the overall 1-eV and the thermal intensity parameters of the decoupled slab moderator are only about 0.25 to 0.3 those of the reference model. The thermal intensity of the coupled slab is better, between 60% and 70% that of the reference model, and shows a maximum at about 8 cm of tungsten in front of the gap. If a flux-trap moderator were to be used, the target division could be chosen to optimize the thermal intensity of the coupled moderator or another performance parameter such as the front moderator intensity or the high-energy neutron background.

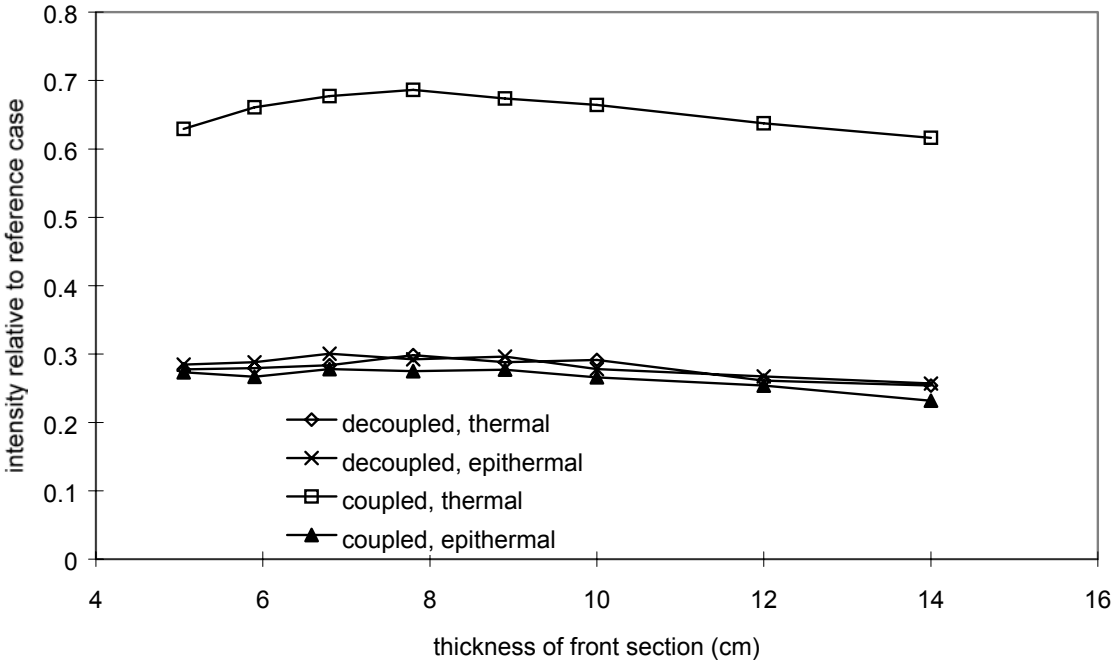

Fig. 6.7. Flux-trap moderator performance compared to reference case (24-cm water gap) vs. the size of target material on the front section.

Fig. 6.8 shows the variation in neutron beam intensity with the size of the gap (for about 5-cm target thickness in front of the gap). Any gap large enough to avoid the target illuminating the perpendicularly emerging beamlines (a minimum of 15 cm) results in a factor of 2 reduction in the epithermal intensity, while a gap large enough to avoid illuminating any beamlines (24 cm) results in a factor of 3 reduction. Similar studies using a more conventional vacuum gap have indicated a somewhat smaller penalty, of about a factor of 2 reduction. The value of the water-filled gap is seen in the improved thermalization for the coupled moderator, but this advantage is not enough to offset the initially lower epithermal intensity. Table 6.4 shows that the low-energy flux on the coupled moderator with a H_2O-filled target gap is roughly 21% lower than for a conventional split target with a vacuum gap.

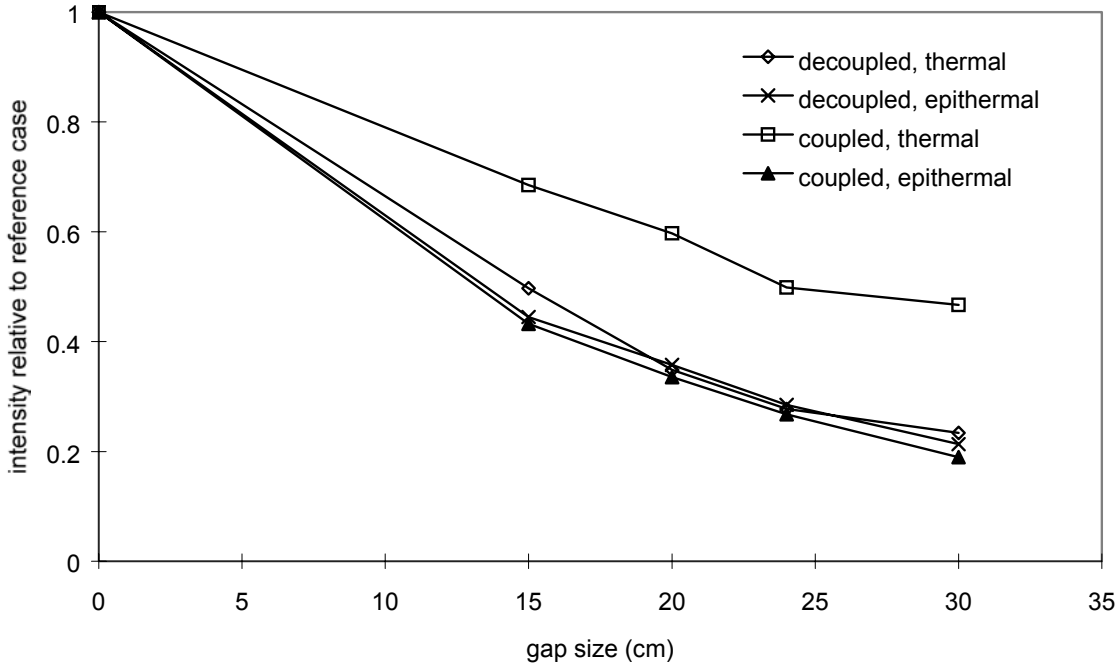

Fig. 6.8. Thermal and epithermal intensity parameters compared to reference case for flux-trap moderators (water gap) vs. gap size.

Table 6.4. Thermal and epithermal intensity for flux-trap moderators (24-cm water gap, 10-cm target upstream) compared to reference model (units are n/sr-pulse).

	Coupled Slab		**Decoupled Slab**	
	I_{th}	I_{epi}	I_{th}	I_{epi}
Reference	1.10E+13	3.84E+12	2.28E+12	2.20E+12
Water gap	7.80E+12	6.53E+11	1.16E+12	6.37E+11
Vacuum gap	9.40E+12	8.32E+11	1.63E+12	9.03E+11
Delta – water	- 29.1 %	- 83.1 %	- 49.1 %	- 71.0 %
Delta – vacuum	- 14.5 %	- 78.3 %	- 28.5 %	- 59.0 %

6.5.4 Heavy-Water vs. Light-Water Coolant

Light water is usually selected as the target coolant, but because of its superior moderating properties, moderation within the target increases losses due to thermal neutron capture in the target material. We investigated the effect of changing all the coolant in the vicinity of the target to heavy water except that between the target and the slab moderators, which serves as a premoderator. In general, the use of heavy water increases the thermal and epithermal spectral intensities by about 10% (see Table 6.5). Therefore, we adopted heavy water as the coolant for the reference configuration.

Table 6.5. Thermal and epithermal intensities for light vs. heavy water (units are n/sr-pulse).

	Front Wing (solid methane)		Coupled Slab (solid methane)		Decoupled Slab (solid methane)	
	I_{th}	I_{epi}	I_{th}	I_{epi}	I_{th}	I_{epi}
H_2O	2.85E+12	1.42E+12	1.01E+13	2.40E+12	4.50E+12	2.30E+12
D_2O	3.08E+12	1.53E+12	1.11E+13	2.62E+12	4.93E+12	2.55E+12
delta	+ 8.1 %	+ 7.8 %	+ 9.9 %	+ 9.2 %	+ 9.6 %	+ 10.9 %
	Front Wing (liquid methane)		Coupled Slab (liquid hydrogen)		Decoupled Slab (solid methane)	
	I_{th}	I_{epi}	I_{th}	I_{epi}	I_{th}	I_{epi}
H_2O	4.06E+12	1.43E+12	2.55E+13	3.54E+12	4.55E+12	2.32E+12
D_2O	4.50E+12	1.59E+12	2.66E+13	3.74E+12	4.86E+12	2.63E+12
delta	+ 10.8 %	+ 11.2 %	+ 4.3 %	+ 5.6 %	+ 6.8 %	+ 13.4 %

6.5.5 Shrunken Target

Because the peak power deposition density in the 20 × 7-cm target plates is only about 250 W/cm^3 (see Fig. 8.2), we performed a calculation in which the target and the beam profile were smaller by about a factor of 0.7 in each dimension, with the goal of increasing the peak power deposition density to about 500 W/cm^3. We saw gains in neutronic performance for all three moderators, with about 5 and 13% increases in thermal intensity for the decoupled and coupled moderators, respectively, as shown in Table 6.6. Although the higher power density is probably tolerable, for the reference case we have adopted conditions that lead to the conservative 250 W/cm^3 deposition rate.

Table 6.6. Thermal and epithermal intensities for the full-size and half-size targets (units are n/sr-pulse).

	Front Wing solid methane		Coupled Slab solid methane		Decoupled Slab solid methane	
	I_{th}	I_{epi}	I_{th}	I_{epi}	I_{th}	I_{epi}
Full size	2.85E+12	1.42E+12	1.01E+13	2.40E+12	4.50E+12	2.30E+12
Half size	3.00E+12	1.52E+12	1.15E+13	2.63E+12	4.72E+12	2.49E+12
% change	+ 5.3 %	+ 7.0 %	+ 13.9 %	+ 9.6 %	+ 4.9 %	+ 8.3 %
	liquid methane		liquid hydrogen		solid methane	
	I_{th}	I_{epi}	I_{th}	I_{epi}	I_{th}	I_{epi}
Full size	4.06E+12	1.43E+12	2.55E+13	3.54E+12	4.55E+12	2.32E+12
Half size	4.27E+12	1.50E+12	2.87E+13	3.80E+12	4.84E+12	2.46E+12
% change	+ 5.2 %	+ 4.9 %	+ 12.5 %	+ 7.3 %	+ 6.4 %	+ 6.0 %

6.5.6 Grooved Moderator

The grooved (coupled) solid methane moderator yields a broader pulse (twice the FWHM) than the flat solid methane moderators. The broader pulse is due to the grooved nature of the moderator; a flat, coupled solid methane moderator would have the same pulse width as a decoupled one for neutron energies above 0.01 eV. We carried out calculations for the grooved moderator concept shown in Fig. 6.9. The V-shaped grooves are horizontal with an opening angle of 30° on a 2-cm pitch. The groove surfaces are defined by a 2.7-mm-thick layer of aluminum that is presumed to be at the moderator temperature, with a front outer jacket of 1-cm thick half-density aluminum that represents the layers of the vacuum jacket, etc., surrounding the

moderator. The volume of moderator material in the grooved moderators is the same as in the flat moderators. The grooved moderator geometry was not optimized in terms of moderator volume or groove configuration for either of the moderator materials studied.

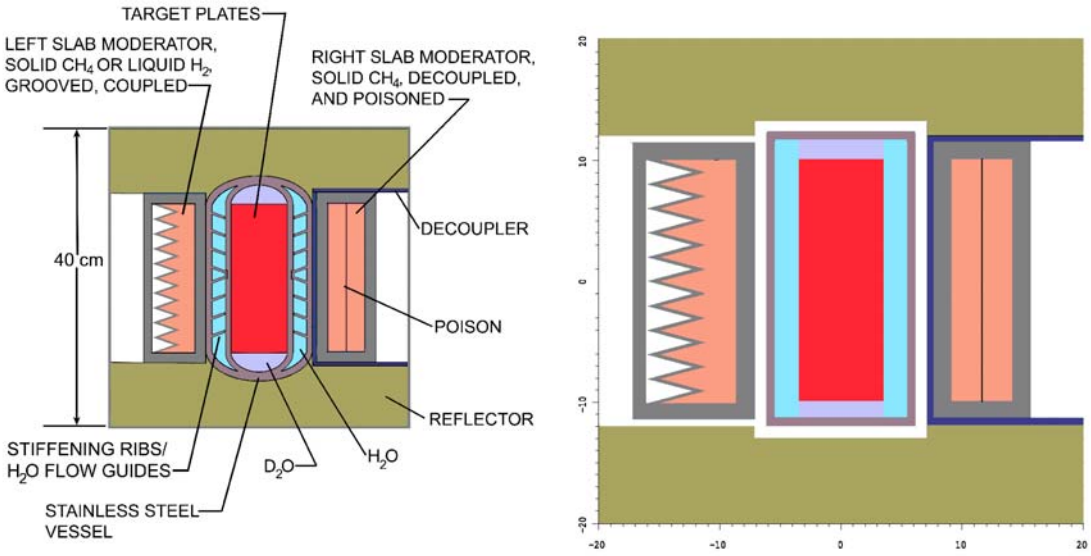

Fig. 6.9. Schematic diagram of the LWTS geometry incorporating the grooved coupled slab moderator (left) and the corresponding MCNP-X model (right).

Fig. 6.10 shows the neutron spectral intensities for the flat and grooved moderators, using both solid methane and liquid hydrogen materials, for beamlines normal to the moderator face. For the solid methane moderator material, there is a clear improvement in the performance at all energies. For liquid hydrogen, the two moderator shapes have equivalent 1-eV spectral intensities, but the grooved moderator has poorer thermal neutron intensity. We believe this is because liquid hydrogen, which has a lower hydrogen density than solid methane (about half), is optically thinner at these energies. However, an optimized moderator design for liquid hydrogen would likely yield an improvement over the flat moderator.

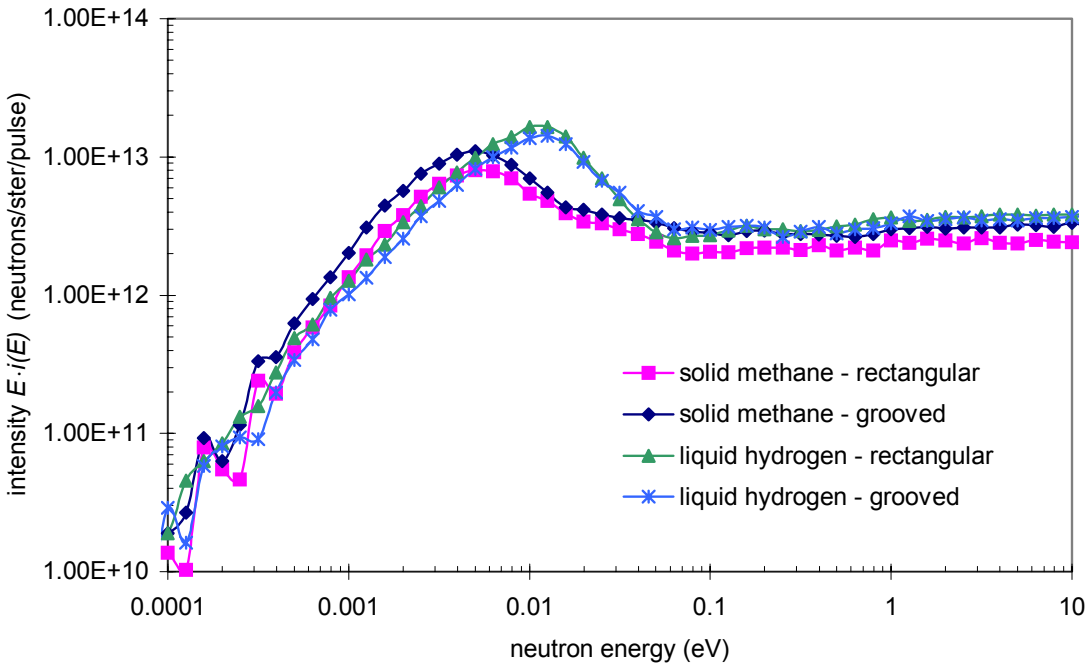

Fig. 6.10. Neutron spectral intensities for the flat and grooved coupled moderator (direction is normal to the moderator surface).

Figures 6.11 and 6.12 show the thermal and epithermal neutron intensities for the grooved moderator relative to the flat moderator at the same selected beamline angles other than the normal calculations for light- and heavy-water target coolant give similar results for both, but suggest that D_2O is favorable over H_2O in this comparison. The enhancement in thermal neutron intensity for the solid methane moderator decreases from a maximum of about 35% at the normal to the surface to about 10% for a beamline at 45° from the normal but shows an improvement at all angles. The improvement in the epithermal intensity is constant at about 20% for all directions. The liquid hydrogen moderator shows a constant epithermal intensity compared to the flat moderator but a decrease in thermal intensity of about 20% at all angles. We emphasize again that this does not represent optimized performance for either moderator.

Comparing the best performance for the solid methane (grooved) and liquid hydrogen (flat) coupled moderators, we see that liquid hydrogen provides more total neutrons and more neutrons above 5 meV. Solid methane, however, gives superior performance for a broad range of energies below 5 meV, an energy range that we believe is of great interest for instruments on the LWTS. Further optimization is required before we can select a moderator material for the coupled slab moderator, taking into account the needs of the instruments viewing this moderator.

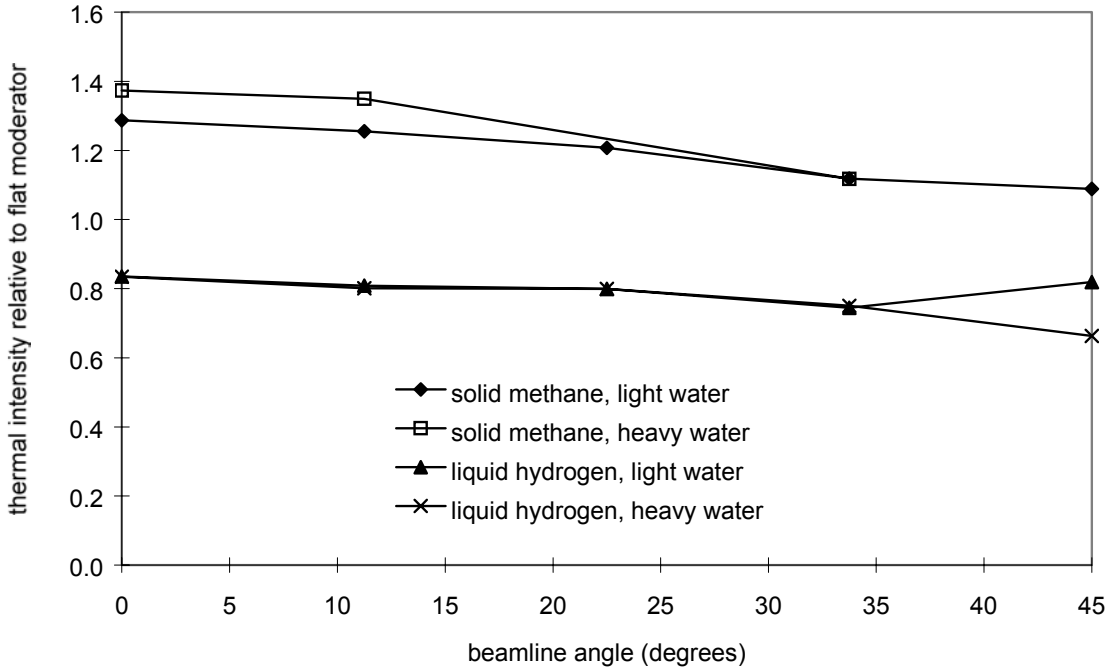

Fig. 6.11. Thermal neutron intensity of the grooved moderator relative to the flat moderator for solid methane and liquid hydrogen moderator materials in the coupled moderator position, for light- and heavy-water target coolants.

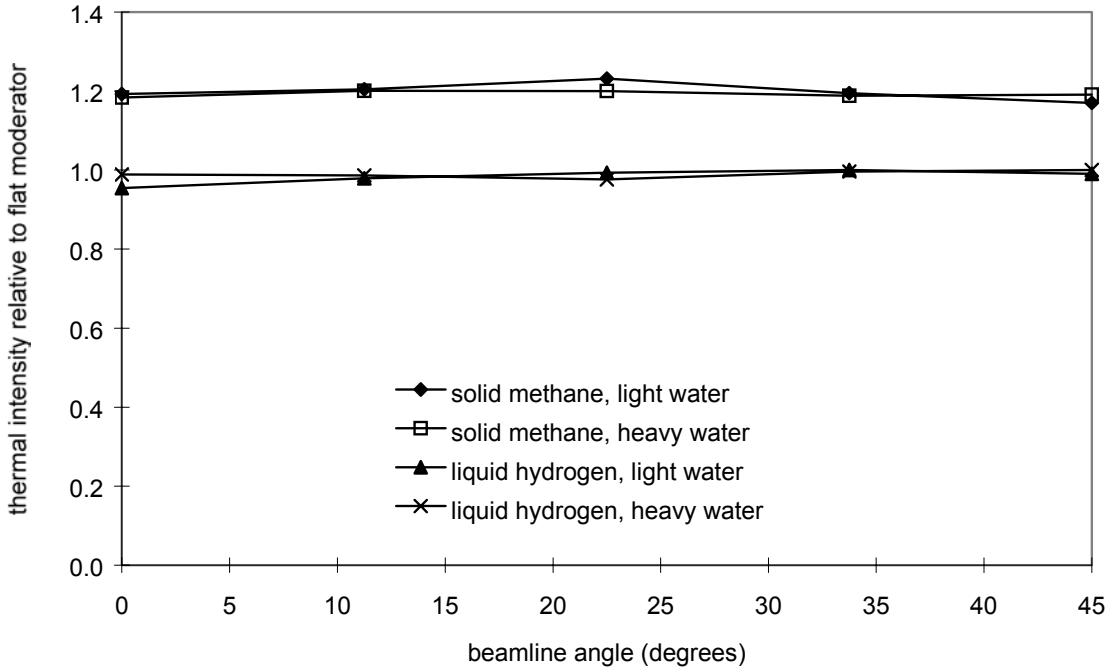

Fig. 6.12. Epithermal neutron intensity (1-eV coupling) for the grooved moderator relative to flat moderator for solid methane and liquid hydrogen moderator materials in the coupled moderator position, for light- and heavy-water target coolants.

6.6 High-Energy Neutron Source Term

One of the most significant and adventurous design features of the LWTS is the use of slab moderators, which are historically considered undesirable because of the contamination of the neutron beams with significant numbers of fast ($0.1 < E_n < 10$ MeV) and high-energy ($E_n > 10$ MeV) neutrons. Because of this contamination, beamlines should not view a slab moderator directly but need to use a curved guide, compact beam bender, T_0 chopper, or some other filter for fast and high-energy neutrons. The calculations presented here show the variation in the fast and high-energy neutron source term as a function of selected design choices.

Figure 6.13 shows the variation in spectral intensity of fast and high-energy neutrons from slab moderators as a function of the angle between the neutron and proton beam directions for the continuous (no flux-trap gap) target. This figure clearly shows that there is a "worst-case" beamline angle, around 68° from the proton beam direction, where the increased source term and reduced shielding from the target itself combine to the worst effect. The highest energy neutrons are still most problematic at the lowest angles relative to the proton beam, which is consistent with the conclusions reached in Sec. 6.3. There is an enormous difference in neutron spectra between beamlines, which may have significant implications regarding the choice of beamline for a given instrument, as some instruments will have restrictions on background and feasible shielding configurations.

Figures 6.14 through 6.16 indicate that the neutron beamline angle influences the fast-neutron component more strongly than does the presence or absence of water in the flux-trap gap and more even the size of this gap. There is relatively little neutron spectrum dependence on the size of the flux-trap gap (Fig. 6.14). Water in the flux-trap gap serves to scatter neutrons, increasing the neutron spectral intensity at energies above 10 MeV in the 70° - 110° beamlines (Fig. 6.15) while retaining the strong dependence on angle seen for the continuous target. Finally, Fig. 6.16 shows that the flux-trap 70° beamline has quantities of the highest energy neutrons ($E_n > 200$ MeV) that are equal to those of the 90° beamline for a slab moderator on the continuous target, although the fast neutron contribution is lower overall. We see that, depending on beamline angle, slab and flux-trap moderators have different energy ranges over which each displays a higher fast and high-energy neutron component. These observations represent important considerations for designing a complete target/moderator system that best suits the needs of the instrument suite to be deployed at LWTS.

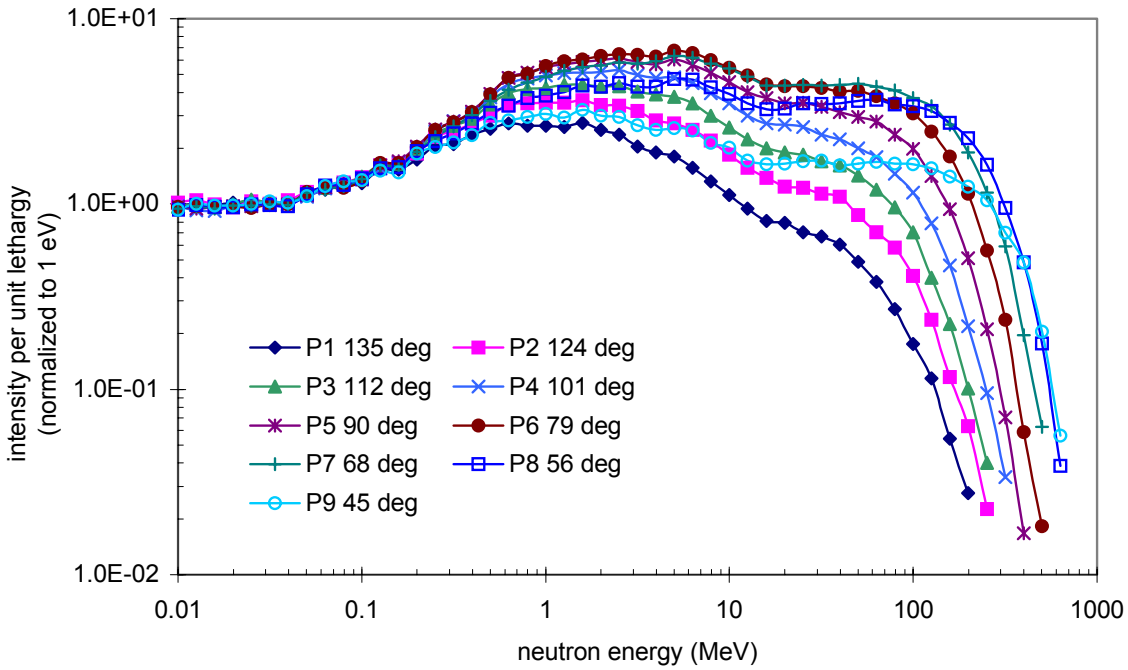

Fig. 6.13. Fast and high-energy neutron spectra from the slab moderators as a function of beamline angle with respect to the incident proton beam direction. The target is continuous (no flux-trap gap).

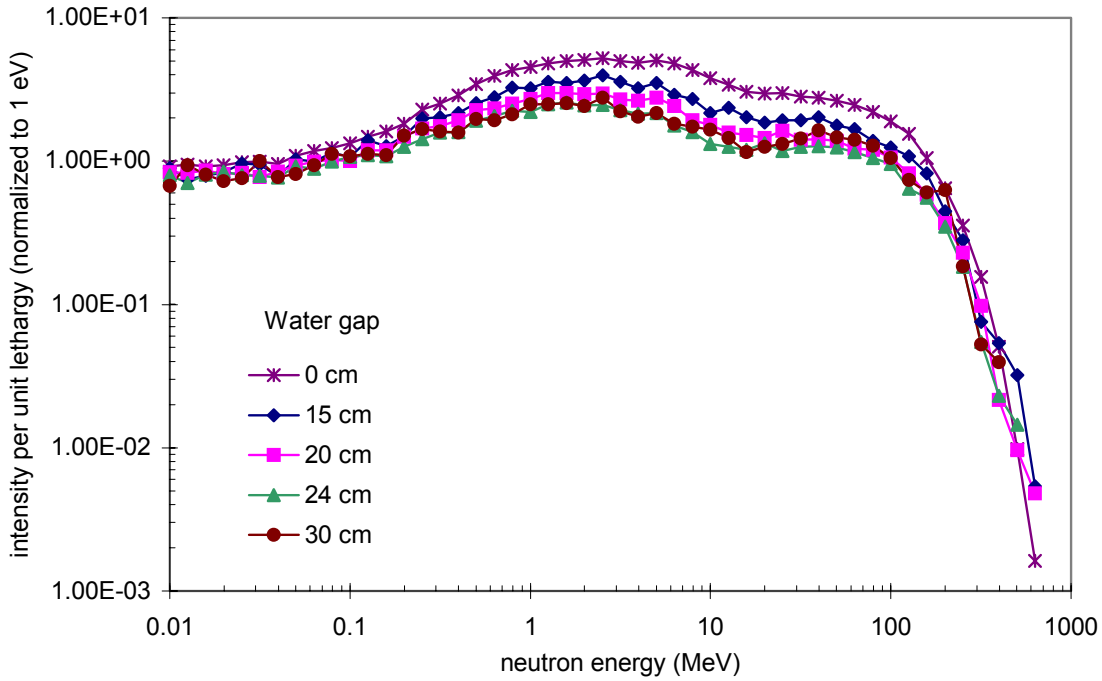

Fig. 6.14. Fast and high-energy neutron spectra as a function of split-target gap (beamline normal to moderator face). Water fills the target gap.

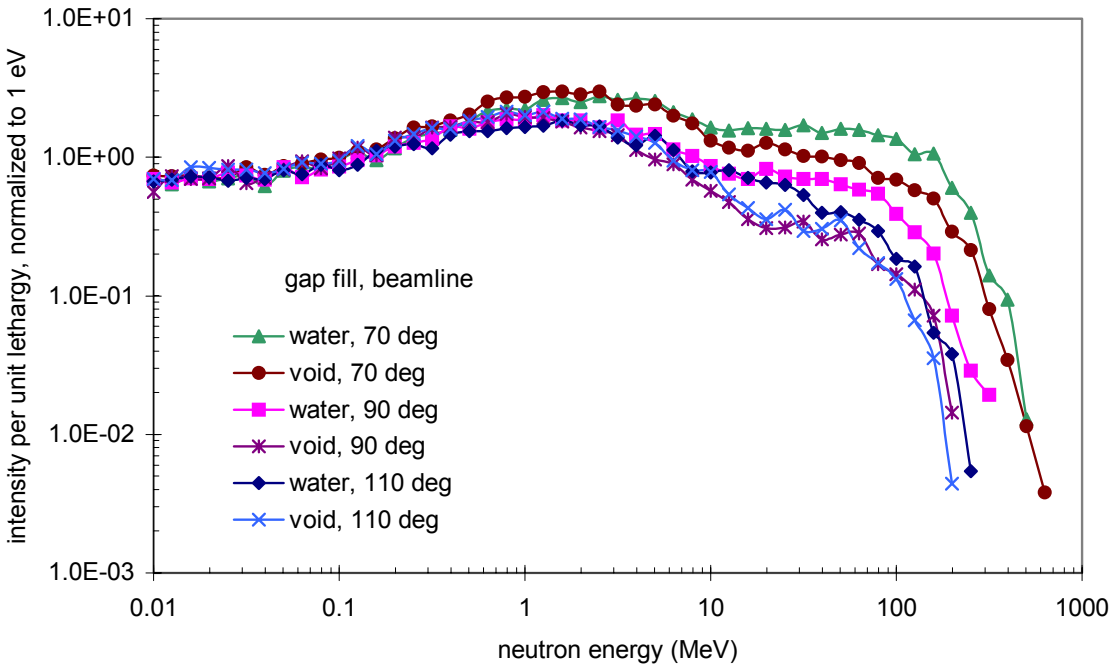

Fig. 6.15. Fast and high-energy neutron spectra as a function of split-target gap fill and beam direction. The gap is 24 cm wide.

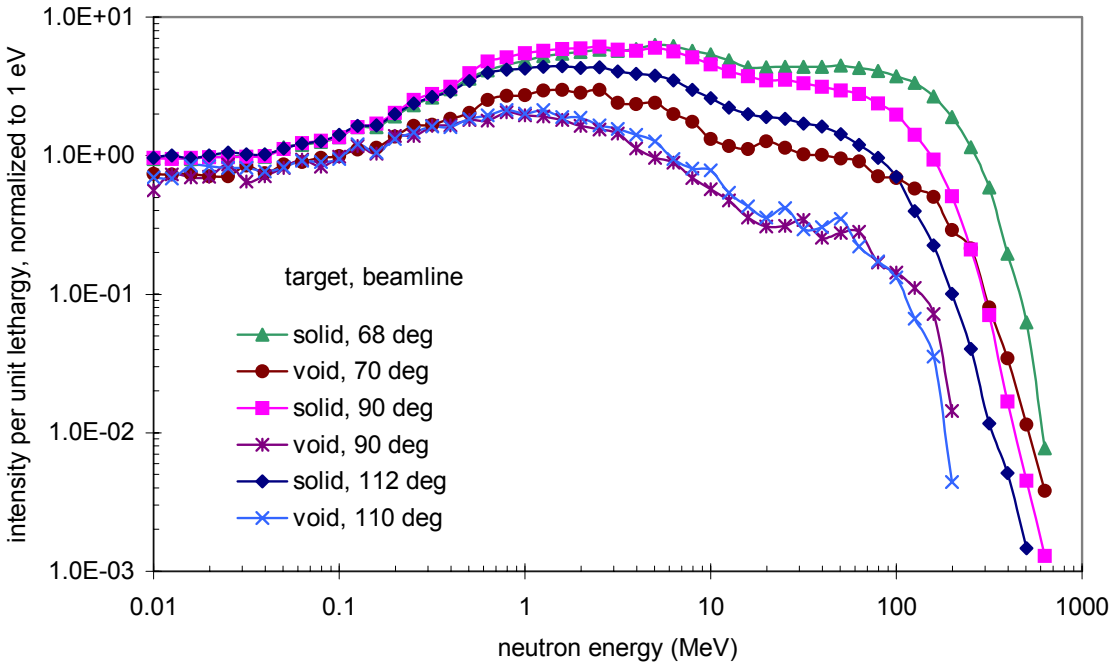

Fig. 6.16. Fast and high-energy neutron spectra for slab and flux-trap moderators. The gap is 24 cm wide.

Fig. 6.17 shows the fast and high-energy neutron spectra from the front wing moderator, with the high-energy spectrum at 90° from the proton beam direction (i.e., normal to the moderator

surface) for the slab moderator shown for comparison. As expected, the fast neutron intensity is significantly smaller for the front wing moderator, because the beamlines do not view the target directly, although there is an increase in fast neutrons for beamline angles that approach looking back toward the target.

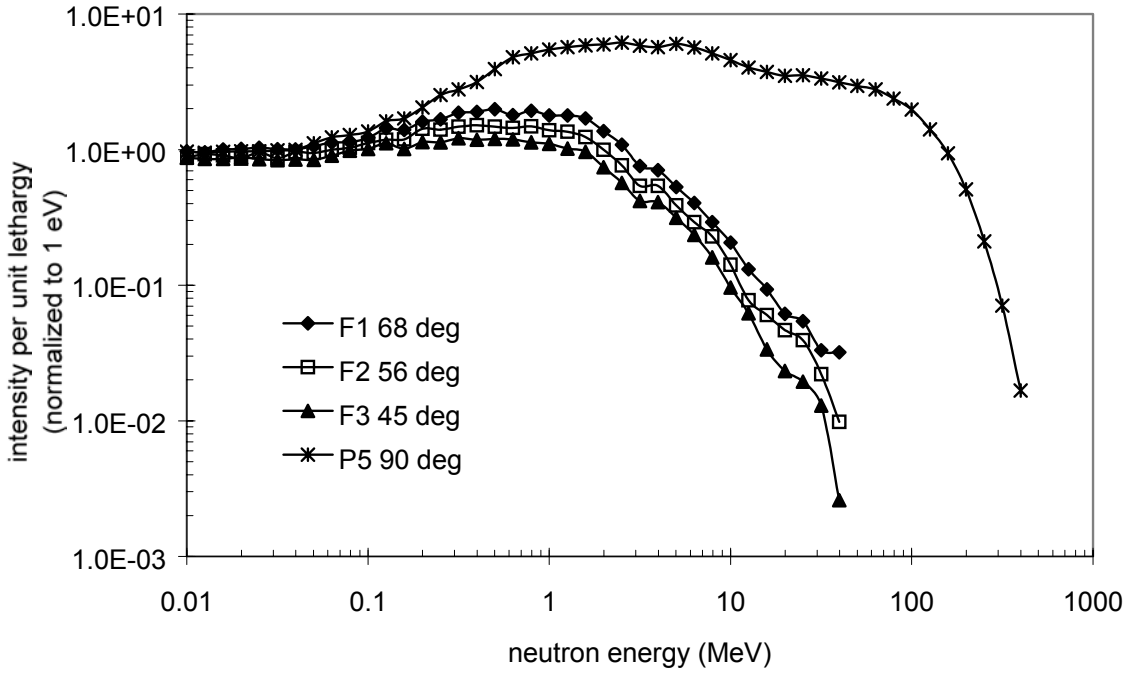

Fig. 6.17. Fast and high-energy neutron spectra from the front wing moderator as a function of beamline angle (F1, 2, 3) with respect to the incident proton beam direction. The high-energy spectrum at 90° from the slab moderator (P5) is shown for comparison.

Our results comparing the LWTS slab to the front wing moderator are roughly consistent at the highest energies ($E_n \geq 40$ MeV) with measurements carried out some time ago for the German SNQ project.[6.6.1]. Those measurements indicate approximately 300 to 1000 greater fast-neutron intensity from a slab moderator configuration than from a wing configuration, as shown in Fig. 6.18. However, the present calculations indicate substantially lower ratios for energies below 20 MeV for the LWTS slab-wing comparison than for the SNQ measurements. Measurements in the LWTS configuration will be needed to resolve this discrepancy. However, the increase in the undesirable neutron component is not significantly larger for a slab moderator than for a flux-trap moderator, which has been successfully employed at the Lujan Center. The shielding requirements are also similar to those for the HPTS beamlines when scaled according to the beam power of the LWTS. Moreover, experience and measurements at ISIS and SINQ indicate that feasible guide and bender shielding adequately controls the fast and high-energy neutron components of the beams and the background in the surroundings.

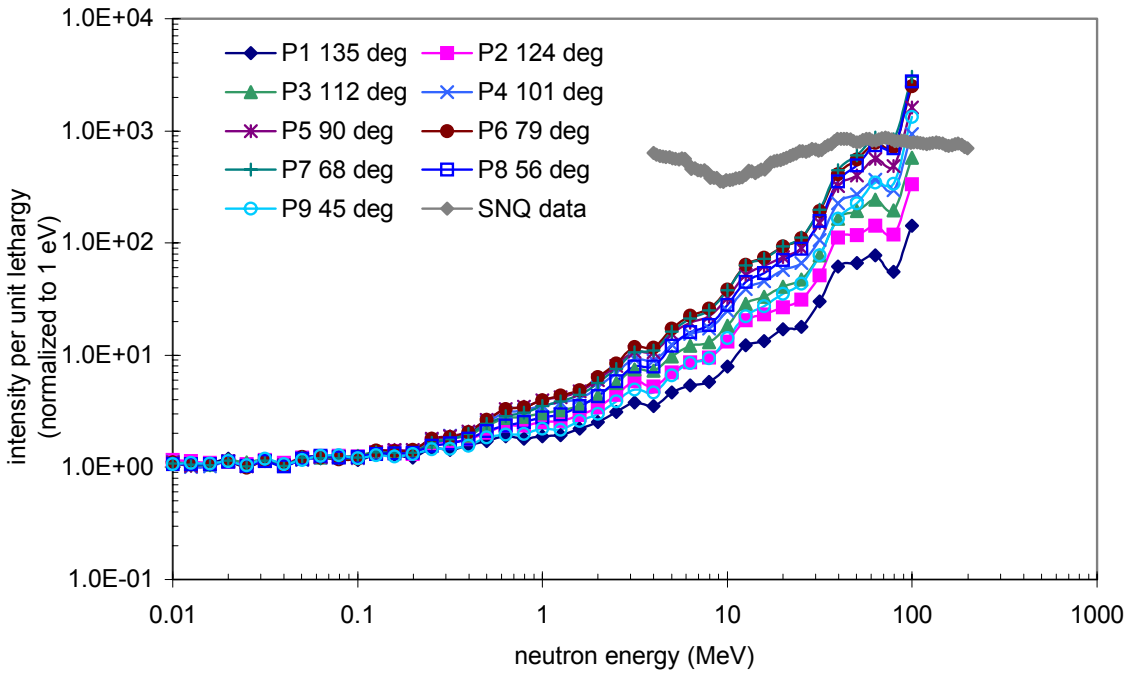

Fig. 6.18. Ratio of fast and high-energy neutrons for slab moderator beamlines relative to the normally-emerging front wing beam (all normalized to their values at 1 eV). Experimental data from SNQ (ratio slab/wing) [6.6.1] are shown for comparison.

6.7 Activation and Afterheat

Nuclear activation of the neutron-producing target determines the afterheat that must be removed from the target in any accident involving a loss of coolant. Usually, the afterheat is estimated by calculating radionuclide production rates using a code such as MCNPX and using these rates as input to a buildup and decay code such as ORIGEN. Rather than conduct detailed target activation studies, which were beyond the limited scope of the LWTS study, we reviewed activation and afterheat calculations from both the IPNS-Upgrade study [6.7.1] and the SNS HPTS solid target backup study [6.7.2] to determine the afterheat that would result from a tungsten target at the 333-kW proton beam power proposed for the LWTS. The comparison of these results reveals some pitfalls that can await one who is not careful regarding the details of the physical vs. the computational model.

We found significant differences between the results of the two studies for constant beam power. The SNS results for afterheat were approximately a factor of 2 higher for a tantalum target and a factor of 4 higher for a tungsten target than the corresponding values from the IPNS-Upgrade study. Examination of the buildup (see Fig. 6.19) and decay rates for the afterheat indicated that the principal nuclides were the same in the two studies. For example, for the tungsten target the afterheat at shutdown for both studies increases an asymptote as a function of operating time with a half-life of about 24 hours, which indicates ^{187}W as the primary radionuclide responsible for afterheat. Afterheat decay after shutdown shows the same principal half-life. Similarly, in the tantalum target afterheat at shutdown increases and subsequently decays with a characteristic half-life of about 114 days, corresponding to ^{182}Ta.

Since the asymptotic values of the curves are different, however, it is obvious that the creation rates calculated in the two studies were different.

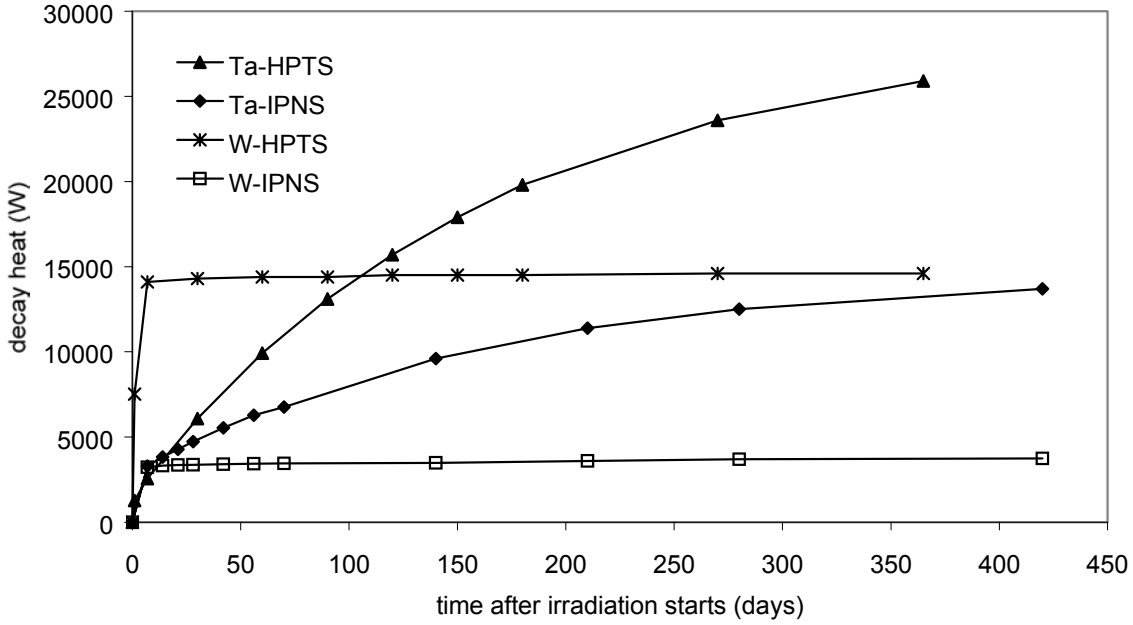

Fig. 6.19. Target decay heat at shutdown for IPNS-Upgrade and HPTS solid backup target studies.

A more detailed examination of the model used for the IPNS-Upgrade activation calculations showed that the model did not contain coolant in the target region (and thus did not accurately account for neutron thermalization in the target). Furthermore, because the model did not contain water, neutron transport had not been carried out below 1 eV, thus completely neglecting radionuclide production caused by thermal neutrons (which is the primary production mechanism for the dominant radionuclides).

To understand these discrepancies and to test the sensitivity of radionuclide production to the presence of water in the model, we carried out some simple calculations of neutron activation rates in tungsten and tantalum targets using the LWTS target model (we included tantalum because it has only one natural stable isotope, thus simplifying analysis of the results). Comparing the results from the LWTS target (assuming H_2O coolant) with those obtained by counting activation caused only by neutrons above 1 eV in a water-free target, we found that the production of the dominant radionuclide was underpredicted by a factor of 3.23 in the tungsten target and 1.63 in the tantalum target (see Table 6.7). Without the water present around the target, production is increased due to neutrons above 1 MeV and decreased below 1 MeV due to the lack of moderation. It is interesting to note, as a result of these calculations, that although we usually regard a spallation target as an energetic-particle system, thermal-neutron capture is the dominant mechanism for generating radionuclides responsible for long-term afterheat.

Table 6.7. (n,γ) production rates in H_2O-cooled Ta and W targets (product nuclei per incident proton)

Target Material	Reaction (half-life)	Neutron	Energy	Range	
		< 1 eV	1 eV - 1 MeV	1 MeV - 20 MeV	Total
Ta (H_2O)	$^{181}Ta(n,\gamma)^{182}Ta$ (114.43 d)	1.954	5.355	0.195	7.504
Ta (no H_2O)		(1.323)*	4.383	0.210	4.593
W (H_2O)	$^{186}W(n,\gamma)^{186}W$ (23.9 h)	1.449	1.061	0.024	2.534
W (no H_2O)		(0.892)*	0.759	0.026	0.785

*production for E_n < 1 eV not included in total for target with no H_2O

Because the afterheat modeling that was carried out for the IPNS-Upgrade study did not result in accurate afterheat values, for the LWTS we chose to adopt the values calculated for the D_2O-cooled HPTS solid-target for afterheat per unit of incident proton beam power. Accordingly, the afterheat for the 333-kW, D_2O -cooled LWTS target would be approximately 1.33 times that cited at the time for the 1-MW, IPNS-Upgrade target. Because we concluded in the IPNS-Upgrade study that the target, vessel, and reflector would not melt in a loss of coolant accident (LOCA), and that the consequences of such an accident were tolerable, the same is likely also to hold true for the LWTS. In any event, the H_2O premoderator layer on the target sides serves as an independent cooling system in the event of a primary coolant LOCA.

6.8 Summary of LWTS Moderator Performance Parameters

Table 6.8 summarizes performance parameters of LWTS moderators, alluding to options described in the preceding sections.

Table 6.8. LWTS moderator performance parameters.

Moderator	Material	I_{Th}, n/sr/pulse	E_{Th}, meV	I_{epi}, n/sr/pulse	Δt_{FWHM}, μsec 2.0 meV	10.0 meV	$v\Delta t_{FWHM}$, mm 1.0 eV
High-resolution cold moderator: decoupled slab	L-H_2–cooled S-CH_4 @ 20 K	4.9×10^{12}	2.53	2.6×10^{12}	71.0	18.0	26.0
High-intensity cold moderator: coupled slab, grooved	Option I: L-H_2 @ 20 K	2.2×10^{13}	5.61	3.7×10^{12}	160.0	63.0	84.0
"	Option II: L-H_2–cooled S-CH_4 @ 20 K	1.6×10^{13}	2.25	3.0×10^{12}	200.0	48.0	54.0
High-resolution broadband moderator: decoupled front wing	Option I: L-CH_4 @ 100 K	4.5×10^{12}	9.78	1.6×10^{12}	45.0	40.0	29.0
"	Option II: L-H_2–cooled S-CH_4 @ 20 K	3.1×10^{12}	2.54	1.5×10^{12}	71.0	19.0	28.0

6.9 References

6.1.1 L.S. Waters, Ed., "MCNP-X User's Manual, Version 2.1.5," Report TPO-E83-UG-X-00001 (Nov. 14, 1999).

6.1.2 R.E. Prael and H. Lichtenstein, "User Guide to LCS: The LAHET Code System," Los Alamos National Laboratory Report LA-UR-89-3014, Revised (Sep. 15, 1989).

6.1.3 J.F. Briesemeister, Ed., "MCNP — A General Monte Carlo N-Particle Transport Code," Los Alamos National Laboratory Report LA-12625-M, Version 4B (Mar. 1997).

6.6.1 G.S. Bauer, H. Sebening, J.-E. Vetter, and H. Willax, "Realisierungstudie zur Spallations-Neutronenquelle," technical report, Arbeitsgemeinschaft Spallations-Neutronenquelle (1981).

6.7.1 "IPNS Upgrade: A Feasibility Study," Argonne National Laboratory Report ANL-95/13 (Apr. 1995).

6.7.2 S.J. Pawel, "Preliminary Materials Recommendation for a Solid Target Back-Up for the SNS," SNS/TSR-0149 (Oct. 29, 1999).

7. ENGINEERING ANALYSIS

7.1 Target Thermal Hydraulics

A major challenge in spallation target design is the removal of heat from the target. Pulsed spallation neutron source targets operated to date — IPNS, KENS (the 5-kW pulsed spallation source at KEK), ISIS, MLNSC (the 80-kW source at LANL) have employed a plate design, with plates of target material oriented perpendicular to the proton beam and separated by narrow coolant channels. Water (heavy water at ISIS) is the coolant in all such systems operated so far. This technology is well developed and understood, is well suited to the LWTS power level, and is the reference design for the LWTS target.

In this chapter we discuss engineering analyses carried out during the LWTS study. The study terminated before all the relevant work was complete, leaving some significant omissions. We reason, on the basis of earlier studies, that these do not represent problems.

The power density distributions obtained from the LWTS neutronics analyses (Sec. 6) serve as inputs to the thermal-hydraulic analyses of the LWTS target plates and vessel. Plate thicknesses and coolant flow velocities are adjusted to provide single-phase flow in the upstream target plates and controlled center temperatures in the downstream plates. The thicknesses and shape of the stainless steel window portion of the target vessel, which heats in a fashion similar to that of the target, but is cooled on only one surface, are adjusted to control the stresses in the window.

The power densities of the LWTS vessel and target disks are lower than in the similar IPNS 1-MW target study [7.1.1] and the SNS backup solid target study [7.1.2]. All stresses are within tolerable limits for the IPNS 1-MW target and SNS solid target studies, so stresses are expected to be within acceptable limits for the LWTS target. The spring-loaded design accommodates thermal expansion of the target disks, as in the IPNS target and plans for the SNS backup solid target.

The spatial energy deposition followed as part of the neutronic analyses of the LWTS target-moderator-reflector assembly. The analyses assumed a shape similar to the rather flat proton beam profile of the HPTS (Sec. 6.1) as shown in Fig. 7.1.

Figure 7.2 shows the energy deposition rate along the target centerline for the reference LWTS proton beam power of 333 kW. The peak energy deposition is about 253 W/cm^3 and occurs in the second target plate. The energy deposition falls rapidly as the proton beam is depleted due to nuclear interactions, but a small Bragg peak can still be seen at the end of the proton beam range (about 30 cm for 1 GeV incident energy). Approximately 62% of the incident beam power appears as heat in the target plates and coolant.

The second target plate from the front of the target (for tungsten plates) has (a) the highest overall plate power density per unit volume and (b) the highest energy deposition per proton and power per cm^2 in any analytical model element. Figure 7.3 shows the distribution of energy and power deposition in plate 2.

Table 7.1 lists LWTS target plate total power, average, and maximum power densities for a 333-kW proton beam power. The target plates increase in thickness from the front to the back of the target, which keeps the total plate powers (and thus the surface heat flux) relatively constant while the average and maximum power densities drop markedly toward the back of the target.

Table 7.1. Total, average, and maximum heating rates for each target plate.

Target Plate	Total	Average	Centerline
	(kW)	(W/cm^3)	(W/cm^3)
Plate 1	30.8	113	252
Plate 2	33.4	113	253
Plate 3	32.8	112	248
Plate 4	31.9	108	242
Plate 5	33.0	105	233
Plate 6	31.4	99.6	219
Plate 7	31.7	94.4	207
Plate 8	31.6	88.4	193
Plate 9	31.3	82.7	180
Plate 10	32.1	76.2	164
Plate 11	31.9	69.0	144
Plate 12	29.0	62.8	130
Plate 13	45.4	54.0	108
Plate 14	37.1	44.1	87.2
Plate 15	36.6	34.8	65.1
Plate 16	32.5	25.8	45.8
Plate 17	23.3	18.5	32.0
Plate 18	21.7	12.9	20.4
Plate 19	17.1	9.03	10.2
Plate 20	21.0	1.11	7.16
Plate 21	13.9	0.737	5.48

The maximum power and maximum thermal energy density per pulse in the spallation target plates and the proton beam window in the target vessel are good indicators of the severity of difficulties in the design of a target in terms of operating heat removal, stresses, shock, lifetimes, LOCA temperatures, etc. The energy and power depositions in the LWTS target are low, so a detailed target analysis and an acceptable design should not be difficult to achieve.

With 333-kW time average proton beam power (2.08×10^{15} proton/sec) distributed on the target as in Fig. 7.1, the maximum thermal power density is 253 W/cm^3. The designs of the similar IPNS 1-MW target study and the SNS solid backup target study at 1 MW, for tungsten, have expected maximum power densities of 1650 and 540 W/cm^3, respectively. The operating heat removal and target plate stresses were found to be acceptable in these studies; therefore, they should be acceptable for the LWTS with its lower power densities.

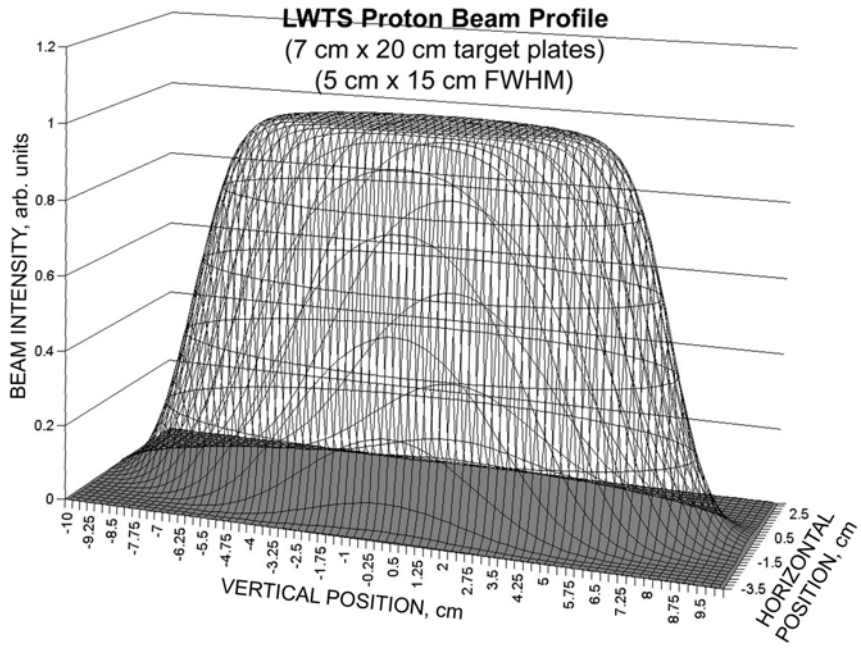

Fig. 7.1. The LWTS proton beam profile.

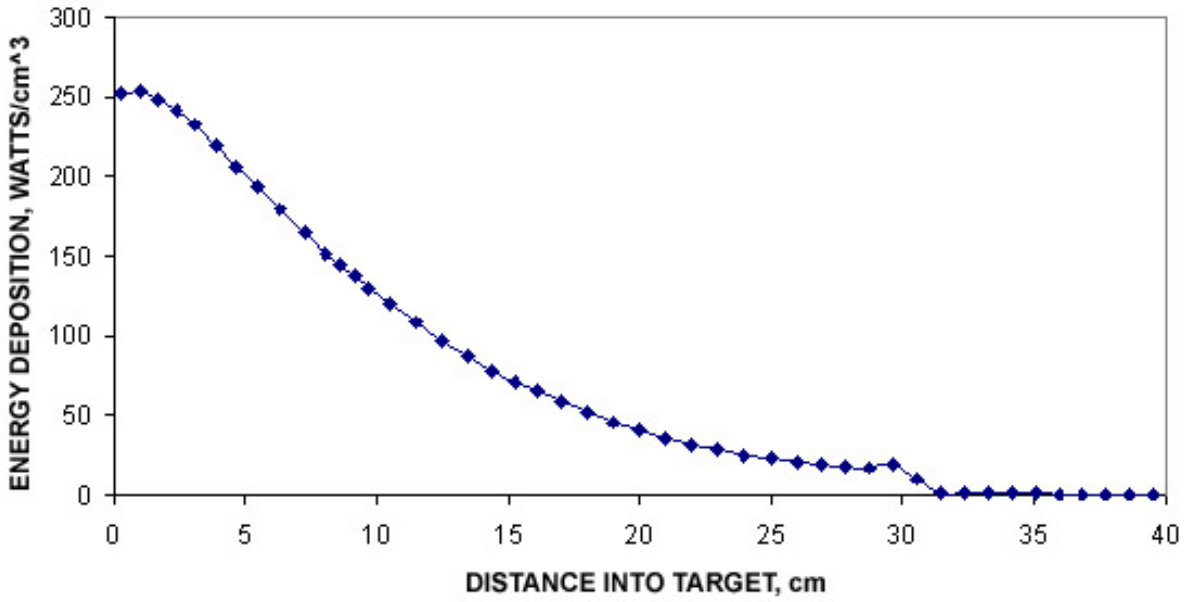

Fig. 7.2. Thermal power density along the LWTS target centerline.

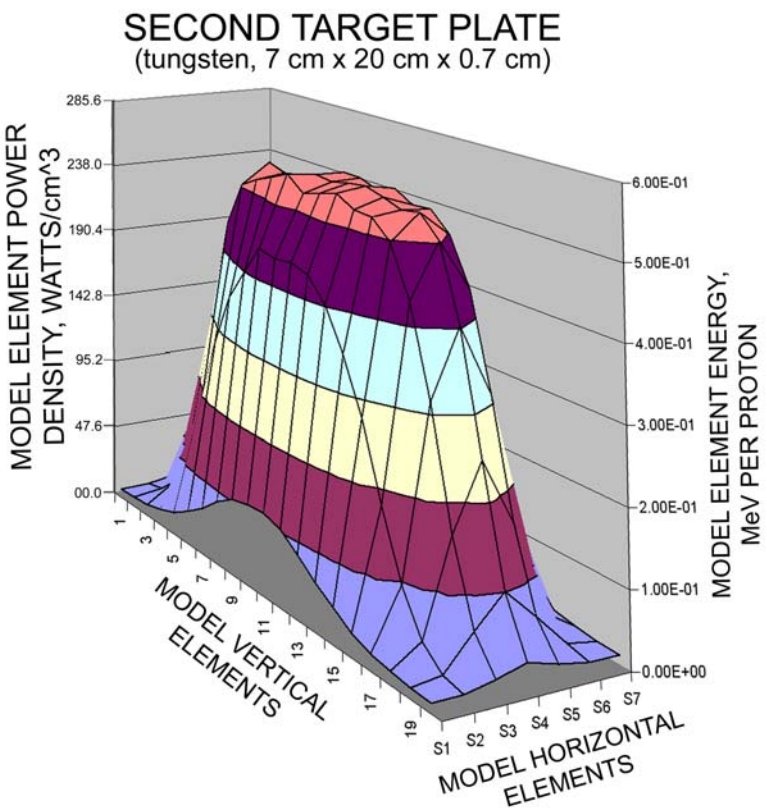

Fig. 7.3. Thermal power density and thermal energy deposition in the second target plate of the LWTS. The volume of each model element is 0.7 cm^3. The power density corresponds to 2.08×10^{15} protons incident on the target, distributed as in Fig. 7.1.

7.2 Moderator Energy Deposition

Moderators absorb heat and suffer radiation damage from the nuclear radiations (principally fast neutrons) in their environment. The LWTS design includes H_2O premoderators that reduce cryogenic cooling requirements and radiation damage rates in the moderator media. The Japanese (Watanabe, Teshigawara, Kiyanagi, and others) are conducting extensive programs aimed at optimizating premoderator systems; as these results become available, we will use the data in our detailed design. A 20-mm-thick H_2O premoderator layer in the target vessel wall separates the slab moderators from the target plates in the LWTS base-case configuration (Fig. 2.2, 2.3, 2.4). Some of this H_2O premoderator layer also lies between the target plates and the front wing moderator.

The modeled LWTS moderator containers contain low-density (10 vol%) foam aluminum to assist in removing heat from the moderator material and conducting it to cooled container surfaces. Such a system works in IPNS, as does a comparable arrangement in KENS.

Our base-case design includes a moving solid methane moderator concept (Fig. 1.2) for both slab moderators, in which one moderator in three is in the service position (and cooled). The moderator moves vertically, with accompanying reflector pieces, to its annealing position, then into a chilling position, and finally returns to the service position. The Jülich-based ACoM is

addressing the engineering aspects of high-power liquid hydrogen-cooled, pelletized solid methane systems. We have participated in these developments, which may prove useful in designing the LWTS. Developments of liquid hydrogen-cooled, pelletized solid methane and solid ammonia moderators taking place at CAF Inc. (at Oak Ridge, Tenn.) point to a successful method for cooling the cryogenic moderator medium at LWTS power.

The modeled systems are fairly realistic for neutronic purposes because the proton density in the L-H_2–pelletized methane is very close to that in the aluminum-foam-diluted solid methane that is the basis for LWTS neutronic performance calculations.

The front wing moderator is of liquid methane. In some of the cases computed, the coupled slab moderator consists of liquid hydrogen in a nonmoving moderator assembly.

Table 7.2 summarizes the heating rates in each moderator where all moderators are assumed to be solid methane. The volumes of the three moderators are $20 \times 12 \times 5$ cm^3. The total powers in the moderators are as follows: front wing, 870 watts; left slab, 1275 watts; and right slab, 1868 watts. These total powers are similar to those in the IPNS 1-MW target study, where the moderator total powers ranged from 780 to 1580 watts. Heat removal from the LWTS moderators is expected to be realizable.

Table 7.2. Heating rates in watts for various moderator components.

	Moderator + Poison	Jacket	Decoupler	Total
Front wing	361	355	154	870
Left slab	762	513	-	1275
Right slab	871	754	243	1868

Table 7.3 lists the heating rates in watts by segments in each moderator where all moderators were assumed in the calculations to be solid methane. The segments are ordered from nearest (to the target) to farthest for each moderator in the direction of the nominal neutron beam direction in the slab moderators, transverse to the direction of the nominal neutron beam direction in the wing moderator. The segments are 0.5 cm thick for the slab moderators and 1 cm thick for the wing moderator

Table 7.3. Heating rates in watts for various moderator segments.

Segment	Front Wing	Left Slab	Right Slab
1	52.3	107.1	113.5
2	45.3	98.9	105.8
3	39.7	90.9	98.7
4	35.1	83.6	93.1
5	31.3	70.6	83.0
6	28.1	77.7	93.6
7	25.5	65.5	75.5
8	23.1	60.3	68.9
9	21.2	55.5	63.3
10	19.5	52.1	59.8
11	17.9		
12	16.8		

7.3 Thermal Shock in Target

We carried out a series of analytical calculations to provide estimates of the maximum temperature and corresponding stress wave amplitude in the LWTS tungsten target plates by using the calculated energy deposition distribution for the LWTS. The results of the calculations show that maximum stresses in the target material are less than about 1/50 of the tensile yield strength for tungsten.

Members of the LWTS design team took part in SNS-motivated thermal-shock strain measurements on various target materials at the LANL Weapons Neutron Research (WNR) facility. Figure 7.4 represents raw unprocessed strain data for a solid tungsten disk subjected to an 800-MeV proton beam pulse having a duration of 300 nsec. The strain gage was located 3.2 cm from the center of the .063-cm-thick, 7.62-cm-diameter disk and oriented to respond to radial strain. The figure shows a maximum relative strain amplitude of approximately 10×10^{-6}. Preliminary experimental results show that the tungsten target should easily withstand the measured strain. These data are not yet fully processed, and final analyses may show additional contributions due to higher frequency components.

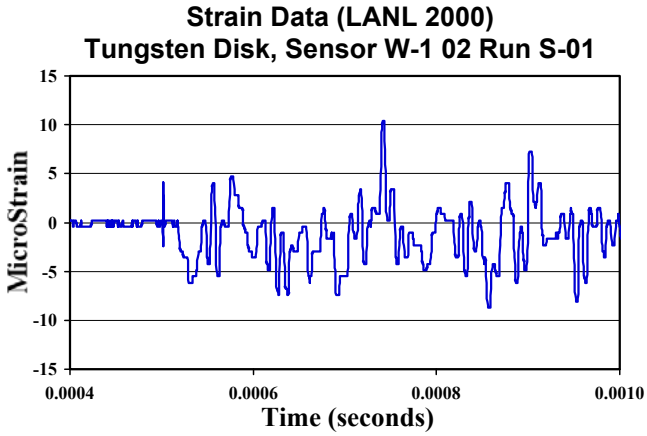

Fig. 7.4. Measured strain in a tungsten plate. The driving proton pulse occurs at about 0.0005 sec.

7.4 Loss-of-Coolant Analyses

Calculations of the transient temperatures under LOCA conditions provided an assessment of the consequences of a LOCA for the IPNS 1-MW target [5]. With a tungsten target and the decay heat data available for that study, a LOCA would have no impact on the facility as a whole even for 1-MW operation, but the target would have to be replaced. This is a tolerable consequence of a hypothetical LOCA. In the context of that study, tantalum was thought to be unacceptable because calculations had indicated higher decay heat powers than in tungsten.

Recent decay heat analyses (Sec. 6.7) for tungsten and tantalum show they have similar saturation magnitudes but different temporal behaviors; i. e., tungsten activates and decays more quickly than tantalum. Because (a) the LWTS target operates at 1/3 the power of the IPNS 1-MW target, (b) the latest tungsten and tantalum decay heat values are less than four times higher than those used for the IPNS 1-MW target, and (c) the LWTS target is larger, it is possible that both materials are acceptable for the LWTS target plates without the need for a backup

decay heat removal system. This result slightly favors tantalum as the target plate material. The decay heat behaviors of the materials will receive further investigation. While passive LOCA mitigation is desired, the benefits of using the vessel wall cooling system for LOCA mitigation as a required active backup cooling system will be evaluated.

7.5 Engineering R&D Activities

Numerous engineering and materials issues have arisen during concept development that require more information than is now available to provide a basis for a detailed design and for potential design innovations. Literature and experience searches and/or an R&D testing program can address the following issues in support of the current reference design target (forced-convection-cooled target plates in a vessel). At this time, they represent areas that need better documentation before the engineering design is complete.

1. Assess thermal shock stress in the proton beam window and target plates. We will track progress in the ASTE testing program at BNL. This collaboration is already under way for this and other purposes.

2. Assess the effects of realizable proton beam footprints in terms of neutron production efficiency and minimizing target and target window stresses.

3. Assess tantalum and various high-tungsten target alloys and cladding materials for fabricability, clad/plate integrity, clad corrosion resistance, embrittlement, cyclic operation damage, radiation damage, radionuclide buildup, and radiation-induced growth.

4. Assess proton beam vacuum window and the vessel proton beam window materials/thicknesses for embrittlement, cyclic operation damage, and radiation damage.

5. Assess LOCA consequences and the need for independent and active afterheat removal systems.

7.6 References

7.1.1 "IPNS Upgrade: A Feasibility Study," ANL-95/13, Argonne National Laboratory, 9700 S. Cass Ave., Argonne, IL 60439-4801, Work sponsored by U.S. Dept. of Energy, Office of Energy Research, Dist. Cat. General Energy Research (UC-400) (Apr. 1995).

7.1.2 D.A. Everitt and S. Chae, "Design of a Solid Target Backup for the SNS," SNS-101050600-TR00001-R01, SNS-TSR-182-rev. 1 (Mar. 28, 2001).

8. SCIENTIFIC JUSTIFICATION

The LWTS will greatly impact a number of areas of science. These typically involve structures and interactions that span relatively large distances or vary greatly in length (10–10,000 Å) and processes that occur over a large range of timescale, 10^{-7} to 10^{-13} sec. The discussions of applications are the results of more than a half-dozen workshops held since early 2000, which involved dozens of scientists drawn from universities and other laboratories working in the subject fields. Workshops dealt with soft matter; disordered materials; magnetism; powder diffraction; biological materials; fundamental neutron physics; and chemical spectroscopy, protein folding dynamics, and polymer dynamics. The workshop activities were carried out with NSF support and formed the basis for development of concepts for the LWTS facility and its instrumentation.

Two criteria form the basis for selection of LWTS instruments. First, the instruments must serve the needs of the scientific community that uses neutron scattering techniques, either by providing improved capabilities where the benefits are known or by expanding the capabilities of neutron scattering to probe phenomena on broader scales of length, energy, and time. Second, the instruments must require the large bandwidth and high cold-neutron brightness provided by the LWTS that is not available at other neutron sources. In this way, the LWTS instruments augment the range and performance of existing and proposed instruments at other neutron sources and either allow for rapid, broadband measurements on evolving sample systems or allow entirely new classes of experiments. Table 8.1 summarizes the importance of the proposed instruments and beamlines for the subject fields addressed in the workshops.

Table 8.1. Importance of proposed LWTS instruments to key areas of science (more asterisks indicate greater importance).

	Soft Matter	Disordered Materials	Magnetism	Powder Diffraction	Biology	Fundamental Physics
Broad Range Intense Multipurpose SANS	***	**	*		***	
200-neV Backscattering Spectrometer	***	**			***	
Magnetism Diffractometer			***	**		
Broad Band Reflectometer	***				***	
Grazing Incidence SANS Reflectometer	***	**			***	
Neutron Spin Echo Spectrometer	***	***	*		**	
Polarized Reflectometer			***			
Ultra-Cold Neutron Station						***
High-Resolution Chopper Spectrometer	*	***	*		*	
High-Resolution Powder Diffractometer			***	***		
Protein Diffractometer	*			**	***	

8.1 Soft Condensed Matter

8.1.1 Introduction

Soft matter is generally based on macromolecules, both nonbiological and biological (or biologically inspired), and their interactions in mixtures with other macromolecules, solvents, and non soft materials. These interactions provide for an enormous richness of structural phases and complexity [8.1.1, 8.1.2]. The structural phases are either disordered or ordered to varying degrees in one, two, or three dimensions, and they sometimes can be systematically tailored to control the ordering and the resultant macroscopic material properties. Thus, soft matter forms a major component of complex materials, with biomolecular materials as a subset. The relatively long length scales involved, coupled with the large number of both intramolecular and intermolecular degrees of freedom, distinguish soft matter from hard "atom-based" materials, that is, those that we understand in terms of interatomic interactions and structural units consisting of small numbers of atoms. The structural complexity exhibited by soft matter includes local bonded and nonbonded interactions in the length range of 0.1 nm to long range ordering at 100 nm and greater. The dynamics of these materials vary from the very short timescales of intramolecular vibrational motions to the very long timescales of slow diffusive motions.

8.1.2 Opportunities for Neutron Scattering in the Study of Soft Matter

The significant difference in scattering cross sections between hydrogen and deuterium, (^{1}H and ^{2}H), coupled with the large amounts of hydrogen present in soft materials, allows for studies with a high degree of sensitivity to structural detail in soft matter systems. Researchers can use contrast variation and/or selective labeling by isotopic substitution of hydrogen to examine the structural detail of soft matter. Because of the large penetration depth of neutrons, scientists can conduct structural investigations of complex systems under confinement or in extreme environments at conditions that are either at or far from equilibrium. The relationship between energy and wave vector implied by the neutron mass and the large incoherent cross section for ^{1}H versus ^{2}H allows for a high sensitivity via inelastic and quasielastic scattering to selected intramolecular and intermolecular dynamics over a wide range of timescales [8.1.3–8.1.5]. Both the long length scales and slow motions of soft complex systems are best explored by means of the elastic/inelastic scattering of long-wavelength (i.e., cold) neutrons.

Pulsed neutron sources are ideal for kinetic studies of structure evolution in soft materials because of both the large bandwidth and the high peak flux per pulse. The spectrometers proposed for the LWTS will provide unsurpassed opportunities for studying these materials. For structural characterization of soft matter, the following instruments will provide unparalleled capabilities: the broad-range intense SANS instrument (BRIMS; Sec. 4.1), the broadband reflectometer (Sec. 4.4), the grazing-incidence SANS instrument (GISANS; Sec. 4.5). For the study of long-timescale dynamic processes typically found in soft matter, the 200-neV crystal analyzer spectrometer (Sec. 4.2) and the spin echo spectrometer (Sec. 4.6) will provide more capabilities than HPTS instrumentation. The 200-neV instrument offers 10 times better resolution then the backscattering instrument on the HPTS; the spin echo machine is practical only on the LWTS.

Science will drive the development of instrumentation that will be based on LWTS. These developments already involve close interaction with the user community, which extends across academia, government, and industry. At existing neutron scattering facilities throughout the world, soft matter research continues to be the area of fastest growth and researchers in this field constitute the largest single group of users. We expect this growth to continue and the use of neutron scattering in the biological field to expand still further.

8.1.3 Potential Areas of Study

8.1.3.1 Small Sample Volumes

Neutron scattering, through deuterium labeling, provided the first direct evidence for the Gaussian nature of the conformation of bulk polymer chains. This finding had a profound impact on the understanding of polymers [8.1.5]. Neutron scattering, combined with the selected deuterium labeling of phospholipid molecules within thick multilayer films, similarly provided the first direct indication of their time-averaged, temperature-dependent conformation within a bilayer [8.1.6, 8.1.7]. Studies of chain conformation have extended to ultrathin films and dilute solutions, but the available flux at present neutron sources limits this increase in scope [8.1.8–8.1.10]. Figure 8.1 shows the data for polymer radius of gyration (R_G) as a function of film thickness (D); the data are derived from many experiments over a two-year period with current neutron sources. The measurements required stacking up to 20 films together. The results are intriguing because they show that R_G is independent of D down to $R_G/D \sim 0.75$. Studies of this kind cannot be readily extended to thinner films or more complex systems with existing sources.

With the current push toward controlling structure at nanometer length scales, the need to probe small sample volumes and dilute concentrations is of paramount importance. The existence of a next-generation, long-wavelength neutron source and the concomitant development of instrumentation and optics will bring new capabilities to the characterization of soft matter using neutrons. For example, SNS instruments will likely enable scientists to characterize biomolecular and polymeric ultrathin microelectronics and photonics films *in situ* directly on a silicon (Si) wafer at concentrations and/or with dimensions that are impossible to access today.

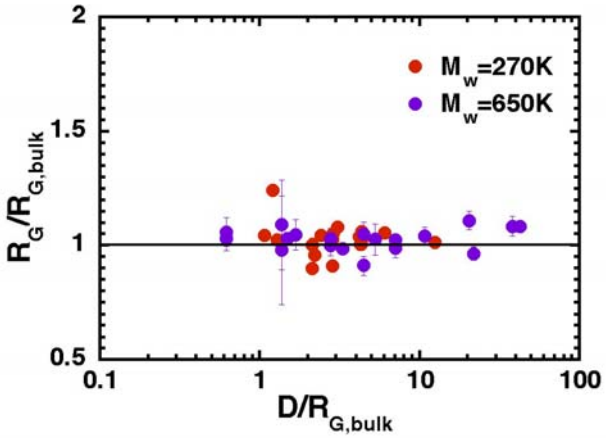

Fig. 8.1. Polymer chain R_G as a function of film thickness D (data from Ref. 8.1.8).

8.1.3.2 Biomolecular Materials

Through a series of elegant SANS experiments that employed selective labeling of pairs of protein subunits combined with contrast matching of the remaining molecule, researchers were able to determine the three-dimensional quaternary structure of the ribosome [8.1.11]. Now, incorporating the deuterium labeling of selected intramolecular sites within a particular macromolecular component, workers are extending this approach to structural studies that explore the richness of phases provided by the interactions of natural proteins, synthetic proteins, and nucleic acids with lipids and polymers [8.1.3]. Figure 8.2 shows two of the self-assembled structures formed from DNA and cationic lipids that are important in the study of synthetic gene delivery systems [8.1.12]. The studies of such new materials in bulk, fiber, and thin-film forms provide the basis for potential technological devices based on biological catalysis, ligand binding specificity (or "recognition"), and macromolecular machines. The potential role of neutron scattering for the characterization of such systems is tremendous but is limited by flux and beam time. The LWTS at SNS will help researchers realize this potential.

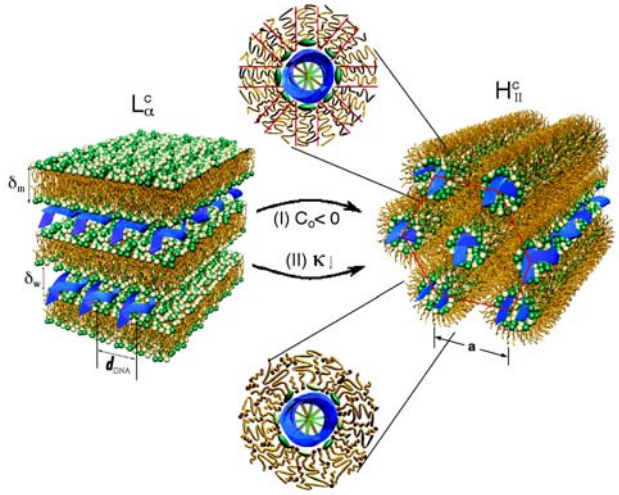

Fig. 8.2. Lamellar phase and columnar inverted hexagonal phase formed from cationic lipid/DNA complexes taken from Ref. 8.1.12 (based on work performed at the Stanford Synchrotron Radiation Laboratory).

8.1.3.3 Complex Polymer Structures

Neutron scattering has provided key insights — unattainable by other means — into the behavior of polymers with compositionally and topologically complex structures. These include mixtures, block copolymers, networks, star polymers, dendrimers, and graft polymers. Significant discoveries already made by using neutron scattering include the following: chain stretching in block copolymers, the role of conformational asymmetry parameter in controlling polymer miscibility, the micellar structure of copolymers in supercritical fluids for use in new, environmentally benign solvents, the location of end groups in dendrimers, and the dependence of linear polymers on molecular weight to determine the degree of penetration of linear polymers into highly grafted molecules [8.1.13–8.1.17]. A recent explosion in the number of techniques for synthesis of complex, controlled macromolecular architectures has substantially heightened the need for instruments capable of probing structural conformations and kinetic responses to

external stimuli across the broad range of length and timescales represented in the proposed suite of LWTS instruments.

8.1.3.4 Confinement and Extreme Environments

The penetrating power of neutrons has allowed scientists to investigate polymer intermolecular ordering/disordering under nonequilibrium flow conditions through confined spaces; understanding this phenomenon is important for processing polymers and colloids [8.1.4, 8.1.18]. The high penetrating power of neutrons also allows researchers to develop sample cells and environments for the study of soft matter under conditions that directly match the final end use. For example, the structure of a complex fluid used as a lubricant in a high-speed bearing subject to high shear rate and/or high pressure is of great technological significance. *In situ* experiments could be conducted on such materials using a high-power, next-generation neutron source. Figure 8.3 shows the neutron scattering intensity distribution in an *in situ* experiment to determine the structure in a micellar solution under shear flow near a surface. Similarly, the structure and dynamics of natural or synthetic proteins could be studied under high pressure to provide important information about the physiochemical basis of its structure and folding within biomolecular materials.

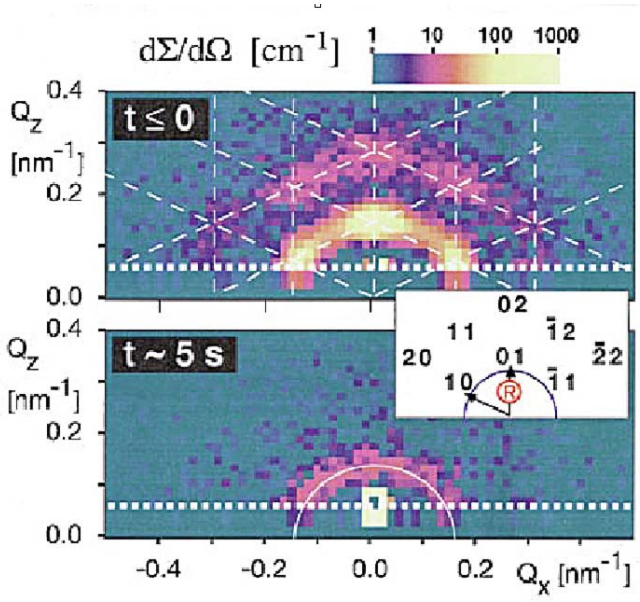

Fig. 8.3. SANS from the surface structure of a micellar solution under shear flow. Top: fully aligned structure; bottom: partially relaxed (Ref. 8.1.17).

8.1.3.5 Dynamics

Scientists have employed inelastic neutron scattering (INS) techniques to demonstrate that the dominant relaxation mechanism in entangled linear polymers is reptation [8.1.19, 8.1.20]. Similarly, we have just begun to investigate the intramolecular dynamics of the photosynthetic protein bacteriorhodopsin within a lipid bilayer membrane. These experiments aim to provide key insights into the role of the protein's environment in its light-induced proton transport function [8.1.21, 8.1.22]. The full range of INS spectrometers proposed for the LWTS will be

key to enabling such studies of the role of intramolecular dynamics in controlling the macroscopic response of soft-matter-based materials.

8.1.3.6 Interfaces and Surfaces

Because interfacial control is crucial to successful implementation of nanotechnology, the study of interfaces is an active area of current research. With a high-flux neutron source optimized for long-wavelength neutron production, scientists will be able to directly follow the dynamics of interfaces in response to perturbations. The broadband reflectometer on LWTS (Sec. 4.5) will allow us to study a wide Q-range without the need to move the sample, a key feature for the study of kinetic processes at fluid surfaces. For example, it will be possible for researchers to observe the response of an interface after exposure to an incident laser pulse during a chemical reaction or in response to local heating (e.g., the pulsed laser polymerization of polydiacetlyene monolayers). The laser pulse could be applied either in phase or out of phase with a harmonic of the neutron pulse.

Many systems form monolayers on fluid surfaces (often on water). The study of these systems requires high flux because of the very small sample volumes. With a high-intensity, low-repetition-rate neutron source, it will be possible for scientists to routinely study the time-dependent evolution of such systems, including the formation of monolayers, structural changes with applied lateral pressure (*in situ* Langmuir trough studies), kinetics of two-dimensional phase transitions, and formation of protein ion channels in lipid films.

8.2 Disordered Materials

8.2.1 Introduction

Liquids, glasses, and amorphous materials (including amorphous semiconductors, molten salts, liquid alloys, and electrolytes, colloids, gels, and polymers) constitute the preponderance of condensed matter in our planet. Such materials are of great commercial importance in modern industrial society [8.2.1–8.2.2]. Depending on the structural units and interaction potentials in the system under study, the time and length scales of these features vary from 10^{-7} to 10^{-13} sec and 1 to 10^{4} nm. The structures and dynamics of disordered systems are complicated; the complexity varies from modest orientational disorder of molecules in crystalline solids to the extreme disorder limit encountered in a multicomponent true glass. Confining material to catalytic surfaces and in porous sieves also creates disorder and new phenomena. The dynamic behavior of disordered materials ranges from local vibration and rotational tunneling of individual molecules to many-body collective phonon-like excitations and from excess "local" vibrational modes (the boson peak) to slow relaxations and diffusion processes.

8.2.2 Opportunities for Neutron Scattering in the Study of Disordered Materials

Much neutron data today lack the statistical precision or resolution to distinguish between different models of many phenomena. Both limitations (precision and resolution) can be dramatically removed by the LWTS and accompanying new instruments such as the SANS (BRIMS) diffractometer (Sec. 4.1), the 200-neV crystal analyzer spectrometer (Sec. 4.2), the spin echo spectrometer (Sec. 4.7), and the high-resolution chopper spectrometer (Sec. 4.9).

These instruments, coupled with the high signal-to-noise ratio possible on the LWTS, will bring a revolution in precision — taking experimental testing of theory to a new level.

8.2.3 Potential Areas of Study

8.2.3.1 Water, Ice, and Water-Rich Complex Fluids

Water is crucial to life on earth. Basic to biological function and a great range of chemical processing technologies and serving as a prototype hydrogen-bonded liquid and solid, water has received concentrated scientific attention for many years. Even so, we do not adequately understand the physicochemical properties of water even in its pure form, let alone its complex roles in biological, ecological, and geological systems. Neutron studies have provided key information on the organization of atoms in no less than a dozen structural forms of water and clarified the origin of differences between excitation spectra of water, amorphous ices, and hyperquenched water. However, to date, the data allocated fail to distinguish the many competing models of hydrogen bonding or of interatomic potentials such as those employed in computer simulations. Making the situation even more complicated, the soft nature of disorder in water and water-rich systems promotes arrangements of structural units that are extremely sensitive to changing temperature, dilution, pH, etc. Forefront challenges are to understand the following: (a) aqueous solutions, (b) hydrolysis reactions, (c) mobility of drugs and nutrients in organs, (d) mobility of nutrients in soils, (e) proton conduction in liquid electrolytes, (f) the formation of liquid crystals in lipids and water in biological membranes, (g) entrapment of water in concrete, and (h) denaturation of proteins. Present neutron scattering instrumentation lacks the resolution and the ranges of energy and momentum transfer to allow researchers to critically address these challenges. Better understanding of these materials will lead to improvements in fields as diverse as drug delivery, road quality, and food preservation. The very high resolution and wide dynamic range of cold-neutron instruments at LWTS will be keys to scientific progress in studies of water-related materials.

8.2.3.2 Fragility, the Boson Peak, and Relaxation in Glassy Materials

Many glass-forming phenomena are poorly understood [8.2.6–8.2.7], in spite of the widespread occurrence of real materials in amorphous states. The excess specific heat, the vanishing excess entropy around the glass transition temperature (T_g), and the plateau in the thermal conductivity at low temperatures are well known but still inadequately explained universal features of glassy solids. These phenomena — the occurrence of Boson peaks, the diverging relaxation time, and the variation of the fragility defined by T_g-scaled Arrhenius plots of the viscosities — all call for high-precision INS measurements to illuminate what features of the potential energy hypersurface define them. INS has already surpassed Raman scattering in characterizing of the Boson peaks. To reveal the nature of two-level systems or floppy modes [8.2.8], scientists must make high-resolution, low-energy-transfer measurements. High-temperature measurements, carried out over a wide range of wave vector and energy transfer, provide information regarding anharmonic decay of vibrational states [8.2.9]. At present, there are not a sufficient number of appropriate instruments, and those that are available are not capable of carrying out the measurements needed to progress in these fields. LWTS instruments will provide the capacity essential for new discoveries in glass dynamics in the 21st century.

8.2.3.3 Neutron Brillouin Scattering

Conventional Brillouin scattering (NBS) using laser light probes only the region very near Q = 0, the hydrodynamic continuum regime. Brillouin scattering carried out with neutrons (also x-rays) provides access to the region far into the first Brillouin zone, where low-energy dispersive excitations merge into the continuum excitations. NBS results will reveal the viscoelastic properties of aqueous solutions and molten metals and the distinction between localization and plane-wave-like propagation in orientational glasses and structural glasses.

The realization of NBS is fraught with difficulties. Measurements require high (and clean) energy transfer resolution (< ~0.1 meV), as well as a wide range of rather small wave vectors (~ 0.01–1.0 $Å^{-1}$). Moreover, kinematics requires use of neutron speeds in excess of the speed of sound — sometimes implying rather high neutron energies. Spectrometers available even at the premier neutron sources lack the intensity and resolution to observe the low-energy excitations near the elastic line.

Even though the technical challenges have not yet been overcome, there has been much debate in the past 20 years regarding the data that do exist. Examples are the controversies about the existence of fast sound in liquid water [8.2.10, 8.2.11] and the interpretation of the transition from normal to fast sound (hard clusters, acoustic-like and optic-like mode interactions, the dynamic cage model, etc.) [8.2.11–8.2.12]. Many scientists have exchanged ideas on the decay of acoustic excitations in vitreous silica and glassy selenium (Ioffe-Regel crossover, mode-coupling theory, anharmonicity, etc.) and the possible evolution to Boson peaks via localization [8.2.13–8.2.21]. The evidence leads to the compelling conclusion that contemporary models will be clarified and new theories will emerge with new instrumentation such as the HRCS at the LWTS.

8.2.3.4 Quantum Systems, Porous Media, and Disorder

The properties of disordered and confined liquids, solids, membranes, and films (quantum and classical) are of great fundamental interest [8.2.22]. Indeed, 20 to 25% of NSF-funded initiatives in the Condensed Matter Physics Program of the Division of Materials Research address some aspects of disorder. The scientific goals are to reveal the impacts of disorder, doping, or confinement on Bose-Einstein condensation; or superconductivity; or phase transitions; and on the magnetic, thermodynamic, elastic, chemical, and biological properties of these systems. There are many examples in which the role of disorder is not yet understood: quantum liquids (^{4}He and ^{3}He) in confined geometries [8.2.23], electrons (Fermions) in disordered materials [8.2.24], Cooper-paired electrons (Bosons) in Josephson arrays and films [8.2.25], Cooper pairs and flux lines in high-Tc materials [8.2.26], and disordered polymers and membranes. These widely different systems share common physical principles such as scaling, universality classes, Bose condensation, superfluidity (conductivity), commensuration, and localization [8.2.22]. Understanding and discovery in one system can be transferred to the others.

Underlying and driving most of the afore-mentioned properties (e.g., superfluidity and phase transitions) are the excitations, especially the Bose excitations [8.2.27]. Disorder introduces subtle changes in these excitations, such as small energy shifts, new low-energy excitations, gaps in dispersion curves, and small (but critical) excitation lifetimes. Detecting these small changes

requires neutron spectrometers that have high resolution and high signal-to-noise ratios, which can be provided only by a brand-new facility such as the LWTS. The IRIS instrument at ISIS (energy transfer resolution of 15 μeV) is now the one that is generally best adapted to these measurements. An instrument that offers resolution below 1 μeV, such as the 200-neV crystal analyzer spectrometer described in Section 4.2, is needed. That instrument will provide the combination of high flux and resolution sufficient to reveal the underlying, low-energy excitations in materials such as those previously listed and in biological systems. Such an instrument, in conjunction with the 2-μeV instrument at the HPTS, would allow scientists to make the connections between excitations, phase transitions, and Bose condensation and open doors to new discoveries in this fundamental field.

8.3 Magnetism

8.3.1 Introduction

Correlations between multiple degrees of freedom are the essence of magnetism. Consequently, most breakthroughs in many-body physics are linked to this field. Magnetism is intrinsic to the technologies that shape our present and future. Efficient transformers for energy transport, transducers, motors, sensors, and electronic information storage — all these technologies rely in essential ways on understanding and controlling magnetic materials. The vitality of both science and engineering related to magnetism has led to a rapid and lucrative concept-to-product cycle. A recent spectacular example was multilayer giant magnetoresistance (GMR), a phenomenon that went from laboratory to consumer in less than 10 years [8.3.1].

8.3.2 Opportunities for Neutron Scattering in the Study of Magnetism

Since its inception, neutron scattering has played a pivotal role for magnetism R&D. Past achievements — including the discovery of Néel and spin glass order, spin waves, and critical fluctuations — have been acknowledged with major awards, including the Buckley Prize to R. J. Birgenau and the Nobel Prize to Cliff Shull. More recently, the fields of thin-film magnetism, colossal magnetoresistance (CMR), high-temperature superconductivity, and quantum magnetism have benefited immensely from knowledge derived from neutron scattering.

8.3.3 Potential Areas of Study

Major challenges that emerged from our workshop in magnetism at the LWTS include (a) understanding and controlling the interplay between charge, spin, and lattice degrees of freedom in oxides; (b) identifying and characterizing novel phases and phase transitions in interacting Fermi systems; and (c) determining the magnetic structure, excitations, and interactions in nanoscale engineered magnets ranging from multilayers, through granular solids, to molecular magnets. The LWTS will play an important role in meeting these challenges.

8.3.3.1 Competing Spin, Charge, and Lattice Degrees of Freedom

The competition between charge, lattice, and spin degrees of freedom can lead to complex ordered phases in which strong short-range interactions balance against longer range interactions such as strain and coulomb forces. These competing degrees of freedom can give rise to a large

number of interesting and potentially useful physical properties. Examples are reports of the formation of dynamic charge ordering in superconducting $La_{2-x}Sr_xCuO_4$ and $YBa_2Cu_3O_{7-x}$ [8.3.2–8.3.4] and of short-range charge correlations that melt with the onset of ferromagnetism and lead to CMR in the manganites $La_{1/3}Ca_{2/3}MnO_3$ and $La_{1.2}Sr_{1.8}Mn_2O_7$ [8.3.5–8.3.7] (Fig. 8.4).

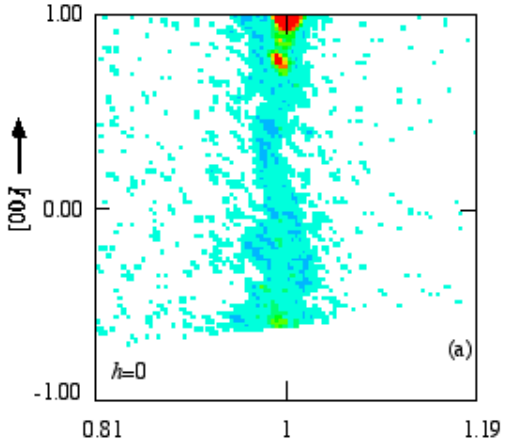

Fig. 8.4. Diffuse neutron scattering from $La_{1.2}Sr_{1.8}Mn_2O_7$, above T_C (at 130 K in the (0k0) plane showing a rod of magnetic scattering along the h0 direction [8.3.7]). TOF single diffractometers measure large volumes of reciprocal space in a single crystal orientation.

Similar effects are also important in quasi-one-dimensional oxides [8.3.8], conducting organic materials, magnetic semiconductors, and geometrically frustrated magnets [8.3.9]. Understanding and ultimately predicting the complex order parameters, low-energy normal modes, and physical properties of these systems have proven to be formidable challenges for the materials science community. Because they relate to all the relevant degrees of freedom, neutrons can furnish many of the needed insights. However, to realize this potential, researchers need instrumentation that can probe small quantities of materials with high signal-to-noise ratio over a wide dynamic range in energy and wave vector transfer (Q=0.01–10 $Å^{-1}$, E=100 μeV–20 meV). The LWTS will allow dramatic progress in this area. The bright cold-neutron pulses enable optimized instrumentation to probe the key nanoscale structure and low-energy dynamics much more efficiently and with greater sensitivity than is currently possible. The proposed magnetism and diffuse scattering instrument (Sec. 4.3) is one such instrument.

8.3.3.2 Quantum Criticality

In recent years, it has become evident that the usual paradigms for understanding metals and magnets break down dramatically near a quantum phase transition [8.3.10]. These breakdowns occur when varying parameters — such as pressure, magnetic field, or dopant concentration — have driven to absolute zero the critical temperature of a classical phase transition. Although the quantum critical point (QCP) then lies at the absolute zero temperature, its existence can have profound consequences for physical properties over a large portion of the phase diagram.

Quantum critical phenomena may play an important role in a wide class of correlated systems, including itinerant magnets, heavy Fermion systems, ferroelectrics, and unconventional superconducting compounds [8.3.11]. While theoretical work on quantum criticality has progressed rapidly, experiments are only just beginning to access critical exponents and scaling functions in selected model systems. Important questions remain regarding: (a) the extent and

role of spatial magnetic correlations at the QCP in metals [8.3.12], (b) the role of disorder close to the QCP [8.3.13], and (c) whether real materials fall into quantum critical universality classes. Neutron scattering, and the LWTS in particular, will be important tools for answering these questions. Future experiments will need to probe fluctuations over a wide range of energies and temperatures, examine a wide range of materials (many of which can only be produced as small single crystals), and probe materials under extreme thermodynamic conditions. The LWTS, as a bright cold-neutron source, will provide unique capabilities for probing low-energy fluctuations with high sensitivity and will have a definite impact in this emerging area of condensed matter physics. A long-wavelength, single-crystal TOF diffractometer at the LWTS would also facilitate discovery and characterization of weak order parameters close to QCPs in small single crystals.

8.3.3.3 Magnets by Design

Advances in synthetic chemistry, materials processing, and thin-film deposition techniques have greatly expanded our ability to pattern magnetic materials at the nanometer scale. Nonvolatile electronic information storage systems are largely based on thin-film magnetism, so this subject is of immense technological importance. Potential benefits from greater understanding of magnetism at the nanometer scale include faster and denser information storage systems [8.3.14] and ultrafast quantum computing [8.3.15]. Many of the challenges in the field lie in developing processing techniques. Neutron scattering will, however, be crucial to improving our understanding of (a) the chemical and magnetic interface between materials, (b) dynamic phenomena in magnets confined to the nanometer scale, and (c) magnetic interactions through nonmagnetic material. The greater brightness of the LWTS will be essential if neutron scattering instrumentation is to keep up with increased technological complexity and miniaturization. Long-wavelength neutron reflectometry (Sec. 4.5) and diffraction (MiDaS, Sec. 4.3) are the dominant techniques for studying magnetism [8.3.16].

Researchers will also need to probe lateral magnetic structure, such as magnetic dots, on scales up to 1 μm. The wide dynamic range of TOF reflectometers and SANS instruments (BRIMS, Sec. 5.1) at the LWTS may also facilitate an entirely new class of experiments that probe nonequilibrium structure following perturbations phased to the proton pulse. Such experiments could result in essential new insights regarding domain wall structure and dynamics in a wide range of magnetic materials. In the area of high-resolution spectroscopy (Sec. 4.9), the LWTS may enable direct observation of quantum-tunneling-induced gaps in the excitation spectrum of magnetic nanoparticles. These experiments using LWTS instruments could open a new window on quantum coherent phenomena at the nanometer scale.

An alternative tool for designing new magnetic materials is synthetic chemistry. The soft structural constraints provided by organic ligands enable molecular-level control of the topology and strength of magnetic interactions. Because of the covalency and complex geometry of molecular magnets, our understanding of interactions and spin density distributions in these materials is rudimentary. Polarized neutron diffraction provides direct access to spin density distributions [8.3.17], but unfortunately, there is currently no scientifically competitive instrumentation in the United States to conduct these studies. Moreover, the large unit cells and small sample sizes that characterize novel molecular magnets make these experiments difficult,

even on the best machines at the ILL. The availability of high-intensity, long-wavelength, polarized neutrons at the LWTS will enable dramatic progress.

Ultra-high-resolution spectroscopy of quantum tunneling in molecular magnets is another area in magnetism where, for example, the CAS (Sec. 4.2) at the LWTS can have a major impact [8.3.18–8.3.20].

8.4 Powder Diffraction

8.4.1 Introduction

Existing powder diffractometers at both neutron and synchrotron radiation sources attract a broad user community because the technique is applicable to many different classes of materials. Currently, areas under study range from proteins, fundamental materials physics and chemistry, earth science, designer porous solids, and self-assembled nanostructures to engineering alloys and cement. The development of new instruments and capabilities will spur the growth of the user community in terms of both numbers and diversity.

8.4.2 Opportunities for Neutron Scattering in the Study of Powder Diffraction

The LWTS will provide an opportunity to construct powder diffractometers with characteristics that complement those of the HPTS and provide world-class performance. The envisioned HPTS instrumentation will cover a d-spacing range well matched to many materials and provide good resolution combined with very high data rates. The instrumentation will be invaluable for performing parametric studies, such as the examination of phase transitions and thermal expansion characteristics. However, the high repetition rate at the HPTS, its moderator characteristics, and optimization for high data rates make the proposed powder diffractometer (POW-GEN3) at the HPTS less than ideal for two important classes of experiments:

The materials problems examined by scientists and engineers are becoming increasingly complex. This complexity is often associated with new, fascinating, and potentially useful properties and may show up structurally as very large unit cells, phase coexistence, subtle superlattices and distortions, or additional length scales that have to be considered. To handle these structural problems, scientists need a powder diffractometer optimized for both excellent resolution ($\Delta d/d$) and low background.

We propose the construction of an ultra-high-resolution ($\Delta d/d \sim 3 \times 10^{-4}$) instrument, UHRPD (Sec. 4.4) to meet these needs (see Fig. 4.6).

Cases involving an additional length scale, such as ordered nanoporous materials or arrays of self-assembled nanoparticles, also require, an instrument that is capable of accessing very large d-spacings. The proposed SANS instrument, BRIMS (Sec. 4.1), at the LWTS will initially meet these needs (see Fig. 4.2). However, we foresee the need, at some time in the future, for a long-wavelength powder diffractometer, capable of delivering data over a very large d-spacing range to enable the high-resolution examination of materials with orders at both the atomic and multinanometer length scales.

8.4.3 Potential Areas of Study

8.4.3.1 Complexity and the Need for Ultra-High Resolution

The scientific impact of the current generation of ultra-high-resolution synchrotron powder x-ray diffractometers illustrates the need for a new ultra-high-resolution neutron powder diffractometer. Instruments such as those on beamlines X3B1 and X7A at the National Synchrotron Light Source at BNL and BM16 at the European Synchrotron Radiation Facility at Grenoble, France, offer resolutions ($\Delta d/d$) in the low 10^{-4} range. They have aided in developing our understanding of many important classes of materials such as C_{60} derivatives [8.4.1–8.4.4], high-Tc superconductors [8.4.5–8.4.8], zeolites [8.4.9–8.4.12], piezoelectrics [8.4.13–8.4.15], and manganite CMR/GMR compounds [8.4.16–8.4.19].

The high resolution of these synchrotron instruments has facilitated the solution of complex new zeolite structures [8.4.9–8.4.12], the examination of phase coexistence [8.4.20] in superconductors [8.4.7, 8.4.8] and manganite CMR materials [8.4.16, 8.4.17, 8.4.20], and the observation of subtle distortions in lead zirconium titanate compositions close to the morphotropic phase boundary [8.4.13, 8.4.14]. This kind of work can have significant scientific and technological implications. Synchrotron powder diffraction was used to characterize the first ultralarge-pore zeolite to be prepared (UTD-1) [8.4.9–8.4.11]. Its pores are large enough to facilitate improvements in petroleum refining [8.4.9, 8.4.10]. The observation of a monoclinic distortion in Pb-Zr-Ti-O (PZT) close to the morphotropic phase boundary [8.4.13, 8.4.14] led to a reinterpretation of the piezoelectric response of this important material [8.4.15].

Figure 8.5, showing a synchrotron diffraction pattern for a two-phase $BaBiO_3$ sample, illustrates the benefits of ultra-high resolution. Laboratory x-ray and typical neutron instruments are incapable of resolving this kind of splitting. The combined synchrotron and neutron studies of Woodward [8.4.17] on phase coexistence in $(Nd_{1/2}Sr_{1/2})MnO_3$ also make it clear that relying on medium-resolution neutron diffraction data alone could lead to grossly incorrect conclusions.

Synchrotron x-ray diffractometers are often the instruments of choice because of their superb resolution. When neutron diffractometers with comparable or better resolution and good data rates become available, many problems involving complex materials will be better handled because of neutron sensitivity to light atoms, different scattering contrast levels, good intensity at high Q, and sensitivity to magnetic ordering. For very complex structural problems, the combination of ultra-high-resolution neutron data with synchrotron data will provide unprecedented capabilities. The UHRPD and BRIMS at the LWTS will be the first to provide the neutron capabilities needed to complement the x-ray instruments.

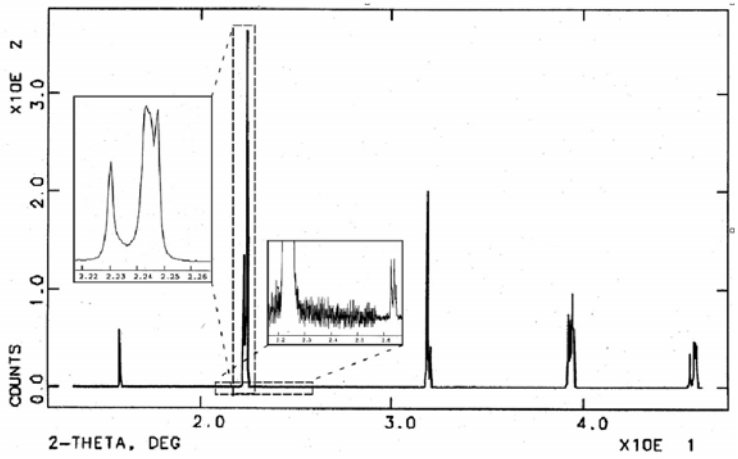

Fig. 8.5. Synchrotron data for "$BaBiO_3$." The splittings indicating the presence of two phases would not have been observable at medium resolution, but the use of x-rays led to problems with the superlattice peaks.

8.4.3.2 Long-Wavelength Powder Diffraction at LWTS

Many materials of current interest display structural features on multiple length scales; examples include mesoporous oxides with pores of nanometer dimensions [8.4.21, 8.4.22] and self-assembled arrays of nanoparticles [8.4.23]. In mesoporous oxides prepared using surfactant templates [8.4.21, 8.4.22, 8.4.24], an ordering of the pores in the system often occurs; there may or may not be ordering on atomic length scales within the walls separating the pores from one another. The self-assembly of nanometer-scale building blocks is currently attracting considerable attention. One interesting group of materials is the self-assembled metal nanoparticles studied by Whetten et al. [8.4.23, 8.4.25]. Each of the individual nanoparticles is crystalline, and they pack together to form well-ordered arrays (see Fig. 8.6a). The diffraction data provide information on nanoparticle packing at low Q and particle internal structure at higher Q (see Fig. 8.6b). Neutron experiments on these materials would, for example, allow scientists to examine the passivating organic groups on the surface of the nanoparticles in the self-assembled solid, leading to improved synthesis techniques. This study cannot be done with x-rays because the scattering from high-Z (large atomic number) atoms in the nanoparticle core is dominant.

The high flux of long-wavelength neutrons from the LWTS is well suited to the construction of an instrument capable of providing good-resolution diffraction data over a very large d-spacing range. We have not yet worked out the design of the instrument that will provide the necessary combination of wide range and medium resolution, although a wide-angle detector on BRIMS (Sec. 4.1) may initially suffice.

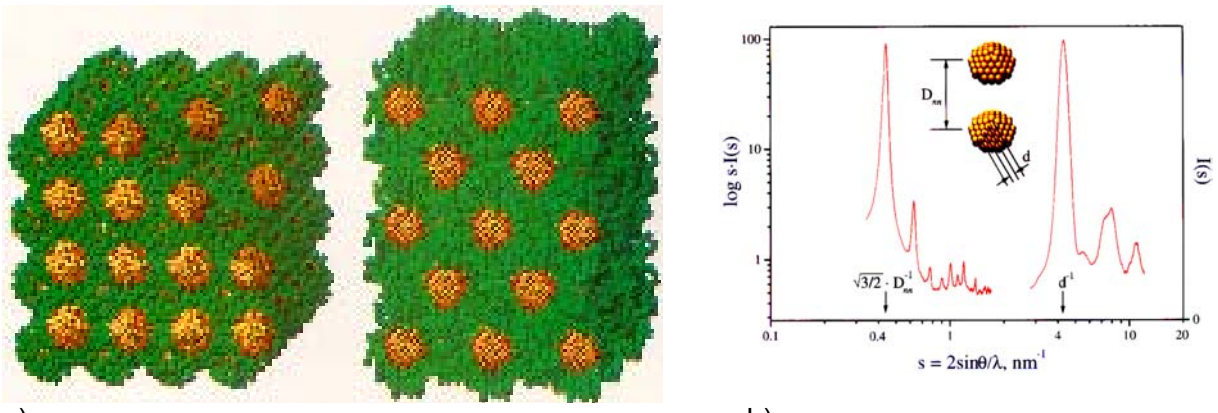

Fig. 8.6. (a) Self-assembled arrays of nanoparticles show order on two distinct length scales giving rise to (b) information at both high and low Q in the diffraction patterns.

8.5 Biological Sciences

8.5.1 Introduction

Knowledge and activity in the life sciences have experienced unprecedented growth in the 20th century. Most experts believe this growth will continue at an enormous rate in the 21st century. Complete sequencing of the human genome, which is considered to be one of the most significant achievements of all time, is a prime example of such progress. Although many of life's mysteries are encoded in the genetic blueprint, the genome sequence gives us only the instruction sets for synthesizing the 50,000 or more proteins present in the human body and tells us very little about how they work in concert to maintain life [8.5.1]. We do know that any single physiological function is carried out by 10 or more protein molecules in concert and that each of these molecules may interact with much larger macromolecular assemblies [8.5.2].

A prerequisite for understanding function is knowledge of the structure of the molecule or molecules of interest. The structure-function hypothesis is well accepted in modern biology; its validity has been confirmed at all levels of molecular organization, from the three-dimensional atomic structures of molecules to the structures of highly complex molecular assemblies in cells. The development and improvement of modern structural biology techniques will be instrumental in realizing some of the lofty expectations that have arisen from the genome project.

Although detailed examination of their structure has revealed much about the function of biomolecules, full understanding of their operation as molecular machines requires information on the wide variety of motions exhibited by these molecules. As well as understanding the principles that lead from sequence to structure — the "protein folding problem" — we also need to understand those principles that lead from structure to dynamics and function [8.5.3]. Moreover, the study of macromolecular dynamics provides us with a rather stringent test of models of intermolecular forces, which are the basis for understanding protein stability and rationalizing protein design [8.5.4–8.5.6]. Neutron scattering offers invaluable tools for studying the structure-function relationship of biological processes in the postgenome era.

8.5.2 Opportunities for Neutron Scattering in the Study of Biological Materials

The following features of neutron scattering methods make them especially useful for investigating the structure and dynamics of macromolecules: (a) Neutron diffraction makes it possible to locate and identify hydrogen atoms as easily as heavy atoms within a macromolecule [8.5.7]; (b) neutron diffraction easily distinguishes deuterium from hydrogen in contrast matching and H/D exchange experiments [8.5.8]; (c) thermal neutrons do not cause radiation damage to biological samples [8.5.9]; and (d) inelastic neutron scattering enables characterizing the dynamics of atoms and molecules [8.5.10]. In the past, U.S. researchers have not been able to make full, effective use of these methods because of the low fluxes and limited access to neutron sources in the United States [8.5.11]. However, the field of macromolecular neutron diffraction outside of this country has exploded. In the past two years, groups in Europe and Japan have published research revealing improvements in molecular models based on neutron vs. x-ray diffraction data [8.5.7, 8.5.9, 8.5.12–8.5.14]. The development of high-efficiency detectors and novel techniques for processing neutron diffraction data is reducing the long measuring times that previously limited neutron diffraction studies [8.5.15, 8.5.16]. The LWTS will make it possible for molecular biologists to perform systematic studies of a large variety of homologous molecules or structurally similar molecules. In these studies, it is the small differences between closely related systems that are important; the high fluxes of long-wavelength neutrons will help to reveal them.

The enormous increase in usable neutron flux provided at the LWTS, along with the increased dynamic range accessible by its spectrometers, will also have a substantial impact not only on structural biology, but also on several areas of biochemistry.

8.5.3 Potential Areas of Study

8.5.3.1 Neutron Single-Crystal Diffraction to Determine the Positions of Protons

In the latter half of the 20th century, worker have applied NMR and x-ray crystallography to discern the three-dimensional structures of several macromolecules such as proteins and nucleic acids, including the intact ribosome, shedding light on many of life's mysteries [8.5.17, 8.5.18]. However, x-ray studies do not readily reveal the structural hydrogen, which constitutes 50% of a macromolecule's atoms. Although high-resolution x-ray structures, combined with molecular modeling, have traditionally been used to determine the positions of hydrogen atoms, a recent study makes it clear that more structural information can be generated from moderate-resolution (2.4-Å) neutron data than from ultra-high-resolution (0.9-Å) x-ray data [8.5.12, 8.5.19, 8.5.20]. The contributions of hydrogen atoms to biological function cannot be overstated. For instance, a hydrogen atom is invariably required to facilitate catalysis. Neutron diffraction structure studies elucidate H/D exchange, enabling us to understand catalytic processes at the molecular level [8.5.21, 8.5.22]. For instance, Kossiakoff and coworkers investigated the catalytic mechanism of the serine protease trypsin using neutron diffraction [8.5.23]; their study showed that the proton is attached to the His-57 rather than the Asp-102 within the catalytic triad. Moreover, scientists can exploit observations of the hydrogen-bond formation between macromolecules and ligands and the water-mediated second-sphere hydrogen-bond formation for drug and ligand design [8.5.24–8.5.28].

Examples of macromolecular single-crystal structures solved by neutron diffraction to date include the following: (a) trypsin [8.5.23, 8.5.29]; (b) RnaseA [8.5.21, 8.5.30, 8.5.31]; (c) crambin [8.5.32]; (d) insulin [8.5.33]; (e) myoglobin [8.5.34, 8.5.35]; (f) lysozyme [8.5.36–8.5.38, 8.5.15], a portion of which is shown in Figure 8.5.1; (g) concanavalin A [8.5.12]; (h) bovine pancreatic trypsin inhibitor [8.5.39]; (i) glycolipids with respect to bacteriorhodopsin [8.5.40]; and (j) endothiapepsin [8.5.13].

Figure 8.7 shows a portion of the structure of HEW lysozyme determined by neutron diffraction illustrating water molecules and hydrogen bonds.

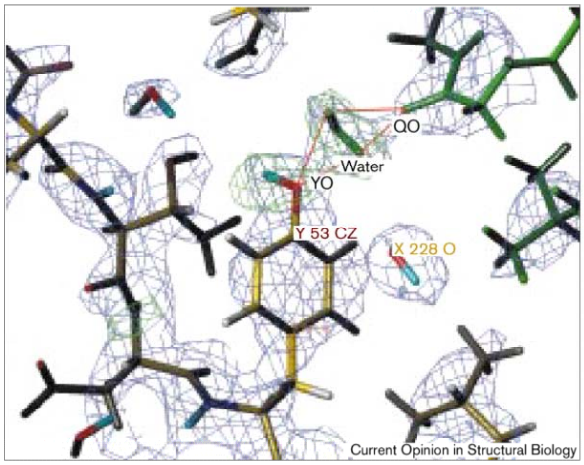

Fig. 8.7. A portion of the HEW lysozyme structure from neutron quasi-Laue diffraction data [8.5.7]. Hydrogen bonds between a water molecule and Tyr53 are shown in red.

The neutron single-crystal TOF Laue technique, successfully employed for small molecules [8.5.41, 8.5.16], will be very effective for use in macromolecular crystallography because of its ability to measure many Bragg reflections by using a stationary sample and stationary detectors and because of its inherently low backgrounds. At the LWTS, the cold-neutron spectrum and low repetition rate are well suited for a single-crystal macromolecular diffractometer (Sec. 4.12) and will dramatically increase the number of protein and nucleic acid structures accessible by using neutron diffraction.

8.5.3.2 Macromolecule-Solvent Interactions

Hydration of macromolecules is necessary for both biological activity and thermodynamic stability; moreover, the use of proper solvent models is extremely important for computational biology. However, it has been very difficult to model solvation reliably, making it difficult to accurately compute biochemical parameters such as protein-ligand binding constants. A long-standing controversy regarding the hydration of macromolecules concerns the formation of solvation spheres around macromolecules, as inferred from early x-ray structures. Neutron scattering provides important information on macromolecule-solvent interactions by distinguishing D_2O from H_2O [8.5.42–8.5.45]. The comparison of deuterated neutron structures with corresponding x-ray structures validated the solvation sphere models [8.5.46]. These studies clearly show that the density of bound solvent is greater than that of bulk solvent. Neutron and x-ray data have been the basis for modeling a solvent as a series of shells with well-defined spatial and physical characteristics [8.5.35, 8.5.44]. The expected high flux in the

desirable spectral range from the cold moderators at the LWTS will make the SANS instruments there ideal for studying solvation of macromolecules and will contribute to the development of accurate solvent models that will benefit in the field of computational biology.

8.5.3.3 Biological SANS as a Tool for Studying Macromolecular Assembly

X-ray crystallography is the single most powerful method for accurately characterizing macromolecular structures, but it is difficult to produce the required crystals of those very large complexes. One alternative, solution-based SANS in contrast-matching experiments, has proven its ability to gather global information on multiple subunit assemblies and large conformational changes. Well-known SANS success stories include the solution of the structures of ribosomes [8.5.47], viruses [8.5.48], and RNA and DNA-protein complexes [8.5.49]. The power of deuterium labeling in SANS permits researchers to compare one component to the others in a multicomponent assembly, and it contributes a significant advantage over complementary techniques such as electron microscopy and small-angle x-ray scattering. SANS complements both x-ray and neutron single-crystal diffraction techniques because it is solution-based and can probe the kinetics of macromolecules. Major hindrances to biological SANS so far have been the limited access to experimental stations and long measuring times. The planned SANS station at the LWTS (BRIMS, Sec. 4.1) will promote the application of neutron scattering to solve challenging biological problems.

8.5.3.4 Protein Dynamics: "Complete" Dynamical Information Made Possible by a Versatile Set of Instruments

Protein dynamics relates to two very important biomolecular processes: conformational flexibility that is essential for enzyme catalysis and the several changes that occur in the final stages of protein folding. Experimental studies of macromolecular dynamics normally employ such optical techniques as photon correlation spectroscopy [8.5.50], fluorescence correlation and photobleaching recovery techniques [8.5.51, 8.5.52], and Brillouin light scattering [8.5.53]. These techniques cover relatively long timescales compared to the neutron spectroscopic methods of quasielastic scattering and spin echo spectroscopy. Although workers have used multidimensional NMR to study slow local incoherent dynamical motions, the method does not provide information on long-range correlations [8.5.54–8.5.56]. On the other hand, neutron scattering spectroscopies cover a much wider dynamic range — from nanoseconds to picoseconds — permitting, for example, studies of conformational flexibility of macromolecules [8.5.3, 8.5.10, 8.5.57–8.5.59], protein folding [8.5.3, 8.5.59], and dynamics of molecules tethered to a surface [8.5.57, 8.5.60, 8.5.61]. The methodologies are therefore complementary rather than competitive. There is enormous potential for new insights into biomolecular dynamics from the use of quasielastic and inelastic neutron scattering at pulsed neutron sources. The TOF methods used at sources such as the LWTS offer inherent advantages, including potentially greater Q-resolution, a larger dynamic range, access to the lowest energy transfers, and high-energy resolution [8.5.62]. A particularly important new direction involves accessing slow ($\sim 10^{-7}$ sec) dynamics with the use of long-wavelength neutrons, as will be possible using the 200-neV-resolution crystal analyzer spectrometer at the LWTS (CAS, Sec. 4.2).

8.5.3.5 Membrane Proteins and Lipid Dynamics

About 30% of all proteins encoded in the human genome are incorporated in or attached to a lipid matrix; moreover, the membrane proteins require a lipid matrix for proper folding and function. Among the many important problems of macromolecular dynamics that we expect to address using the LWTS are lipid dynamics in lipid/water interfaces and in the hydrophobic core of lipid bilayers. Scientists can achieve specificity by selective deuteration of lipid head groups and hydrocarbon chains or by exploiting differences in timescales (e.g., intramolecular chain dynamics vs. lateral diffusion) that can be observed using specific spectrometers. We can evaluate collective and molecular motional processes by using a combination of LWTS spin echo (Sec. 4.6) and backscattering instruments (Sec. 4.2), respectively. Varying the scattering angle and using appropriately oriented samples enables researchers to separate in-plane from out-of-plane motional processes. By collecting quasielastic data from highly oriented bilayer stacks at different hydration levels, we can answer such questions as "What is the origin of intermolecular forces acting between lipids and proteins?" and "What is the origin of forces acting between opposing membranes?"

8.5.3.6 Low-Angle Diffraction and Reflectometry: Macromolecular Assembly in Membranes and Fibers

Scientists have obtained definitive information concerning the intramolecular structures of selected macromolecular components and their assembly within these supramolecular structures by conducting low-angle diffraction studies of oriented biological membrane multilayers, oriented fibers of nucleic acids, and filamentous proteins and viruses [8.5.63–8.5.70]. Contrast matching and deuteration of selected intramolecular sites are key advantages of neutron scattering in these applications. The combination of these results with high-resolution structures of individual macromolecular components provided by x-ray crystallography greatly enhances our understanding of these supramolecular structures. The dramatic gains in long-wavelength neutron flux provided by the LWTS will have a major impact on studies of the structures and kinetics of supramolecular complexes in oriented fibers, multilayers, and single monolayers conducted using low-angle neutron diffraction (Sec. 4.1) and neutron reflectometry (Sec. 4.4). Most importantly, the facility will provide for a dramatic reduction in data collection times for experiments that involve an extensive systematic series (for instance, comparisons of isomorphous samples with deuterated vs. protonated components, whose long-term stabilities can be problematic). Scientists can extend the studies on oriented multilayers down to the level of single bilayers and single monolayers, both on alkylated inorganic multilayer substrates and on a liquid/vapor interface (where the surface pressure controls an additional key thermodynamic parameter). In the former case, the multilayer substrate allows unique phasing of the reflectivity data, providing the scattering length density profile of the bio-organic overlayers directly [8.5.71, 8.5.72].

8.5.3.7 Neutron-Scattering-Based Potentials for Molecular Dynamics

Perhaps two of the most important aspects of macromolecular dynamics accessible at the LWTS are the connection between pico- and nanosecond motions on the Å length scale in native proteins and the results of computer molecular dynamics (MD) simulation studies. For scientists to realize the full potential of MD as a predictive tool, accurate interatomic potentials must be

available. Neutron-scattering data are ideally suited to verifying such potentials because of the ease of calculating neutron-scattering spectra in absolute scale for comparison with experimental results. This approach will become even more powerful as future increases in computing power make it routinely possible to "tune" potentials by comparison with neutron-scattering results. The combined use of MD and INS has already made a significant impact in the study of relatively complex disordered systems [8.5.73]. Examples include biologically important interacting ligands in solution, as well as organic and inorganic materials that are increasingly important to modern technologies. These advances will spur a revolution in materials design and optimization.

8.6 Fundamental Neutron Physics

8.6.1 Introduction

A wide variety of investigations employing low-energy neutrons shed light on important issues in nuclear, particle, and astrophysics; the elucidation of quantum mechanics; the determination of fundamental constants; and the study of fundamental symmetry violation. In many cases, these experiments provide information that is not otherwise available from accelerator-based nuclear physics facilities or high-energy accelerators. An energetic research community in the United States is engaged in "fundamental" neutron physics — the use of neutrons in the study of fundamental physics issues. The LWTS and the HPTS will allow an exciting program of such work in the next decade.

8.6.2 Opportunities for Neutron Scattering in the Study of Fundamental Neutron Physics

Current experiments in fundamental neutron physics address scientific issues in four general categories:

1. The nature of time reversal noninvariance and the origin of the cosmological baryon asymmetry
2. The nature of the electroweak theory and the origin of parity violation
3. The nature and detailed description of the weak interaction between quarks
4. The origin of the heavy elements and other issues in stellar astrophysics

The first category, which lies at the heart of modern cosmology and particle physics, includes the search for the neutron electric dipole moment [8.6.1] and the search for T-odd correlation coefficients in neutron beta decay ("D-coefficient" [8.6.2] and "R-coefficient" [8.6.3]). The following are among the important issues addressed by neutron experiments: whether the baryon asymmetry of the universe is directly related to fundamental T-violation [8.6.4] and whether the magnitude of T-violation is consistent with the predictions of the Standard Model [8.6.5].

The second category involves accurately characterizing the parameters that describe neutron beta decay (lifetime and correlation coefficients [8.6.6]). Comparison of these results provides a basis to determine whether the weak interaction in the charged-current sector is completely left-handed (as it is in the Standard Model) or has right-handed components [8.6.7]. These precision measurements can also furnish important information regarding the completeness of the three-

family picture of the Standard Model through a test of the unitarity of the Cabibbo-Kobayashi-Masakawa matrix [8.6.8]. Neutron beta decay also provides the timescale for big bang nucleosynthesis [8.6.9] and remains the largest uncertainty in cosmological models that predict ^{4}He abundance [8.6.10].

Category three involves the study of the weak interaction between quarks in the strangeness-conserving sector [8.6.11]. This study is very problematic because of the overwhelming direct effects of the strong interaction. As a result, the effective weak couplings in the usual meson-exchange model of the process are poorly understood [8.6.12]; different experiments have yielded contradictory results [8.6.13]. Sensitive experiments conducted using polarized cold neutrons to determine parity violation (an unambiguous tag for the weak interaction) in the n-p, n-D, and n-^{4}He systems afford an opportunity to measure NN weak interactions in simple systems that are free of unknown nuclear structure effects [8.6.14]. Knowledge of these interactions is necessary for understanding parity-violating phenomena in nuclei, such as the recently discovered nuclear anapole moment [8.6.15]; this knowledge is also relevant to quantum chromodynamics (QCD) in the strongly interacting limit.

The final category examines stellar astrophysics and the origin of the heavy elements. Light element nucleosynthesis occurred during the first few minutes of the big bang; however, all isotopes with an atomic mass number greater than seven are created only in stellar processes [8.6.16]. Typically, these stellar processes (“r, “s, “p, etc.) involve competition between neutron capture, which moves isotopes to increasing atomic mass number, and beta decay, which increases atomic number. The relative isotopic abundances are particularly sensitive to the neutron capture cross sections of radioactive nuclei with lifetimes comparable to s-process timescales (months to years [8.6.17]). Intense neutron sources in the few-keV energy regime (corresponding to stellar temperatures) provide the only experimental method for obtaining this information.

Both statistics and systematic effects significantly limit essentially all the experiments in this program. During the last few years, it has become apparent that a pulsed source offers unique opportunities for addressing potential systematic errors in these very sensitive experiments. For example, the current generation of experiments employs neutron TOF to accurately determine neutron polarization [8.6.18], account for the effects of stray magnetic fields, identify momentum-dependent parasitic effects, and improve signal-to-noise ratios. A dedicated fundamental neutron physics beamline at the SNS — the most intense pulsed source in the world — accommodating long-term experiments in sequence, will be uniquely suited to address both the statistical and systematic issues in future experiments.

8.6.3 Potential Areas of Study

A recent international workshop [8.6.19] identified the following categories of specific experiments that should be pursued and technical facilities that should be developed in the initial fundamental physics program at the SNS. We have included brief comments regarding the advantages of a pulsed neutron source following each category description.

(1) Experiments to measure the weak NN interaction for example, gamma asymmetry in np and possibly nD capture, neutron spin rotation measurements in np and possibly nD, and

n-^{4}He. A spallation neutron source provides TOF information that allows important checks of possible systematic effects.

(2) In-beam neutron decay experiments that require absolute neutron polarization measurements (A and B coefficients). A spallation source provides neutron TOF information, which allows scientists to exploit polarized ^{3}He neutron polarizers in a powerful way.

(3) Neutron cross-section measurements in the keV range on radioactive samples for nuclear astrophysics. Only spallation sources produce neutrons of adequate fluxes in this energy regime. Neutron TOF allows for the resolution of nuclear resonances. The increased intensity of the SNS allows researchers to study interesting radioactive isotopes that are only available in very small samples.

(4) Measurements with UCNs (such as neutron beta-decay measurements and the neutron electric dipole moment), which operate in a short-fill, long-counting mode. A high-peak-intensity pulsed source allows for greatly increased signal-to-noise ratios.

(5) The production of ultracold neutrons [8.6.20] using a stand-alone, low-current spallation target would provide a very high density of UCN and would allow improved measurement of neutron beta-decay parameters [8.6.21] and, perhaps, the neutron electric dipole moment. A very low power spallation source for UCN production is possible only at an accelerator.

Participants in the TUNL workshop concluded that in each of the scientific areas in which fundamental neutron physics measurements have an important impact, there are crucial experiments that can best be performed at the SNS — some at the HPTS, some best suited for the LWTS.

8.7 References

8.1.1 P.G. de Gennes, J. Badoz, and A. Reisinger "Fragile Objects: Soft Matter, Hard Science and the Thrill of Discovery," Copernicus Books, NY (1996).

8.1.2 P. Lindner and G. Wignall, "Neutron Scattering Measurements of Soft Matter," *MRS Bulletin* **24:** 34–39 (1999).

8.1.3 J.K. Blasie P. Timmins, "Neutron Scattering in Structural Biology and Biomolecular Materials," *MRS Bulletin* **24:** 40–47 (1999).

8.1.4 P. Butler, "Shear Induced Structures and Transformations in Complex Fluids," *Curr. Opin. in Coll. and Interf. Sci.* **4:** 214–221 (1999).

8.1.5 H. Benoit, J.P. Cotton, D. Decker, B. Farnoux, J.S. Higgins, G. Jannink, R. Ober, and C. Picot, "Dimensions of a Flexible Polymer Chain in the Bulk and in Solution," *Nature,* **245:** 13–15 (1973).

8.1.6 G. Büldt, U. Gally, J. Seelig, and G. Zaccai, "Neutron Diffraction Studies on Phosphatidyl-choline Model Membranes 1. Head Group Conformation," *J. Mol. Biol*. **134:** 673–691 (1979).

8.1.7 G. Zaccai, G. Büldt, A. Seelig, and J. Seelig, "Neutron Diffraction Studies on Phosphatidyl-choline Model Membranes 2. Chain Conformation and Segmental Disorder," *J. Mol. Biol*. **134:** 693–706 (1979).

8.1.8 R.L. Jones, S.K. Kumar, D.L. Ho, R.M. Briber, and T.P. Russell, "Chain Conformation in Ultrathin Polymer Films," *Nature,* **400:** 146–149 (1999).

8.1.9 Y.B. Melnichenko and G.D. Wignall, "Dimensions of Polymer Chains in Critical Semidilute Solutions," *Phys. Rev. Lett*. **78:** 686–688 (1997).

8.1.10 Y.B. Melnichenko, M.A. Anisimov, A. Povodyrev, G.D. Wignall, J.V. Sengers, and W.A. Van Hook, "Sharp Crossover of the Susceptibility in Polymer Solutions near the Critical Demixing Point," *Phys. Rev. Lett.* **79:** 5266–5269 (1997).

8.1.11 M.S. Capel and P.B. Moore, "Quaternary Structure of the Small Ribosomal-Subunit of Escherichia-Coli Determined by Neutron Diffraction," *J. of Appl. Cryst.,* **21***,* 823–827 (1988) and M.S. Capel, M. Kjeldgaard, D.M. Engelman, and P.B. Moore, "Positions of S2, S13, S16, S17 and S21 in the 30-S-Ribosomal Subunit of Escherichia-Coli," *J. Mol. Bio.* **200:** 65–75 (1988).

8.1.12 I. Koltover, T. Salditt, J.O. Rädler, and C.R. Safinya, "An Inverted Hexagonal Phase of Cationic Liposome-DNA Complexes Related to DNA Release and Delivery," *Science* **281:** 78–81 (1998).

8.1.13 K. Almdal, J.H. Rosedale, F.S. Bates, G.D. Wignall, and G.H. Fredrickson, "Gaussian-Coil to Stretched-Coil Transition Block Copolymer Melts," *Phys. Rev. Lett*. **65:** 1112–1115 (1990).

8.1.14 P.A. Weimann, T.D. Jones, M.A. Hillmyer, F.S.J.D. Londono, Y. Melnichenko, G.D. Wignall, and K. Almdal, "Phase Behavior of Isotactic Polypropylene-Poly(ethylene/ ethyl-ethylene) Random Copolymer Blends," *Macromolecules* **30:** 3650–3658 (1997).

8.1.15 J.B. McClain, J.D. Londono, D. Chillura-Martino, R. Triolo, D.E. Betts, D.A. Canelas, H. D. Cochoran, E.T. Samulski, J.M. Simone, and G.D. Wignall, "Design of Nonionic Surfactants for Supercritical Carbon Dioxide," *Science* **274:** 2049–2052 (1996).

8.1.16 B.D. Vogt, G.D. Brown, V.S. RamachandraRao, and J.J. Watkins; "Phase Behavior of Nearly Symmetric Polystyrene-block-Polyisoprene Copolymers in the Presence of CO_2 and Ethane," *Macromolecules* **32:** 7907–7912 (1999).

8.1.17 S. Choi, R.M. Briber, B.J. Bauer, D.-W. Liu, and M. Gauthier, "Small Angle Neutron Scattering of Blends of Arborescent Polystyrenes," *Macromolecules* **33:** 6495–6501 (2000)

8.1.18 W.A. Hamilton, P.D. Butler, L.J. Magid, Z. Han, and T.M. Slawecki, "Fast Relaxation of a Hexagonal Poiseuille Shear-Induced Near-Surface Phase in a Threadlike Micellar Solution," *Phys. Rev. E*. **60:** R1146–R1149 (1999)

8.1.19 P. Schleger, B. Farago, C. Lartigue, A. Kollmar, and D. Richter, "Clear Evidence of Reptation in Polyethylene from Neutron Spin-echo Spectroscopy," *Phys. Rev. Lett.* **81:** 124–127 (1998)

8.1.20 B. Ewen, "Neutron Spin Echo Investigations of Polymer Dynamics," *Curr. Opin. in Solid State & Mat. Sci.* **3:** 606–609 (1999)

8.1.21 V. Réat, H. Patzelt, M. Ferrand, C. Pfister, D. Oesterhelt, and G. Zaccai, "Dynamics of Different Functional Parts of Bacteriorhodopsin: H-H-2 Labeling and Neutron Scattering," *Proc. Natl. Acad. Sci. USA* **95:** 4970–4975 (1998)

8.1.22 U. Lehnert, V. Réat, M. Weik, G. Zaccai, and C. Pfister, "Thermal Motions in Bacteriorhodopsin at Different Hydration Levels Studied by Neutron Scattering:

Correlation with Kinetics and Light-Induced Conformational Changes," *Biophys. J.* **75:** 1945–1952 (1998)

8.2.1 "New functionality in glass," *Materials Research Bulletin*, **23:** (11) (1998).

8.2.2 "Condensed-Matter and Materials Physcis: Basic Research for Tomorrow's Technology," National Research Council (National Academy Press, Washington D.C.), Chapters 5 and 6 (1999).

8.2.3 B. Jönsson, B. Lindman, K. Holmberg, and B. Kronberg, "Surfactants and Polymers in Aqueous Solution," (Wiley, Chichester, 1998).

8.2.4 D.F. Evan and H. Wennerström, "The Colloidal Domain, When Physics, Chemistry, Biology and Technology Meet," 2nd Edition (Wiley-VCH, New York) (1999).

8.2.5 R.G. Larson, "The Structure and Rheology of Complex Fluids," (Oxford University Press, New York) (1999).

8.2.6 C.A. Angell, K.L. Ngai, G.B. McKenna, P.F. McMillan, and S.W. Martin, "Relaxation in Glassforming Liquids and Amorphous Solids", *J. Appl. Phys.* **88:** (6), 3113–3157 (2000).

8.2.7 C.A. Angell, "Ten Questions on Glassformers, and a Real Space 'Excitations' Model with some Answers on Fragility and Phase Transitions," *J. Phys.: Condens. Matter* **12:** 6463–6475 (2000).

8.2.8 K.O. Trachenko, M.T. Dove, M.J. Harris, and V. Heine, "Dynamics of Silica Glass: Two-level Tunnelling States and Low-Energy Floppy Modes," *J. Phys. Chem. Solids* **12:** 8041–8064 (2000).

8.2.9 J. Fabian and P.B. Allen, "Anharmonic Decay of Vibrational States in Amorphous Silicon," *Phys. Rev. Lett.* **77:** (18), 3839–3842 (1996).

8.2.10 J. Teixeira, M.-C. Bellissent-Funel, S.H. Chen, and B. Dorner, "Observation of New Short-Wavelength Collective Excitations in Heavy Water by Coherent Inelastic Neutron Scattering," *Phys. Rev. Lett.* **54:** (25), 2681–2683 (1985).

8.2.11 F.J. Bermejo, M. Alvarez, S.M. Bennington, and R. Vallauri, "Absence of Anamolous Dispersion Features in the Inelastic Neutron Scattering Spectra of Water at both Sides of the Melting Transition," *Phys. Rev.* **B 51:** (3), 2250–2262 (1995).

8.2.12 F. Sette, G. Ruocco, M. Krisch, U. Bergmann, C. Masciovecchio, V. Mazzacurati, G. Signorelli, and R. Verbeni, "Collective Dynamics in Water by High Energy Resolution Inelastic X-ray Scattering," *Phys. Rev. Lett.* **75:** (5), 850–853 (1995).

8.2. 13 P. Benassi, M. Krisch, C. Masciovecchio, V. Mazzacurati, G. Monaco, G. Ruocco, F. Sette, and R. Verbeni, "Evidence of High Frequency Propagating Modes in Vitreous Silica," *Phys. Rev. Lett.* **77:** (18), 3835–3838 (1996).

8.2.14 A. Wischnewski, U. Buchenau, A.J. Dianoux, and J. L. Zarestky, "Sound-wave Scattering in Silica," *Phys. Rev. B* **57:** (5), 2663–2666 (1998).

8.2.15 E. Rat, M. Foret, E. Courtens, R. Vacher, and M. Arai, "Observation of the Crossover to Strong Scattering of Acoustic Phonons in Densified Silica," *Phys. Rev. Lett.* **83:** (7), 1355–1358 (1999).

8.2.16 S.N. Taraskin and S.R. Elliott, "Ioffe-Regel Crossover for Plane-wave Vibrational Excitations in Vitreous Silica," *Phys. Rev. B* **61:** (18), 12031–12034 (2000).

8.2.17 S.N. Taraskin and S.R. Elliott, "Propagation of Plane-wave Vibrational Excitations in Disordered Systems," *Phys. Rev. B* **61:** (18), 12017–12030 (2000).

8.2.18 O. Pilla, A. Cunsolo, A. Fontana, C. Masciovecchio, G. Monaco, M. Montagna, G. Ruocco, T. Scopigno, and F. Sette, "Nature of the Short Waveletngh Excitations in

Vitreous Silica: An X-ray Brillouin Scattering Study," *Phys. Rev. Lett.* **85:** (10), 2136–2139 (2000).

8.2.19 M. Foret, B. Hehlen, G. Taillades, E. Courtens, R. Vacher, H. Casalta, and B. Dorner, "Neutron Brillouin and Umkapp Scattering from Glassy Selenium," *Phys. Rev. Lett.* **81:** (10), 2100–2103 (1998).

8.2.20 W. Götze and M.R. Mayr, "Evolution of Vibrational Excitations in Glassy System," *Phys. Rev. E* **61:** (1), 587–606 (2000).

8.2.21 G. Ruocco, F. Sette, R.D. Loenardo, G. Monaco, M. Sampoli, T. Scopigno, and G. Viliani, "Relaxation Processes in Harmonic Glasses," *Phys. Rev. Lett.* **84:** (25), 5788–5791 (2000).

8.2.22 U.C. Tauber and D.R. Nelson, "Superfluid Bosons and Flux Liquids: Disorder, Thermal Fluctuations and Finite-size Effects," *Phys. Repts.,* **289:** 157 (1997).

8.2.23 B. Fok, O. Plantevin, H.R. Glyde, and N. Mulders, "Phonons, Rotons and Layer Modes of Liquid ^{4}He in Aerogel," *Phys. Rev. Lett.,* **85**, 3886 (2000); H.R. Glyde, O. Plantevin, B. Fok, G. Coddens, P.S. Danielson, and H. Schober, "Dynamics of Liquid ^{4}He in Vycor," *Phys. Rev. Lett.,* **84**, 2646 (2000).

8.2.24 M. Imada, A. Fujimon, and Y. Tokura, "Metal Insulator Transitions," *Reviews of Modern Physics,* **70**, 1039 (1998).

8.2.25 D.C. Harris, S.T. Herbert, D. Stroud, and J.C. Garland, "Effect of Random Disorder on the Critical-Behavior of Josephson Junction Arrays," *Phys. Rev. Lett.,* **67**, 3606 (1991).

8.2.26 G. Blatter, M.V. Feigelman, V.B. Geshkenbein, A.I. Larkin and V.M. Vinokus, "Vortices in High-Temperature Superconductors," *Rev. Mod. Phys.,* **66**, 1125 (1994); A. van Otterlo, R.T. Scalettar, G.T. Zimanyi, "Phase Diagram of Disordered Vortices from London Langevin Simulations," *Phys. Rev. Lett.,* **81**, 1497 (1998).

8.2.27 M. Makivic, N. Trivedi and S. Ullah, "Disordered Bosons — Critical Phenomena and Evidence for New Low-Energy Excitations," *Phys. Rev. Lett.,* **71**, (1993).

8.3.1 S.S.P. Parkin, "Giant Magnetoresistance in Magnetic Nanostructures," *Ann. Rev. Mat. Science*, **25:** 357–388 (1995).

8.3.2 H.A. Mook and F. Dogan, "Charge Fluctuations in $YBa_2Cu_3O_{7-x}$ High-Temperature Superconductors," *Nature*, **401:** (6749) 145–147 (1999).

8.3.3 H.A. Mook, P.C. Dai, F. Dogan, and R.D. Hunt, "One-Dimensional Nature of the Magnetic Fluctuations in $YBa_2Cu_3O_{6.6}$," *Nature*, **404:** (6779) 729–731 (2000).

8.3.4 T. Egami, Y. Petrov, and D. Louca, "Lattice Effects on Charge Localization in Cuprates," *J. Supercond.* **13:** 709–712 (2000).

8.3.5 L. Vasiliu-Doloc, S. Rosenkranz, R. Osborn, S.K. Sinha, J.W. Lynn, J. Mesot, O.H. Seeck, G. Preosti, A.J. Fedro, and J.F. Mitchell, "Charge Melting and Polaron Collapse in $La_{1.2}Sr_{1.8}Mn_2O_7$," *Phys. Rev. Lett* **83:** 4393 (1999).

8.3.6 C.P. Adams, J.W. Lynn, Y.M. Mukovskii, A.A. Arsenov, D.A. Shulyatev, "Charge Ordering and Polaron Formation in the Magnetoresistive Oxide $La_{0.7}Ca_{0.3}MnO_3$," *Phys. Rev. Lett.* **85:** 3954–3957 (2000).

8.3.7 R. Osborn, S. Rosenkranz, D.N. Argyriou, L. Vasiliu-Doloc, J.W. Lynn, S.K. Sinha, J.F. Mitchell, K.E. Gray, and S.D. Bader, *Phys. Rev. Lett*. **81**: 3964, 1998).

8.3.8 E. Dagotto, "Experiments on Ladders Reveal a Complex Interplay Between a Spin-gapped Normal State and Superconductivity," *Rep. Prog. Phys.* **62:** 1525–1571 (1999).

8.3.9 S.-H. Lee, C. Broholm, S-W. Cheong, T.H. Kim, and W. Ratcliff, "Local Spin Resonance and Spin-Peierls-like Phase Transition in the Geometrically Frustrated Antiferromagnet $ZnCr_2O_4$," *Phys. Rev. Lett.* **84:** 3718–3721 (2000).

8.3.10 S. Sachdev, "Quantum Phase Transitions," Cambridge University Press (2000).
8.3.11 G. Aeppli, T.E. Mason, S.M. Hayden, H.A. Mook, and J. Kulda, "Nearly Singular Magnetic Fluctuations in the Normal State of a High-Tc Cuprate Superconductor," *Science* **278:** 1432–1435 (1997).
8.3.12 M.C. Aronson, M.B. Maple, P. DeSa, A.M. Tsvelik, and R. Osborn, "Non-Fermi-Liquid Scaling in UCu5-xPdx (x = 1, 1.5): A phenomenological description," *Europhys. Lett.* **40:** 245–250 (1997).
8.3.13 A.H.C. Neto, G. Castilla, and B.A. Jones, "Non-Fermi Liquid Behavior and Griffiths Phase in f-Electron Compounds," *Phys. Rev. Lett.,* **81:** 3531–3534 (1998).
8.3.14 S.S.P. Parkin, K.P. Roche, M.G. Samant, P.M. Rice, R.B. Beyers, R.E. Scheuerlein, E.J. O'Sullivan, S.L. Brown, J. Bucchigano, D.W. Abraham, Y. Lu, M. Rooks, P.L. Trouilloud, R.A. Wanner, and W.J. Gallagher, "Exchange-Biased Magnetic Tunnel Junctions and Application to Nonvolatile Magnetic Random Access Memory," *J. App. Phys.* **85:** 5828–5833, (1999).
8.3.15 C.P. Williams and S.H. Clearwater, "Explorations in Quantum Computing," Springer Verlag (1997).
8.3.16 C.F. Majkrzak, "Neutron Reflectometry Studies of Thin Films and Multilayered Materials," *Acta Physica Polonica A*, **96:** 81–99 (1999).
8.3.17 R.A. Robinson , P.J. Brown, D.N. Argyriou, D.N. Hendrickson, and S.M.J. Aubin, "Internal Magnetic Structure of Mn_{12} Acetate by Polarized Neutron Diffraction," *J. Phys. Cond. Matt.* **12:** 2805–2810 (2000).
8.3.18 E. Chudnovsky, "Quantum Hysteresis in Molecular Magnets," *Science* **274:** 938–939 (1996).
8.3.19 B. Schwarzschild, "Hysteresis Steps Demonstrate Quantum Tunneling of Molecular Spins," *Phys. Today*, p. 17 (January 1997).
8.3.20 E.M. Chudnovsky and J. Tejada, "Macroscopic Quantum Tunneling of the Magnetic Moment," Cambridge University Press (1998).
8.4.1 O. Zhou, J.E. Fischer, N. Coustel, S. Kycia, Q. Zhu, A.R. McGhie, W.J. Romanow, J.P. McCauley, A.B. Smith III, and D. E. Cox, "Structure and Bonding in Alkali-Metal-Doped C_{60}," *Nature*, **351:** 462–464 (1991).
8.4.2 P.W. Stephens, L. Mihaly, P.L. Lee, R.L. Whetten, S.-M. Huang, R. Kaner, F. Deidericht, and K. Holczer, "Structure of Single-Phase Superconducting K_3C_{60}," *Nature*, **351:** 632–634 (1991).
8.4.3 P.W. Stephens, G. Bortel, G. Faigel, M. Tegze, A. Janossy, S. Pekker, G. Oszlanyi, and L. Forro, "Polymeric Fullerene Chains in RbC_{60} and KC_{60}," *Nature*, **370:** 636–639 (1994).
8.4.4 P.W. Stephens, D.E. Cox, J.W. Lauher, L. Mihaly, J.B. Wiley, P.-M. Allemand, A. Hirsch, K. Holczer, Q. Li, J.D. Thompson, and F. Wudl, "Lattice Structure of the Fullerene Ferromagnet TDAE-C_{60}," *Nature*, **355:** 331–332 (1992).
8.4.5 J.D. Axe, A.H. Moudden, D. Hohlwein, D.E. Cox, K.M. Mohanty, and A.R. Moodenbaugh, "Structural Phase Transformations and Superconductivity in $La_{2-x}Ba_xCuO_4$," *Phys. Rev. Lett.*, **62:** 2751–2754 (1989).
8.4.6 H. Takagi, R.J. Cava, M. Marezio, B. Batlogg, J.J. Krajewski, and W.F. Peck Jr., "Disapearance of Superconductivity in Overdoped $La_{2-x}Sr_xCuO_4$ at a Structural Phase Boundary," *Phys. Rev. Lett.*, **68:** 3777–3780 (1992).
8.4.7 A.R. Moodenbaugh, L. Wu, Y. Zhu, L.H. Lewis, and D.E. Cox, "High-resolution X-ray Diffraction Study of $La_{1.88-x}Sr_{0.12}Nd_xCuO_4$," *Phys. Rev. B*, **58:** 9549–9555 (1998).

8.4.8 X. Xiong, Q. Zhu, Z.G. Li, S.C. Moss, H.H. Feng, P.H. Hor, D.E. Cox, S. Bhavaraju, and A.J. Jacobson, "Synchrotron X-ray study of interstitial oxygen ordering in the superconducting phase of $La_2CuO_{4+\delta}$," *J. Mater. Res.*, **11:** 2121–2124 (1996).

8.4.9 C.C. Freyhardt, M. Tsapatsis, R.F. Lobo, K.J. Balkus, M.E. Davis, "A high-silica zeolite with a 14-tetrahedral-atom pore opening," *Nature*, **381:** 295–298 (1996).

8.4.10 R.F. Lobo, M. Tsapatsis, C. Freyhardt, P.W. Khodabandeh, C.-Y. Chen, K.J. Balkus, S.I. Zones, and M. E. Davis, "Characterization of the Extra-Large-Pore Zeolite UTD-1," *J. Am. Chem. Soc.*, **119:** 8474–8484 (1997).

8.4.11 T. Wessels, L.B. Bearlocher, L.B. McCusker, and E.J. Creyghton, "An Ordered Form of the Extra-Large-Pore Zeolite UTD-1: Synthesis and Structure Analysis from Powder Diffraction Data," *J. Am. Chem. Soc.*, **121:** 6242–6247 (1999).

8.4.12 C.C. Freyhardt, R.F. Lobo, S. Khodabandeh, J.E. Lewis, M. Tsapatsis, M. Yoshikawa, M.A. Camblor, M. Pan, M.M. Helmkamp, S.I. Zones, and M.E. Davis, "VPI-8: A High-Silica Molecular Sieve with a Novel 'Pinwheel' Building Unit and Its Implications for the Synthesis of Extra-Large Pore Molecular Sieves," *J. Am. Chem. Soc.*, **118:** 7299–7310 (1996).

8.4.13 B. Noheda, D.E. Cox, G. Shirane, J.A. Gonzalo, L.E. Cross, and S.-E. Park, "A monoclinic ferroelectric phase in the $Pb(Zr_{1-x}Ti_2)O_3$ solid solution", *Appl. Phys. Lett.*, **74:** 2059–2061 (1999).

8.4.14 B. Noheda, J.A. Gonzalo, L.E. Cross, R. Guo, S.-E. Park, D.E. Cox, and G. Shirane, "Tetragonal-to-monoclinic phase transition in a ferroelectric perovskite: the structure of $PbZr_{0.52}Ti_{0.48}O_3$," *Phys. Rev. B*, **61:** 8687–8695 (2000).

8.4.15 R. Guo, L.E. Cross, S.-E. Park, B. Noheda, D.E. Cox, and G. Shirane, "Origin of the High Piezoelectric Response in $PbZr_{1-x}Ti_xO_3$," *Phys. Rev. Lett.*, **84:** 5423–5426 (2000).

8.4.16 P.G. Radaelli, D.E. Cox, M. Marezio, S.-W. Cheong, P.E. Schiffer, and A. P. Ramirez, "Simultaneous Structural, Magnetic, and Electronic Transitions in $La_{1-x}Ca_xMnO_3$," *Phys. Rev. Lett.*, **75:** 4488–4491 (1995).

8.4.17 P.M. Woodward, D.E. Cox, T. Vogt, C.N.R. Rao, and A.K. Cheetham, "Effect of Compositional Fluctuations on the Phase Transitions in $(Nd_{1/2}Sr_{1/2})MnO_3$," *Chem. Mater.*, **11:** 3528–3538 (1999).

8.4.18 P.G. Radaelli, D.E. Cox, M. Marezio, and S. Cheong, "Charge, orbital, and magnetic ordering in $La_{0.5}Ca_{0.5}MnO_3$," *Phys. Rev. B*, **55:** 3015–3023 (1997).

8.4.19 D.E. Cox, P.G. Radaelli, M. Marezio, and S.-W. Cheong, "Structural changes, clustering, and photoinduced phase segregation in $Pr_{0.7}Ca_{0.3}MnO_3$," *Phys. Rev. B*, **57:** 3305–3314 (1998).

8.4.20 A. Moreo, S. Yunoki, and E. Dagotto, "Phase Separation Scenario for Manganese Oxides and Related Materials," *Science*, **283:** 2034–2040 (1999).

8.4.21 J.S. Beck, J.C. Vartuli, W.J. Roth, M.E. Leonowicz, C.T. Kresge, K.D. Schmitt, C.T.-W. Chu, D.H. Olson, E.W. Sheppard, S.B. McCullen, J.B. Higgins, and J.L. Schlenker, "A New Family of Mesoporous Molecular Sieves Prepared with Liquid Crystal Templates," *J. Am. Chem. Soc.*, **114:** 10834–10843 (1992).

8.4.22 C.T. Kresge, M.E. Leonowicz, W.J. Roth, J.C. Vartuli, and J.S. Beck, "Ordered mesoporous molecular sieves synthesized by a liquid-crystal template mechanism," *Nature*, **359:** 710–712 (1992).

8.4.23 R.L. Whetten, J.T. Khoury, M.M. Alvarez, S. Murthy, I. Vezmar, Z.L. Wang, P.W. Stephens, C.L. Cleveland, W.D. Luedtke, and U. Landman, "Nanocrystal Gold Molecules," *Adv. Mater.*, **8:** 428–433 (1996).

8.4.24 A. Firouzi, D. Kumar, L.M. Bull, T. Besier, P. Sieger, Q. Huo, S.A. Walker J.A. Zasadzinski, C. Glinka, J. Nicol, D. Margolese, G.D. Stucky, and B.F. Chmelka, "Cooperative Organization of Inorganic-Surfactant and Biomimetic Assemblies," *Science*, **267:** 1138–1143 (1995).

8.4.25 R.L. Whetten, M.N. Shafigullin, J.T. Khoury, T.G. Schaaff, I. Vezmar, M.M. Alvarez, and A.P. Wilkinson, "Crystal Structures of Molecular Nanocrystal Arrays," *Acc. Chem. Res.*, **32:** 397–406 (1999).

8.5.1 B. Alberts and A. Klug, "The Human Genome itself must be Freely Available to all Humankind," *Nature*, **404:** (6778): 542 (2000).

8.5.2 B. Alberts, "The Cell as a Collection of Protein Machines," *Cell*, **92:** 291–294 (1998).

8.5.3 D.A. Bu, S-H Neumann, C.M. Lee, D.M. Brown, D.M. Engelman, and C.C. Han, "A view of Dynamics Changes in the Molten Globule-native Folding Step by Quasielastic Neutron Scattering," *J. Mol. Biol*., **301:** 525–536, (2000).

8.5.4 G. Zaccai, "How soft is a protein? A Protein Dynamic Force Constant Measured by Neutron Scattering," *Science*, **288:** 1604–1607, (2000).

8.5.5 Z. Guo and D. Thirumalai, "Kinetics and Thermodynamics of Folding a *de novo* Designed Four-Helix Bundle Protein," *J. Mol. Bio*., **263:** 323–343, (1996).

8.5.6 M. Ferrand, A.J. Dianoux, W. Petry, and G. Zaccai, "Thermal Motions and Function of Bacteriorhodopsin in Purple Membranes: Effects of Temperature and Hydration Studied by Neutron Scattering," *PNAS*, **90:** 9668–9672, (1993).

8.5.7 N. Niimura, "Neutrons Expand the Field of Structural Biology," *Biophysical Methods*, 602-608, (1999).

8.5.8 G. Zaccai, "Neutron Scattering in Biology in 1998 and Beyond," *J. Phys. and Chem. of Solids*, **60:** 1291–1295, (1999).

8.5.9 N. Niimura, "Neutrons in Structural Biology," *J. Phys. and Chem. of Solids*, **60:** 1265–1271, (1999).

8.5.10 G. Zaccai, "Moist and Soft, Dry and Stiff: a Review of Neutron Experiments on Hydration-Dynamics-Activity Relations in Purple Membrane of *Halobacterium Salinaru*," *Biophysical Chemistry*, **86:** 249–257 (2000).

8.5.11 P. Langan and B.P. Schoenborn, "Need for Neutron Diffraction Instruments," *Science*, **286**(5442): 1089 (1999).

8.5.12 J. Habash, J. Raftery, R. Nuttall, H.J. Price, K. Wilkinson, J.K. Gilboa, and J.R. Helliwell, "Direct Determination of the Positions of the Deuterium Atoms of the Bound Water in Concavalin A by Neutron Laue Crystallography," *Acta Cryst. D*, **56:** 541–550 (2000).

8.5.13 J.B. Cooper and D.A. Myles, "A Preliminary Neutron Laue Diffraction Study of the Aspartic Proteinase Endothiapepsin," *Acta Cryst. D*, **56:** 246–248, (2000).

8.5.14 C. Bon and C. Wilkinson, "Quasi-Laue Neutron-Diffraction Study of the Water Arrangement in Crystals of Triclinic Hen-Egg-White Lysozyme," *Acta Cryst. D*, **55:** 978–987, (1999).

8.5.15 N. Niimura, Y. Minezaki, T. Nonaka, J.C. Castagna, F. Cipriani, P. Hoghoj, M.S. Lehmann, and C. Wilkinson, "Neutron Laue Diffractometry with an Imaging Plate Provides an Effective Data Collection Regime for Neutron Protein Crystallography," *Nat. Struct. Biol.,* **4:** 909–914, (1997).

8.5.16 C.C. Wilson, "Neutron Diffraction of p-Hydroxyacetanilide (Paracetamol): Libration or Disorder of the Methyl Group at 100 K," *J. Molec. Struct.*, **405:** 207–217 (1997).
8.5.17 N. Ban, P. Nissen, J. Hansen, P.B. Moore, and T.A. Steitz, "The Complete Atomic Structure of the Large Ribosomal Subunit at 2.4 A Resolution," *Science*, **289**(5481): 905–920 (2000).
8.5.18 P. Nissen, J. Hansen, N. Ban, P.B. Moore and T.A. Steitz, "The Structural Basis of Ribosome Activity in Peptide Bond Synthesis," *Science*, **289**(5481): 920–930 (2000).
8.5.19 C.C. Wilkinson, "The Potential for Biological Structure Determination with Pulsed Neutrons," In Neutrons in Biology, Editor B.P. Schoenborn and R.B. Knott, New York, Plenum Press, 35–55 (1996).
8.5.20 J.R. Helliwell, "Neutron Laue Diffraction does it Faster," *Nat. Struct. Biol*., **4:** 874–876 (1997).
8.5.21 A. Wlodawer and L. Sjolin, "Hydrogen Exchange in Rnase A: Neutron Diffraction Study," *PNAS*, **79:** 1418–1422 (1982).
8.5.22 A.A. Kossiakoff, "Protein Dynamics Investigated by the Neutron Diffraction-Hydrogen Exchange Technique," *Nature*, **296:** 713–721 (1983).
8.5.23 A.A. Kossiakoff and S.A. Spencer, "Direct Determination of the Protonation States of Aspartic Acid-102 and Histidine-57 in the Tetrahedral Intermediate of the Serine Proteases," *Nature*, **288:** 414–416 (1981).
8.5.24 H.L. Sham, C. Zhao, K.D. Stewart, D.A. Betebenner, S. Lin, C.H. Park, X.P. Kong, W. Rosenbrook, Jr., T. Herrin, D. Madigan, S. Vasavanonda, N. Lyons, A. Molla, A. Saldivar, K.C. Marsh, E. McDonald, N.E. Wideburg, J.F. Denissen, T. Robins, D.J. Kempf, J.J. Plattner, and D.W. Norbeck, "A Novel, Picomolar Inhibitor of Human Immunodeficiency Virus Type 1 Protease," *J Med. Chem*., **39:** 392–397 (1996).
8.5.25 E.L. Ellsworth, J. Domagala, J.V. Prasad, S. Hagen, D. Ferguson, T. Holler, D. Hupe, N. Graham, C. Nouhan, P. J. Tummino, G. Zeikus, and E. A. Lunney, "4-Hydroxy-5,6-Dihydro-2H-pyran-2-ones.3. Bicyclic and Hetero-Aromatic Ring Systems as 3-Position Scaffolds to Bind to S1' and S2' of the HIV-1 Protease Enzyme," *Bioorg Med Chem Lett*., **19:** 9, 2019–2024 (1999).
8.5.26 V. Dhanaraj, C.G. Dealwis, C. Frazao, M. Badasso, B.L. Sibanda, I.J. Tickle, J.B. Cooper, H.P.C. Driessen, M. Newman, C. Aguilar, S.P. Wood, T.L. Blundell, P. Hobart, K.F. Geoghegan, M.J. Ammirati, D.E. Danley, B.A. O'Connor, and D.J. Hoover, "X-ray Analysis of Peptide-Inhibitor Complexes Define the Structural Basis of Specificity for Human and Mouse Renin," *Nature*, **357:** 466–471 (1992).
8.5.27 C.G. Dealwis, C. Frazao, M. Badasso, J.B. Cooper, I.J. Tickle, H.P. Driessen, T.L. Blundell, and K. Murakami, "The Investigation of the Three-Dimensional Structure of Mouse Submaxillary Renin Complexed with an Inhibitor, CH66, Based on the 4-16 Fragment of Rat Angiotensinogen," *J. Mol. Biol.*, **236:** 342–360 (1993).
8.5.28 A. Sachpatzidis, C. Dealwis, J.B. Lubetsky, P.H. Liang, K.S. Anderson, and E. Lolis, "Crystallographic Studies of Phosphonate-Based Alpha-Reaction Transition-State Analogues Complexed to Tryptophan Synthase," *Biochemistry*, **28:** 38, 12665–12674
8.5.29 A.A. Kossiakoff, M.D. Sintchak, J. Shpungin, and L.G. Presta, "Analysis of Solvent Structure in Proteins using Neutron D_2O-H_2O Solvent Maps: Pattern of Primary and Secondary Solvation of Trypsin," *Proteins*, **12:** 223–236 (1992).
8.5.30 A. Wlodawer and W.A. Hendrickson, "A Procedure for Joint Refinement of Macromolecular Structures with X-ray and Neutron Diffraction Data from Single Crystals," *Acta Cryst*., **A38:** 239–247 (1982).

8.5.31 A. Wlodawer, M. Miller, and L. Sjolin, "Active Site of Rnase: Neutron Diffraction Study of a Complex with Uridine Vanadate, a Transition-State Analog," *PNAS*, **80:** 3628–3631 (1983).
8.5.32 M.M. Teeter and A.A .Kossiakoff, "The Neutron Structure of the Hydrophobic Plant Protein Crambin," In Neutrons in Biology. Edited by Schoenborn B. P., Knott R. B. New York: Plenum Press. 335–348 (1984).
8.5.33 A. Wlodawer, H. Savage, and G. Dodson, "Structure of Insulin: Result of Joint Neutron and X-ray Refinement," *Acta Cryst. B*, **45:** 99–107 (1989).
8.5.34 S.E.V. Phillips and B.P. Schoenborn, "Neutron Diffraction Reveals Oxygen-Histidine Hydrogen Bond in Oxymyoglobin," *Nature*, **292:** 81–82 (1981).
8.5.35 X. Cheng and B.P. Schoenborn, "Hydration in Protein Crystals, A Neutron Diffraction Analysis of Carbon Monoxymyoglobin," *Acta. Cryst. B*, **46:** 195–208 (1990).
8.5.36 M.S. Lehmann, S.A. Mason, and G.J. McIntyre, "Study of Ethanol-Lysozyme Interactions using Neutron Diffraction," *Biochemistry*, **24:** 5862–5869 (1985).
8.5.37 M.S. Lehmann and R.F.D. Stanfield, "Binding of Dimethyl Sulfoxide to Lysozyme in Crystals, Studied with Neutron Diffraction," *Biochemistry*, **28:** 7028–7033 (1989).
8.5.38 F. Cipriani, J.C. Castagna, M.S. Lehmann, and C. Wilkinson, "A Large Image-Plate Detector for Neutrons," *Physica B*., **213-214:** 975–977 (1995).
8.5.39 A. Wlodawer, J. Walter, R. Huber, and L. Sjolin, "Structure of Bovine Pancreatic Trypsin Inhibitor – Results of Joint Neutron and X-ray Refinement of Crystal Form II," *J Mol Biol*., **180:** 301–329 (1984).
8.5.40 M. Weik, H. Patzelt, G. Zaccai, and D. Oesterhelt, "Localization of Glycolipids in Membranes by in Vivi Labeling and Neutron Diffraction," *Mol. Cell*., **1:** 411–419 (1998).
8.5.41 A.J. Schultz, R.G. Teller, M.A. Beno, J.M. Williams, M. Brookhard, W. Lamanna, and M.B. Humphrey, "Argonne Intense Pulsed Neutron Source Used to Solve the Molecular Structure of a Novel Organometallic Complex," *Science*, **220:** 197–199 (1983).
8.5.42 A.A. Kossiakoff, "The Application of Neutron Crystallography to the Study of Dynamic and Hydration Properties of Proteins," *Annu. Rev. Biochem*., **54:** 1195–1227 (1985).
8.5.43 H. Savage and A. Wlodawer, "Determination of Water Structure around Biomolecules Using X-ray and Neutron Diffraction Methods," *Methods Enzymol*., **127:** 162–183 (1986).
8.5.44 B.P. Schoenborn, "The Solvent Effect in Protein Crystals," *J. Mol. Biol*., **201:** 741–749 (1988).
8.5.45 J.S. Finer-Moore, A.A. Kossiakoff, J.H. Hurley, T. Earnest, and R.M. Stroud, "Solvent Structure in Crystals of Trypsin Determined by X-ray and Neutron Diffraction," *Proteins*, **12:** 203–222 (1992).
8.5.46 D.J. Svergun, M.H.J. Koch, S. Kuprin, S. Richard, and G. Zaccai, "Hydration Shell in Solution: Validation by X-ray and Neutron Scattering," *PNAS*, **95:** 2267–2272 (1998).
8.5.47 M. Capel, P.B. Moore, D.M. Engleman, D. Snider, B.P. Schoenborn, M. Kjeldgaard, J. Langer, V. Ramakrishnan, I. Sillers, and S. Yabuki, "Complete Mapping of the Proteins in the Small Ribosome Subunit of E. Coli," *Science*, **238:** 1403–1406 (1987).
8.5.48 B. Jacrot, C. Chauvin, and J. Witz, "Comparative Neutron Small-Angle Scattering Study of Small Spherical RNA Viruses," *Nature*, **266:** 417–421 (1977).
8.5.49 B. Norden, C. Elvingson, M. Kubista, B. Sjoberg, H. Ryberg, M. Ryberg, K. Mortensen, and M. Takahashi, "Structure of RecA-DNA Complexes Studied by Combination of Linear Dichroism and Small-angle Neutron Scattering Measurements on Flow-Oriented Samples," *J. Mol. Biol.*, **226:** 1175– (1992).

8.5.50 H. Liu, J. Gapinski, L. Skibinska, A. Patkowski, and R. Pecora, "Chemical Physics, Effect of Electrostatic Interactions on the Dynamics of Semiflexible Monodisperse DNA Fragments," **113**(14): 6001–6010 (2000).

8.5.51 P. Cluzel, M. Surette, and S. Leibler, "An Ultrasensitive Bacterial Motor Revealed by Monitoring Signaling Proteins in Single Cells," *Science*, **287**, 1652–1655 (2000).

8.5.52 N.B. Cole, C.L. Smith, N. Sciaky, M. Terasaki, M. Edidin, and J. Lippincott, "Cross-Link Density Influence on the Relaxations in Glass- and Gel-Forming Polyurethanes by Neutron and Brillouin Scattering," *Physical Review B-Condensed Matter*, **57:** (18), 11212–11222 (1998).

8.5.53 Y. Scheyer, C. Levelut, J. Pelous, and D. Durand, "Diffusional Mobility of Golgi Proteins in Membranes of Living Cells," *Science*, **273:** 797–801 (1996).

8.5.54 V.A. Feher and J. Cavanagh, "Millisecond-Timescale Motions Contribute to the Function of the Bacterial Response Regulator Protein Spo0F," *Nature*, **400:** 289–293 (1999).

8.5.55 D. Huster, K. Arnold, and K. Gawrisch, "Investigation of Lipid Organization in Biological Membranes by Two-Dimensional Nuclear Overhauser Enhancement Spectroscopy," *J. of Phys. Chem. B*, **103:** 243–251 (1999).

8.5.56 R.E. Lechner, N.A. Dencher, J. Fitter, and T. Dippel, "2-Dimensional Proton Diffusion on Purple Membrane," *Solid State Ionics***, 70:** 296–304 (1994).

8.5.57 J. Fitter, R.E. Lechner, and N.A. Dencher, "Interactions of Hydration Water and Biological Membranes Studied by Neutron Scattering," *J. Phys. Chem. B*, **103:** 8036–8050 (1999).

8.5.60 S. Janssen, H. Natter, R. Hempelmann, T. Striffler, U. Stuhr, H. Wipf, H. Hahn, and J.C. Cook, "Hydrogen Diffusion in Nanocrystalline PD by Means of Quasielastic Neutron Scattering," *Nanostructured Materials*, **9:** 579–582 (1997).

8.5.61 M. Muller, W. Press, W. Langel, G. Coddens, M. Ferrand, and H. Buttner, "Rotational Excitations of Methane Molecules in Porous Media," *Physica B*, **226:** (1-3) 185–188 (1996).

8.5.62 B. Ruffle, J. Ollivier, S. Longeville, and R.E. Lechner, "Neutron Time-of-Flight Measurement Techniques: New Possibilities of TOF Spectroscopy with NEAT at BENSC," *Nuclear Instruments & Methods In Physics Research Section A — Accelerators Spectrometers Detectors And Associated Equipment*, **449:** (1-2) 322–330 (2000).

8.5.63 G. Büldt, U. Gally, J. Seelig, and G. Zaccai, "Neutron Diffraction Studies of Phosphatidylcholine Model Membranes. I. Headgroup Conformation," *J. Mol. Biol.*, **134:** 673–691 (1979).

8.5.64 G. Zaccai, A. Büldt, and J. Seelig, "Neutron Diffraction Studies of Phosphatidylcholine Model Membranes. II. Chain Conformation and Segmental Disorder," *J. Mol. Biol.*, **134:** 693–706 (1979).

8.5.65 L. Herbette, P. DeFoor, S. Fleischer, D. Pascolini, A. Scarpa, and J.K. Blasie, "The Separate Profile Structures of the Calcium Pump Protein and the Phospholipid Bilayer Within Isolated Sarcoplasmic Reticulum Membranes Determined by X-ray and Neutron Diffraction," *Biochim. Biophys. Acta*, **817:** 103–122 (1985).

8.5.66 J.M. Pachence, P.L. Dutton, and J.K. Blasie, "The Reaction Center Profile Structure Derived from Neutron Diffraction," *Biochim. Biophys. Acta Bioenergetics*, **635:** 267–283 (1981).

8.5.67 J.M. Pachence, P.L. Dutton, and J.K. Blasie, "A Structural Investigation of Cytochrome c Binding to Photosynthetic Reaction Centers in Reconstituted Membranes," *Biochim. Biophys. Acta*, **724:** 6–19 (1983).

8.5.68 D.M. Engelman and G. Zaccai, "Bacteriorhodopsin is an Inside-Out Protein," *PNAS,* **77:** 5894–5898 (1980).
8.5.69 W. Fuller, V.T. Forsyth, A. Mahendrasingam, P. Langan, W.J. Pigram, S.A. Mason, and C.C. Wilson, "DNA Hydration Studied by Neutron Fiber Diffraction," *Neutrons in Biology*, ed. B.P. Schoenborn and R.B. Knott (Plenum Press, 1996).
8.5.70 R. Nambudripad, W. Stark, S.J. Opella, and L. Makowski, "Membrane-Mediated Assembly of Filamentous Bacteriophage Pf1 Coat Protein," *Science*, **252:** 1221–1344 (1991).
8.5.71 C.F. Majkrzak and N.F. Berk, "Exact Determination of the Phase in Neutron Reflectometry," *Phys. Rev. B*., **52**(15): 10827–10830 (1995).
8.5.72 L.R. Kneller, A.M. Edwards, C.F. Majkrzak, N.F. Berk, S. Krueger, and J.K. Blasie, "Hydration State of a Single Cytochrome c Monolayer Vectorially — Oriented at a Soft Interface Investigated via Neutron Interferometry," *Biophys. J.* (in press).
8.5.73 R.M. Venable, Y.H. Zhang, B.J. Hardy, and R.W. Pastor, "Molecular-Dynamics Simulations of a Lipid Bilayer and of Hexadecane — An Investigation of Membrane Fluidity," *Science*, **262:** 223–226 (1993).
8.6.1 J.M. Pendlebury and E.M. Hinds, "Particle Electric Dipole Moments," *Nucl. Inst. Meth.* **A440**: 471–478 (2000).
8.6.2 L.J. Lising, et al, *Phys. Rev. C* (2000).
8.6.3 J. Sromicki, "T Violation in the Weak Scalar and Tensor Interaction," *Nucl. Inst. Meth.* **A440**: 609–617 (2000).
8.6.4 A.D. Sakharov, *JETP Lett.* **5**: 24–27 (1967).
8.6.5 L. Wolfenstein, "Violation of Time Reversal Invariance in K0 Decays," *Phys. Rev. Lett.* **83**: 911–912 (1999).
8.6.6 J.D. Jackson, S.B. Treiman, and H.W. Wyld, "Possible Tests of Time Reversal Invariance in Beta Decay," *Phys. Rev.* **106**: 517–521 (1957).
8.6.7 R.N. Mohapathra and J.C. Pati, "Lepton Number as the Fourth Color," *Phys. Rev. D* **10**: 275–289 (1974).
8.6.8 M. Kobayashi and T. Maskawa, "CP-Violation in the Renormalizable Theory of the Weak Interaction," *Prog. Theor. Phys.* **49**: 652–657 (1973).
8.6.9 D.N. Schramm and R.V. Wagoner, "Element Production in the Early Universe," *Ann. \Rev. Nucl. Sci.* **27**: 37–74 (1977).
8.6.10 S. Burles, K.M. Nollett, J.W. Truran, and M.S. Turner, ", "Sharpening the Predictions of Big Bang Nucleosynthesis," *Phys. Rev. Lett.* **82**: 4176–4179 (1999).
8.6.11 B. Desplanques, J.F. Donoghue, and B.R. Holstein," Unified Treatment of the Parity Violating Nuclear Force," *Ann. Phys.* **124**: 449–495 (1980).
8.6.12 E.G. Adelberger and W.C. Haxton," Parity Violation in the N-N Interaction," *Ann. Rev. Nucl. Part. Sci.* **35**: 501–558 (1985).
8.6.13 W.S. Wilburn and J.D. Bowman," Consistency of Parity-Violating Pion-Nucleon Couplings Extracted from Measurements in 18F and 133Cs," *Phys. Rev. C* **57**: 3425–3429 (1998).
8.6.14 B. Desplanques," Parity-non-conservation in Nuclear Forces at Low Energy: Phenomenology and Questions," *Phys. Rep.* **297**: 1–62 (1998).
8.6.15 C.S. Wood, S.C. Bennett, D. Cho, B.P. Masterson, J.L. Roberts, C.E. Tanner, and C.E. Wieman, "Measurement of Parity Nonconservation and an Anapole Moment in Cesium," *Science* **275**: 1759–1763 (1997).

8.6.16 K.M. Nollett and S. Burles," Estimating Reaction Rates and Uncertainties for Primordial Nucleosynthesis", *Phys. Rev. D* **61**: 123505-1–123505-16 (2000).
8.6.17 F. Kappeler, F.K. Thielemann, and M. Wiescher, *Ann. Rev. Nucl. Part. Sci.* **48**: 175–251 (1998).
8.6.18 D.R. Rich et al., *Nucl. Inst. Meth.*, submitted (2000).
8.6.19 International Workshop on Fundamantal Physics with Pulsed Neutron Beams, Research Triangle Park, NC, June 1-3, 2000, proceedings to be published by World Scientific (2001).
8.6.20 R.E. Hill, J.M. Ayana, T.J. Bowles, G.L. Greene, G. Hogan, S. Lamoreaux, L. Marek, R. Mortenson, C.L. Morris, A. Saunders, S.J. Seestrom, W. Teasdale, S. Hoedl, C.Y. Liu, D.A. Smith, A. Young, B.W. Filippone, J. Hua, T. Ito, E. Pasyuk, P. Geltenbort, A. Garcia, B. Fujikawa, S. Baessler, and A. Serebrov, "Performance of the Prototype LANL Solid Deuterium Ultra-Cold Neutron Source," *Nucl. Inst. Meth.* **A440**: 674–681 (2000).
8.6.21 T. J. Bowles and A.R. Young, co-spokesmen, UCN A collaboration (private communication).

9. PELLETIZED MODERATORS AND OTHER R & D EFFORTS

9.1 Pelletized Moderator Development

This section describes results of some efforts that have already progressed significantly and lists others in which work needs to be undertaken. Numerous issues have arisen during concept development that require more information than is now available to provide the basis for detailed design and for potential design innovations. Our R&D program will address these data gaps.

Pelletized moderators are a possibility for the LWTS. Having solid moderating material dispersed in a flowing liquid coolant, which may also be a moderating material, a pelletized moderator might accomplish the following:

- Enhance heat removal, enabling use of moderator materials with good neutronic and poor thermal properties
- Limit the spontaneous release of stored radiation damage energy to small volumes,
- Stabilize against the spontaneous release of stored radiation damage energy
- Dissipate the energy and gases released without damage to moderator structures
- Allow the use of coolants (e.g., liquid helium) with no moderating properties, enabling lower moderator temperatures
- Permit a moderator configuration in which solid moderator material can be exchanged continuously or in batches in the active region

9.1.1 The Pelletized Moderator Concept

Solid methane in liquid hydrogen is an example of a pelletized moderator concept for use at high-power spallation sources where monolithic solid moderators would not be feasible [9.1.1–9.1.5]. Designers often consider solid methane to be the best material for high-resolution moderators on pulsed spallation sources because it has a high hydrogen density (leading to narrow pulses) and favorable low-energy inelastic neutron scattering (leading to low spectral temperatures). Unfortunately, the thermal conductivity of solid methane is very poor (except near the 20.4 K phase transition), which precludes its use as a moderator material in high-power sources. Also, solid methane is subject to radiation damage that builds up stored chemical energy in the material. This energy can spontaneously and precipitously appear as heat (burping), resulting in temperature and pressure increases so large and fast that they threaten the integrity of the moderator vessel. The intent of a pelletized moderator is to avoid the radiation damage by increasing the heat removal capabilities of the moderator system; limiting the volume of solid moderator material involved in the spontaneous, highly nonlinear energy release process; and providing a way to dissipate the pressure surge following a burp. We envision a pelletized moderator as a randomly packed bed of solid methane pellets 1–5 mm in diameter that is cooled by flowing liquid hydrogen. Table 9.1 shows mean hydrogen densities for various methane and hydrogen moderator systems.

Table 9.1. Hydrogen densities for various methane and hydrogen moderator systems. (Percentages indicated are by volume.)

Material	H Density (p/b-cm)	H Density (relative)
Solid methane at 22 K	0.0787	1.11
Liquid hydrogen at 15 bar and 22 K	0.0439	0.49
Solid methane at 22 K with 10% aluminum	0.0709	1.00
48% methane at 22 K with 52% hydrogen at 15 bar	0.0632	0.89
62% methane at 22 K with 38% hydrogen at 15 bar	0.0655	0.92
78% methane at 22 K with 22% hydrogen at 15 bar	0.0709	1.00

All methane moderators at current facilities use a methane-aluminum mix (about 10 vol% aluminum) to provide adequate cooling to the methane. A randomly packed bed of mono-disperse spheres has 62% of the density of the solid. Researches have developed prototypes that accomplish this packing density in 3-mm hexagonal prism pellets of methane and ammonia [9.1.5]. Matching the hydrogen density of a methane-hydrogen pelletized moderator to that of a solid methane/aluminum moderator would require a particle packing fraction of 78%, which is theoretically possible (in a hexagonal close-packed arrangement) but might challenge thermal hydraulics requirements. Nevertheless, the hydrogen density of the 62% packed bed is attractive.

9.1.2 Simulation Techniques

Optimization of a spallation neutron source requires accurate calculations of neutronic performance. A pelletized moderator, with heterogeneity on length scales comparable to those of neutron mean-free-paths, may not perform as a homogenized mixture of its constituent materials. Because previous work [9.1.6] predicts a strong effect of pellet size on moderator performance, we have examined techniques for (a) analyzing the neutronic performance of pelletized moderators, in particular, heterogeneity effects in pelletized moderators and (b) assessing the performance of pelletized moderators in comparison to conventional monolithic moderators. We use the MCNP code package, [9.1.7] which, like most neutronic codes, usually involves defining volumes of specific shape having a specific composition at each location. Unfortunately, this method is ill-suited to the task of modeling a pelletized moderator in detail. Because (a) it requires a great deal of manual setup and (b) it requires a large amount of computer memory and CPU time. However, most neutron transport codes include an alternative capability for treating regular array geometries. MCNP provides this capability in terms of the "lattice geometry," in which a regular array of identical cells fills a larger region — in our case, an array of methane pellets in a hydrogen matrix.

The lattice geometry technique substantially reduces the manual setup time and the computer memory required but still requires significantly more CPU time than the homogenized calculation. For example, calculations with a relatively coarse lattice (7.4-mm pitch with 48% packing fraction) required 60% more CPU time than did a homogenized mixture. Smaller pitched lattices are even more demanding, but CPU time at this level does not present a significant problem.

Finally, we observed that the simple cubic lattice has unrealistic clear streaming paths through the moderator, which do not occur in a randomly packed bed. We have not examined any effects from these clear paths, although we have identified ways to do so.

9.1.3 Calculations of Heterogeneity Effects

The details of the MCNP lattice geometry implementation limit the array to a simple cubic lattice with a maximum packing fraction of $\pi/6 \approx 52\%$ for spherical pellets. This fraction is lower than the desired pellet fraction and lower even than the realistic fraction in a randomly packed bed. However, when we compared calculations for spherical pellets with those for cubic pellets of the same volume, we found no differences in moderator performance. Thus, we modeled our pellets as cubes within a simple cubic lattice, which permits any desired packing fraction.

We performed a series of calculations for a moderator consisting of 48% methane and 52% hydrogen (by volume). This packing fraction permits comparison of a lattice of spherical pellets to one having cubic pellets. We found no significant difference in either the spectral-shape or emission-time distributions between these cases for cell pitches of 0.74 to 7.4 mm and no difference in performance between pellets and a homogenized mixture of the same materials. These findings contrast with the results of work performed elsewhere, [9.1.6] which revealed changes as large as 20% in 1-eV-normalized spectral intensity between pelletized and homogeneous configurations. Although our results seem to indicate that we do not need to consider heterogeneity effects in our calculations, the disagreement with other results and the relatively low cost of modeling heterogeneity justify continuing to include it.

9.1.4 Pelletized Moderator Performance: An Example

We calculated spectral intensities and corresponding emission time distributions for a pelletized moderator having a 48% packing fraction of solid methane, the remainder parahydrogen, both at 22 K and compared the results with those from a conventional methane/aluminum moderator. Figure 9.1 shows normalized lethargy spectra for the two moderators. The integrated neutron thermal intensities are nearly identical. The spectral temperature for the pelletized moderator is slightly higher, but we anticipate that it will decrease at higher pellet packing fractions. Although the pelletized moderator in this case has only 89% of the hydrogen density of the conventional moderator, its spectral intensity is quite respectable.

Figure 9.2 shows a significant difference in the emission time distributions from the two moderators. At the energy shown (5 meV), the pelletized moderator has a slightly higher peak intensity and a lower tail (good aspects) but a slower rising edge and slightly broader pulse (bad aspects). The pelletized moderator pulse shape has some features that seem similar to those of the para-hydrogen moderator pulse shapes. This result may be caused by the clear paths between the methane pellets. Such paths through para-hydrogen (which has a mean-free-path of 450 mm at neutron energies below 15 meV) might result in an unrealistically leakage-dominated moderator.

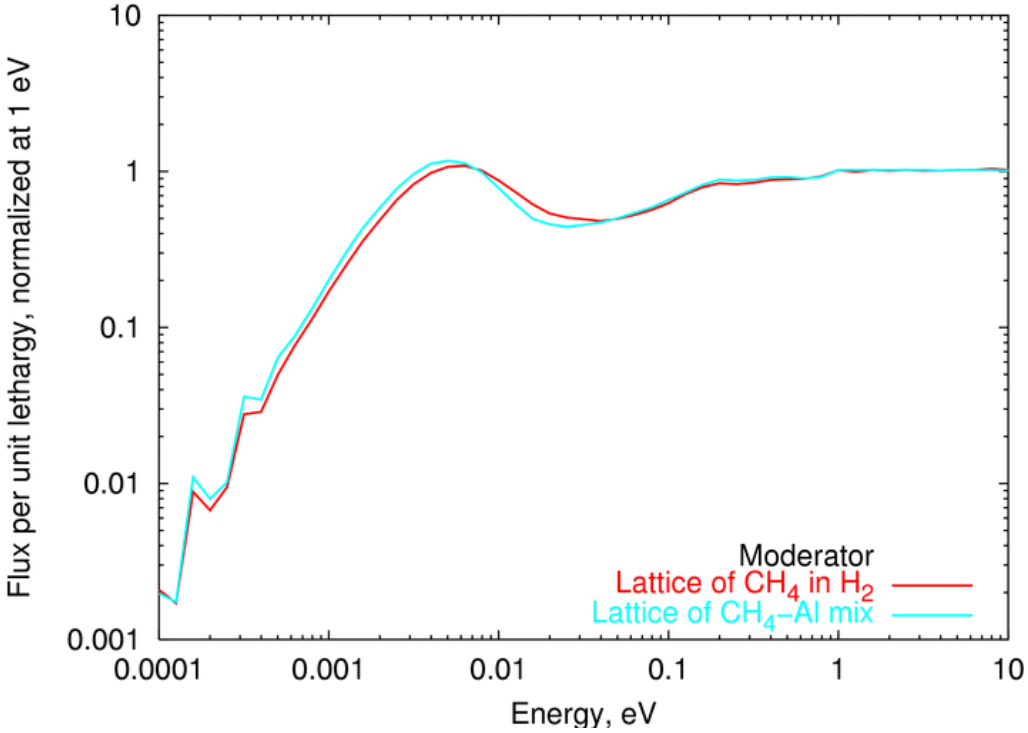

Fig. 9.1. Moderator spectra for pelletized (48% packing fraction) and conventional moderators, normalized to 1 eV.

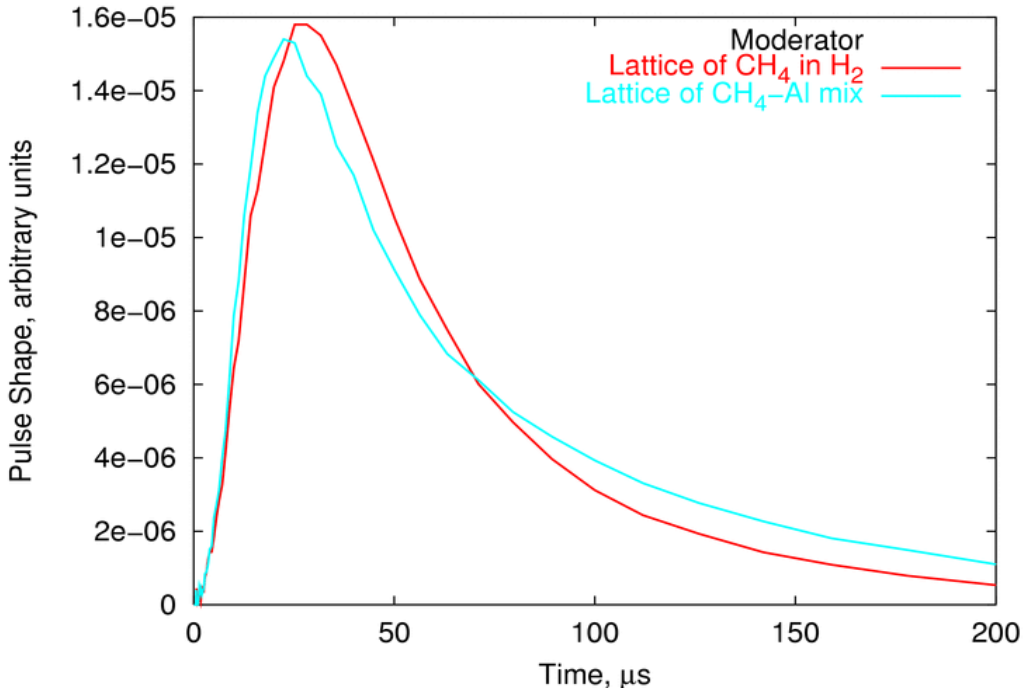

Fig. 9.2. Emission time distributions (5 meV) for pelletized (48% packing fraction) and conventional moderators.

9.2 R&D Program

More R&D relating to the source and instruments is necessary to meet design requirements.

- Guide and bender effectiveness and shielding: Conduct numerical simulations, collect data from ISIS and SNQ at PSI in Switzerland, complete AGS ASTE tests at BNL, and conduct prototype tests at IPNS.

- Solid methane moderators: Track and collaborate in DOE-sponsored pelletized moderator development at CFI Inc.; support cell calculations at UIUC; participate in the ACoM collaboration; cosponsor, track, and collaborate in URAM measurements at Dubna; conduct tests at a small reactor; examine (destructively) the removed IPNS moderator.

- Solid $^{15}NH_3$ alternative: Obtain $S(Q,\omega)$ measurements at IPNS, collaborate in $^{14}NH_3$ moderator tests at Hokkaido University, and conduct tests at a small reactor.

- Compact benders: Conduct tests at IPNS and collect data from ISIS and elsewhere.

- Focusing optics: Conduct prototype tests at IPNS.

- Crystal analyzer spectrometer time focusing: Conduct proof-of-principal tests at IPNS.

- Neutron polarization: Study theory of new techniques and conduct prototype tests at IPNS.

- Drabkin filter: Conduct tests at IPNS.

- Detectors: Acquire and test prototypes at IPNS (e.g., LiGd borate scintillators), and participate in evaluations at ISIS and elsewhere.

- Neutron beam diagnostics: Develop and test techniques at IPNS.

This list is incomplete; we will prioritize and set detailed plans in the areas ultimately chosen for investigation.

9.3 Neutron Physics and Moderator Development Laboratory

The SNS will be the largest and best pulsed neutron source facility in the world. To leverage the investment in that facility, to take best advantage of the expertise that will be concentrated and developed during the design and construction of that facility, and to optimize the performance of that facility, we propose a development center, a Neutron Physics Laboratory (NPL) dedicated to studying the science and engineering of such a neutron source. The NPL might be located at SNS or at another institution. This proposal represents our acknowledgment that pulsed neutron source engineering is at the cutting edge and that new information will make room for new ideas for improving the SNS. Because the SNS project is the world's first greenfield pulsed spallation

neutron source, it presents a unique opportunity to maximize its performance and the long-term scientific impact of fundamental development efforts in neutron production and neutron scattering. In addition, the proposed NPL will serve as a proof-of-principle for small, university-scale neutron source facilities, which will expand teaching and research capabilities within the neutron source user community.

The NPL will consist of a balanced combination of experimental and analytical capabilities. The laboratory will require a neutron source based on a small, low-energy accelerator but one just large enough to perform the experiments necessary to characterize the phenomena being studied. The earlier work of Graham and Carpenter at the University of Michigan, as well as the ongoing work of Kiyanagi at the University of Hokkaido, suggest a likely scale for this operation. The low intensity of this source makes it far more amenable to modification and reconfiguration than a higher power installation. Fewer components require active cooling, far less shielding and personnel access will be far easier. SNS personnel will carry out much of the R&D activity at NPL in collaboration with other interested parties: ISIS (TS2), ESS, and JNF (ACoM, URAM).

We therefore propose that the NPL include a neutron source that produces 5×10^{12} neutrons per second (time averaged), operating in a short-pulsed mode. In such a mode, the accelerator will operate at no more than 240 Hz with a pulse length of no more than 5 μs. The machine should also be capable of operation significantly shorter pulse lengths than at the SNS (an attendant decrease in total yield will be acceptable) because the characteristic pulse length for short-wavelength neutrons at the SNS will approach 0.6 μs, and this range should be accessible to the NPL efforts as well. The recent proposal [9.3.1] to construct a low-energy neutron source (LENS) based on the facilities of the University of Indiana, can serve the purpose we outline here (we are taking part in the planning for that laboratory).

9.4 Conclusions

We have developed a method for modeling the performance of heterogeneous pelletized moderators with relatively little effort. Our results differ from those obtained by others, in that treating a pelletized moderator as a homogenized block gives nearly the same results as the heterogeneous calculation.

Our calculations indicate very promising performance from pelletized methane moderators, which is comparable to that of monolithic methane/aluminum moderators used today. Continuing R&D should include modeling of the polyethylene/hydrogen pelletized systems measured elsewhere [9.4.1, 9.4.2], calculations for other packing fractions and more pellet sizes, the effects of unrealistic clear streaming paths through regular lattices of pellets, and treating randomly packed beds of pellets.

9.5 References

9.1.1 K.D. Williamson and A.T. Lucas, "A Combined H_2/CH_4 Cold Moderator for a Short Pulsed Neutron Source," Proc. 10th Mtg. Intl. Collaboration on Advanced Neutron Sources (D.K. Hyer, Ed.), Institute of Physics Conference Series Number 97, pp. 559–564, Los Alamos National Laboratory, Institute of Physics (Oct. 1988).

9.1.2 A.T. Lucas, G.S. Bauer, and C.D. Sulfredge, "A Pelletized Solid Methane Moderator for a Medium-to-High Power Neutron Source," Proc. 13th Mtg. Intl. Collaboration on Advanced *Neutron Sources* (G.S. Bauer and R. Bercher, Eds.), Vol. II of PSI Proceedings 95–02, (Villigen, Switzerland), pp. 644–653, Paul Scherrer Institute (Nov. 1995).

9.1.3 A.T. Lucas, "Cold Moderators at ORNL," Proc. Intl. Workshop on Cold Moderators for Pulsed Neutron Sources (J.M. Carpenter and E.B. Iverson, Eds.), pp. 137–154, OECD (1998).

9.1.4 G.S. Bauer, "Pulsed Neutron Source Cold Moderators — Concepts, Design, and Engineering," Proc. Intl. Workshop on Cold Moderators for Pulsed Neutron Sources (J.M. Carpenter and E.B. Iverson, eds.), pp. 27–42, OECD (1998).

9.1.5 C.A. Foster and J.M. Carpenter, "An Advanced Cold Moderator Using Solid Methane Pellets," Proc. 15th Mtg. Intl. Collaboration on Advanced Neutron Sources (J. Suzuki and S. Itoh, eds), pp.882–892, JAERI-Conf 2001-002 (Mar. 2001).

9.1.6 Y. Kiyanagi and S. Date, "Neutronic Calculations on Mixed Moderator of Solid Methane and Liquid Hydrogen," Proc. Fourth Mtg. Collaboration for Advanced Cold Moderators (ACoM IV) (H. Barnert-Wiemer, ed.), Forschungszentrum Juelich GmbH (Feb. 1999).

9.1.7 J.F. Briesmeister, "MCNP: A General Monte Carlo N-Particle Transport Code," Los Alamos National Laboratory, Version 4B (Mar. 1997).

9.3.1 LENS Proposal

9.4.1 Y. Ogawa, Y. Kiyanagi, and N. Watanabe, "Neutronic Performance on a Mixed Cold Moderator of Polyethylene Particles and Liquid Hydrogen," Proc. Intl. Workshop on Cold Moderators for Pulsed Neutron Sources (J.M. Carpenter and E.B. Iverson, Eds.), pp. 233–240, OECD (1998).

9.4.2 Y. Ogawa, M. Konno, H. Iwasa, T. Kamiyama, Y. Kiyanagi, M. Furusaka, and N. Watanabe, "Comparison of Decoupled Cryogenic Moderators for High-Resolution Experiments," Proc. ICANS-XIV, 14th Mtg. Intl. Collaboration on Advanced Neutron Sources (J.M. Carpenter and C.A. Tobin, Eds.), pp. 569–578, Utica, Illinois (Jun. 1998).

10. CONTRIBUTORS TO THE DEVELOPMENT OF THE LWTS CONCEPTUAL DESIGN AND SCIENTIFIC CASE

The technical concepts for the, LWTS, the LWTS Science Case, and for the LWTS preliminary instrument package came about in a series of steps, which began in 1998. Initial questions had to do with scale: opening a second target station at SNS would roughly double the number of instruments that SNS could accommodate, based on the already committed accelerator and conventional components of the project. However, beam power diverted to the second target station would diminish the performance of many of the instruments on the first, HPTS. (Later, we found means to deliver adequate power to LWTS while maintaining full power to HPTS.) But then again, a second target station, operating at a fraction of the frequency of the HPTS (but with the same charge delivered per pulse), would better accommodate the instruments that use long-wavelength neutrons and are poorly suited to the 60-Hz HPTS. Moreover, the lower time-average power of a lower-frequency installation would place lower engineering demands on the target and moderators, enabling more effective optimization for long-wavelength applications.

Thus arose the fundamental concepts of LWTS, mutually complementary as well as complimentary: low frequency so as to provide the wavelength bandwidth needed for long-wavelength neutron applications and consequent low power to enable the most effective target and cold moderator design for long-wavelength neutrons. The U.S. National Science Foundation provided funds to further evaluate the LWTS ideas.

The initial list of about 35 instruments for SNS, with estimates of the desired operating frequency and wavelength range, provided a basis for quantifying the division of instruments between the HPTS and LWTS and for setting the performance goals for LWTS. LWTS would provide clear advantages for the total SNS facility, if the pulsing frequency were about 10 Hz, and if the moderators were on average about three times more efficient for producing long-wavelength neutrons as those of HPTS. The early considerations were based on SNS beam power of 2.0 MW. Although the goal for the near term is now 1.4 MW, the basis for LWTS design is still one-third of 2 MW, namely 333 kW.

In summary, the goals for LWTS arose as follows:

- Low frequency — 10 Hz
- Low power, same charge per pulse as HPTS — 33.3 kJ/pulse, 333 kW
- Moderator efficiency for long wavelengths three times greater than HPTS

Further in the vein of conceptual complementarity and complimentarity, optimization for long-wavelength neutron applications leads to extensive use of neutron guides, while curved guides (increasingly effective as wavelengths become longer) act as filters against fast and high-energy neutrons. Incorporating curved (long) guides and/or beam benders (short) enables use of the unconventional "slab moderator" (radial source/moderator) geometry, avoided in multipurpose sources, but more effective. (Multipurpose sources must serve short-wavelength applications and cannot profit from universal use of guides and benders. To minimize the contamination of the beams by fast neutrons, all sources to date have used "wing moderators," that is, tangential source/moderator geometry.)

Still further, a goal for LWTS is to adapt as closely as possible (while optimizing for long-wavelength neutrons and capitalizing on the benefits of lower power) the design of the HPTS, so as to minimize the engineering, design, construction, and operating costs of the second facility.

The following pages list the names of participants in the various activities that took place during the concept development and the technical and scientific evaluations of the LWTS.

Once the participants agreed on these ideas, the Concept Design Group set to work in early 1999 and formulated and evaluated a set of preliminary concepts that led to a preliminary Concept Design Review in January 2000 and the submission of a proposal to the NSF to support further work.

Argonne convened a review of the Concept Design, which took place in January 2000 and endorsed the LWTS concepts. Participants in that review, listed on the following pages, included the most experienced target systems designers; leaders in the use of neutron scattering, especially of long-wavelength neutrons; and experienced designers of neutron-scattering instruments.

Various breakout meetings on the general subject of soft matter science took place during the May 2000 meeting of the Neutron Scattering Society of America in Washington, D.C., which focused attention on the prospects for LWTS. A Reference List of instruments evolved from these and from the ongoing scientific workshops, which provided a basis for evaluating possible physical layouts of the LWTS experimental area. See Section 2.1.

The NSF rapidly approved a program that supported further work on the LWTS technical design, the formulation of a science case for LWTS, and the conceptualization and evaluation of instruments designed to serve the needs of the foreseen scientific applications. The Concept Design Group continued its work, and workshops on behalf of LWTS convened in 2000 to evaluate the uses of LWTS in six different general fields: Polymers, Colloids and Structural Biology; Magnetism; Disordered Materials; Long-Wavelength Powder Diffraction; Chemical Spectroscopy, Protein-folding Dynamics, and Polymer Dynamics; Structural Biology; and Fundamental Physics. The following pages list the participants in those workshops. The sections in Chapter 8 of this report are summaries of the products of their discussions.

Argonne convened a review of the Science Case for LWTS in October 2000 and a general review of the LWTS project in November 2000.

Needs for instrumentation that emerged from the science workshops led eleven groups to develop concepts for eleven instruments or classes of instruments, carried out to varying levels of completeness. The following pages list the names of those who took part in those efforts.

Throughout, the theme of the work was to provide a source design that responds to scientific needs. The work was to have been a repeatedly iterated process in which science drives instruments, instruments drive the source, and source opportunities stimulate instruments that inspire new science. All participants in the LWTS development dedicated their efforts to the process in this spirit.

FULL AND PART-TIME MEMBERS OF THE LWTS CONCEPTUAL DESIGN GROUP

J. M. Carpenter, Design Group Leader

I. Baek, IPNS-ANL
H. A. Belch, IPNS-ANL
K. N. Clausen, ESS
E. B. Iverson, SNS-ORNL
R. K. Crawford, IPNS-ANL
R. Kleb, IPNS-ANL
A. E. Knox, TD-ANL
K. C. Littrell, IPNS-ANL
B. J. Micklich, TD-ANL
J. W. Richardson, IPNS-ANL

LWTS Preliminary Concept Design Review
IPNS-ANL - Jan. 24-25, 2000

Contributors

J. M. Carpenter, IPNS-ANL
E. B. Iverson, SNS-ANL
I. Baek, IPNS-ANL
A. E. Knox, TD-ANL
G. S. Bauer, FZ-Jülich
T. A. Broome, ISIS
G. J. Russell, LANSCE-LANL
N. Watanabe, JAERI
T. A. Gabriel, SNS-ORNL
T. McManamee, SNS-ORNL
L. Magid, Univ. Tenn. Knoxville
H. R. Glyde, Univ. Delaware
J. K. Blasie, Univ. Pennsylvania
R. M. Briber, Univ. Maryland
C. L. Broholm, Johns Hopkins
T. P. Russell, Univ. Mass.
T. E. Mason, SNS-ORNL
R. K. Crawford, IPNS-ANL
J. W. Richardson, IPNS-ANL

SNS LWTS Polymers, Colloids & Structural Biology Workshop
University of Maryland – April 19, 2000

Contributors

J. F. Ankner, SNS-ORNL
S. Baker, Harvey Mudd Univ.
J. Briber, Univ. Maryland
E. B. Iverson, SNS-ORNL
E. Kaler, Univ. Delaware
L. Magid, Univ. Tenn. Knoxville
T. E. Mason, SNS-ORNL
A. Palmer, Howard Univ.
J. W. Richardson, IPNS-ANL
T. Russell, Univ. Massachusetts
J. K. Zhao, SNS-ORNL

Magnetism Workshop
ANL - April 27, 2000

Contributors

D. Argyriou, MSD-ANL
C. Broholm, Johns Hopkins Univ.
G. Aeppli, NEC Research
D. Abernathy, SNS-ORNL
J. D. Jorgensen, MSD-ANL
M. Lumsden, ORNL
J. W. Lynn, NIST
J. L. Manson, MSD-ANL

Magnetism Workshop Contributors (cont)

J. Ankner, SNS-ORNL
W. Bao, LANL
M. Bird, NHMFL
G. Boebinger, LANL
J. M. Carpenter, IPNS-ANL
C-L Chien, Johns Hopkins
P. Coleman, Rutgers Univ.
M. Fitzsimmons, LANSCE-LANL
M. Greven, Stanford Univ.
F. Mezei, HMI
H. Nakotte, New Mexico St. U.
R. Osborn, MSD-ANL
S. S. P. Parkin, IBM Almaden Res. C.
A. P. Ramirez, Lucent Tech.
J. Rhyne, Univ. Missouri
H. Schneider-Muntau, NHMFL
J. Tranquada, BNL

Disordered Materials Workshop
University of Delaware - April 28-29, 2000

Contributors

C. A. Angell, Arizona State Univ.
S. Baker, Harvey Mudd Univ.
F. J. Bermejo, C.S.I.C. Madrid Spain
J. M. Carpenter, IPNS-ANL
H. R. Glyde, Univ. Delaware
K. W. Herwig, SNS-ORNL
L. E. Iton, MSD-ANL
S. M. Kauzlarich, UC-Davis
D. G. Kearley, Univ. Delft
M. L. Klein, Univ. Pennsylvania
D. D. Klug, NRC-Canada
J. D. Londono, DuPont
C-K Loong, IPNS-ANL
L. Magid, Univ. Tenn. Knoxville
D. L. Price, MSD-ANL
M. L. Saboungi, MSD-ANL
P. Sokol, Penn State Univ.
H. L. Strauss, UC-Berkeley
G. X. Tessema, NSF
J. Turner, Univ. Tenn. Knoxville

Long Wavelength Powder Diffraction Workshop
ANL - May 12, 2000

Contributors

J. D. Jorgensen, MSD-ANL
K. Anderson, ISIS
D. Argyriou, MSD-ANL
J. P. Hodges, SNS-ORNL
K. Poeppelmeier, Northwestern Univ.
J. W. Richardson, IPNS-ANL
A. Stein, Univ. Minnesota
P. W. Stephens, SUNY Stony Brook
B. Toby, NIST
J. Turner, Univ. Tenn. Knoxville
R. B. Von Dreele, LANSCE-LANL
A. P. Wilkinson, Georgia Tech.
R. Whetten, Georgia Tech.

Spallation Neutron Source Users Meeting
Washington, DC- May 21-24, 2000
~300 Attendees

Workshop on "Fundamental Physics with Pulsed Neutron Beams"
Research Triangle Park, North Carolina – June 1-3, 2000
~60 attendees

Proceedings published in "Fundamental Physics with Pulsed Neutron Beams", eds. C. Gould, G. Greene, F. Plasil, M. Snow, World Scientific, 2001

Workshop on Chemical Spectroscopy, Protein Folding Dynamics and Polymer Dynamics
ANL - Oct. 10-11, 2000

Contributors

H. N. Bordallo, IPNS-ANL
J. K. Blasie, Univ. Pennsylvania
J. M. Carpenter, IPNS-ANL
K. W. Herwig, SNS-ORNL
Z. Bu, NIST
J. Eckert, LANSCE-LANL
B. Frick, ILL
K. Gawrisch, NIH
G.G. J. Kearley, Delft Univ.
M. L. Klein, Univ. Pennsylvania
R. E. Lechner, HMI
L. Magid, Univ. Tenn. Knoxville
J. W. Richardson, IPNS-ANL
G. F. Strouse, UC Santa Barbara
D. J. Tobias, UC Irvine
K. W. Zilm, Yale Univ.

Structural Biology
University of Tennessee - Knoxville – Dec. 18-19, 2000

Contributors

J. Becker, Univ. Tenn. Knoxville
B. Bennett, Univ. Tenn. Knoxville
H. Bordallo, IPNS-ANL
M. Buchanan, ORNL
C. Bunick, Vanderbilt Med. Sch
G. Bunick, BIO-ORNL
D. Carter, New Century Pharmac.
D. Cole, OBER/DOE
C. Dealwis, Univ. Tenn. Knoxville
L. Edberg, CBSE, UAB
M. Fawver, Neutron Science Init., UT
V. Gupta, Univ. Tenn. Knoxville
L. Hanson, BIO-ORNL
J. Harp, BIO-ORNL
J. Helliwell, Univ. of Manchester
J. Hutchinson, ORNL
T. Koetzle, CHM-BNL
C. Kundrot, MSFC-NASA
P. Langan, BIO-LANL
G. Lynn, CSMB-ORNL
L. Magid, Univ. Tenn. Knoxville
T. Mason, SNS-ORNL
D. McRee, Crystallography-Scripps
W. Minor, Univ. of Virginia
D. Myles, EMBL-Grenoble
N. Niimura, JAERI/ASRC
A. J. Schultz, IPNS-ANL
E. Serpersu, Univ. Tenn. Knoxville
E. Snell, MSFC-NASA
A. Soares, Florida State Univ.
W. Stallings, Pharmacia Corp.
I. Tanaka, JAERI/ASRC
M. Teplova, Biological Sciences
V. Terechko, Biological Sciences
P. Thiyagarajan, IPNS-ANL
P. Timmons, ILL, LSS Group
T. Uchiki, Univ. Tenn. Knoxville
G. Wignall, SSD-ORNL
M. Wilkerson, Univ. Tenn. Knoxville
A. Wilkinson, Georgia Tech. Inst.
C. Wilson, ISIS-RAL
J. K. Zhao, SNS-ORNL

INSTRUMENT CONCEPT DEVELOPMENT TEAMS

Broad-Range Intense Multipurpose SANS
Contributors

J. M. Carpenter, IPNS-ANL
K. C. Littrell, IPNS-ANL
P. Seeger, LANSCE-LANL
P. Thiyagarajan, IPNS-ANL

200-neV Backscattering Spectrometer
Contributors

H. N. Bordallo, IPNS-ANL
J. M. Carpenter , IPNS-ANL
K. Herwig, SNS-ORNL
K. C. Littrell, IPNS-ANL

Magnetism Diffractometer
Contributors

D. Argyriou, MSD-ANL
J. M. Carpenter, IPNS-ANL
J. D. Jorgensen, MSD-ANL
K. C. Littrell, IPNS-ANL

Broad-Band Reflectometer
Contributors

J. Ankner, SNS-ORNL
G. Felcher, MSD-ANL
E. Gilbert, IPNS-ANL

Grazing Incidence SANS Reflectometer
Contributors

J. Ankner, SNS-ORNL
G. Felcher, MSD-ANL
E. Gilbert, IPNS-ANL

Neutron Spin Echo Spectrometer
Contributors

G. Felcher, MSD-ANL
F. Klose, SNS-ORNL
J. Lal, IPNS-ANL
K. C. Littrell, IPNS-ANL

Polarized Reflectometer
Contributors

G. Felcher, MSD-ANL
F. Klose, SNS-ORNL
S. te Velthuis, MSD-ANL

Fundamental Neutron Physics
Contributors

G. Greene, LANSCE-LANL
K. C. Littrell, IPNS-ANL
M. Snow, Indiana Univ.

Direct-Geometry Spectrometer
Contributors

C. J. Benmore, IPNS-ANL
C-K Loong, IPNS-ANL

Instrument Concept Development Teams (cont)

High-Resolution Powder Diffractometer
Contributors

J. P. Hodges, SNS-ORNL
J. D. Jorgensen, MSD-ANL
J. W. Richardson, IPNS-ANL
A. Wilkinson, Georgia Tech

Protein Diffractometer
Contributors

C. Dealwis, Univ. Tenn. Knoxville
K. C. Littrell, IPNS-ANL
A. J. Schultz, IPNS-ANL
P. Thiyagarajan, IPNS-ANL